UNIVERSITY OF CALIFORNIA SAN DIEGO

Isoform-specific PKA holoenzymes differ in structure, function and allosteric regulation

A dissertation submitted in partial satisfaction of the requirements for
the degree Doctor of Philosophy

in

Chemistry

by

Tsanwen Lu

Committee in charge:

Professor Susan S. Taylor, Chair
Professor Michael Burkart
Professor Mark Herzik
Professor Andres Leschziner
Professor Alexandra Newton
Professor Haim Weizman

2020

This dissertation of Tsanwen Lu is approved, and it is acceptable in quality and form for publication on microfilm and electronically:

_____

_____

_____

_____

_____

_____
Chair

University of California San Diego

2020

DEDICATION

To my family.

TABLE OF CONTENTS

LIST OF FIGURES

LIST OF TABLES

ACKNOWLEDGEMENTS

I would like to thank my advisor, Dr. Susan Taylor for all the supports. She gave me all the opportunities and resources to let me become an independent scientist. She showed me that we need to be bold on science, be careful on research, be open minded to the world, and be confidence to what you believe. I am so grateful that I have her as a role model in my graduate school. If I have any chance to become a good scientist, it is all because of her. I would also like to thank my thesis committee members: Dr. Andres Leschziner, Dr. Alexandra Newton, Dr. Michael Burkart, Dr. Mark Herzik, Dr. Haim Weizman, and my previous committee member, Dr. Elizabeth Villa for all the insightful discussions and advices. They make sure I am on the right path of research.

I also need to thank all the collaborators during my PhD studies. Dr. Ping Zhang showed me the world of crystallography, and she also gave me so many useful suggestions and help inside and outside the lab. Dr. Michael Cianfrocco has taught me cryoEM knowledge. By working with Dr. Jin Zhang and Jason, I am able to start seeing the world of cells. They are like my other mentors and I have learned so much from them during the collaborations.

Thanks all the members in Taylor lab, I cannot finish my PhD without any of them. Grace has always encouraged me and helped me sort out all the problems. I cannot imagine my lab life without her. I would like to thank Jian, Phillip and Jody for their help on crystallography, SAXS and simulations. They are selfless and have taught me everything they know. I also appreciate the help and discussion with Frank, Mira, Lalima, Jason and Evan. I also need to thank the invaluable help from Nick and Cole. I am so grateful to be in this lab environment with countless supports and stimulations.

I also need to thank all my friends outside the lab. I am grateful to have these friends who made life fun. They give me the strength to finish my PhD: En-ching, Hsiu-I, Peng-Hao, Ti, Curtis, Chad, I-Fen, Yijia, Daniel, and Mickey. I am so glad I have met them in San Diego. My life would not be the same without any of them.

Most importantly, I want to thank my family. They show unconditionally love, trust and supports. Even though they live in the opposite side of the earth, their supports have been crucial for me to finish my PhD.

Chapter 2 includes the material that appears in **Lu, T.-W.**; Wu, J.; Aoto, P. C.; Weng, J.-H.; Ahuja, L. G.; Sun, N.; Cheng, C. Y.; Zhang, P.; Taylor, S. S. "Two PKA RIα holoenzyme states define ATP as an isoform-specific orthosteric inhibitor that competes with the allosteric activator, cAMP" *Proc National Acad Sci* **2019**, *116*, 16347-16356. The dissertation author is the primary author of this manuscript.

Chapter 3 includes the material that appears in Cao, B.*; **Lu, T.-W.***; Fiesco, J. A. M.*; Tomasini, M.; Fan, L.; Simon, S. M.; Taylor, S. S.; Zhang, P. "Structures of the PKA RIα Holoenzyme with the FLHCC Driver J-PKAcα or Wild-Type PKAcα" *Structure* **2019**, *27*, 816-828 e814. The dissertation author is one of the primary authors of this manuscript. ***Contributed equally**.

Chapter 4 is currently submitted as a manuscript by **Lu, T.-W.**; Aoto, P. C; Weng, J.-H.; Nielsen, C.; Cash, J. N.; Hall, J.; Zhang, P.; Simon, M. S.; Cianfrocco, M. A.; Taylor, S. S. "Capturing allostery: asymmetry and dynamics of PKA RIIβ holoenzyme with DnaJB1-PKAc fusion in fibrolamellar hepatoceullar carcinoma" The dissertation author is the primary author of this manuscript.

VITA

2008 *B.S.*, Chemistry, National Taiwan University, Taiwan

2010 *M.S.*, Chemistry, National Taiwan University, Taiwan

2020 *Ph.D.,* Chemistry & Biochemistry, University of California San Diego, USA

Publications

1) **Lu, T.-W.**; Aoto, P. C; Weng, J.-H.; Nielsen, C.; Cash, J. N.; Hall, J.; Zhang, P.; Simon, M. S.; Cianfrocco, M. A.; "Capturing allostery: asymmetry and dynamics of PKA RIIβ holoenzyme with DnaJB1-PKAc fusion in fibrolamellar hepatoceullar carcinoma" Under review

2) Watanabe, R.; Buschauer, R.; Böhning, J.; Audagnotto, M.; Lasker, K.; **Lu, T.-W.**; Boassa, D.; Taylor, S. S.; Villa, E. "In situ structure of a LRRK2 Parkinson's disease-mutant bound to microtubules" Under revision

3) Zhang, J. Z.; **Lu, T.-W.**; Tenner, B.; Yang, J.; Zhang, J.-F.; Taylor, S. S.; Mehta, S.; Zhang, J. "PKA regulatory RIα forms a cAMP/PKA signaling compartment through phase separation" Under revision

4) **Lu, T.-W.**; Wu, J.; Aoto, P. C.; Weng, J.-H.; Ahuja, L. G.; Sun, N.; Cheng, C. Y.; Zhang, P.; Taylor, S. S. "Two PKA RIα holoenzyme states define ATP as an isoform-specific orthosteric inhibitor that competes with the allosteric activator, cAMP" *Proc National Acad Sci* **2019**, *116*, 16347-16356

https://doi.org/10.1073/pnas.1906036116

5) Cao, B.*; **Lu, T.-W.***; Fiesco, J. A. M.*; Tomasini, M.; Fan, L.; Simon, S. M.; Taylor, S. S.; Zhang, P. "Structures of the PKA RIα Holoenzyme with the FLHCC Driver J-PKAcα or Wild-Type PKAcα" *Structure* **2019**, *27*, 816-828 e814

*** Contribute equally**

https://doi.org/10.1016/j.str.2019.03.001

6) Bachmann, V.; Mayrhofer, J.; Ilouz, R.; Tschaikner, P.; Raffeiner, P.; Röck, R.; Courcelles, M.; Apelt, F.; **Lu, T.-W.**; Baillie, G.; Thibault, P.; Aanstad, P.; Stelzl, U.; Taylor, S.; Stefan, E. "Gpr161 anchoring of PKA consolidates GPCR and cAMP signaling" *Proc National Acad Sci* **2016**, *113*, 7786–7791

https://doi.org/10.1073/pnas.1608061113

7) **Lu, T.-W.**; Chang, C.-F.; Lai, C.-C.; Chiu, S.-H. "A Molecular Switch Based on Very Weak Association Between BPX26C6 and Two Recognition Units" *Org. Lett.* **2013**, *15*, 5742-5745

https://doi.org/10.1021/ol4027864

8) Hsueh, S.-Y.; Kuo, C.-T.; **Lu, T.-W.**; Lai, C.-C.; Liu, Y.-H.; Hsu, H.-F.; Peng, S.-M.; Chen, C.-C.; Chiu, S.-H. "Acid/Base- and Anion Controllable Organogels Formed from Urea-based Molecular Switch" *Angew. Chem. Int. Ed.* **2010**, *49*, 9170-9173

https://doi.org/10.1002/anie.201004090

ABSTRACT OF THE DISSERTATION

Isoform-specific PKA holoenzymes differ in structure, function and allosteric regulation

by

Tsanwen Lu

Doctor of Philosophy in Chemistry

University of California San Diego, 2020

Professor Susan S. Taylor, Chair

Protein Kinase A (PKA) is the master switch for cAMP-mediated signaling. The inactive PKA holoenzymes (R_2C_2) are comprised of a cAMP-binding regulatory (R)-subunit dimer and 2 catalytic (C)-subunits, while cAMP binding to the R-subunits unleashes the activity of the C-subunits. Of the 4 functionally non-redundant R-subunits (RIα, RIβ, RIIα, RIIβ), RIα and RIβ contain PKA pseudo-substrate sites, in contrast to RIIα and RIIβ, which have substrate sites in their inhibitor sequences.

One of my main projects was to study the isoform-specific features of the PKA holoenzymes. I solved the crystal structure of the full-length RIα holoenzyme in two

conformations and identified a novel isoform-specific function. The two conformations differ by their ATP-dependency. ATP also facilitates RIα holoenzyme formation by locking it into an inactive state that becomes more resistant to cAMP. ATP has no effect on the RIIβ holoenzyme conformation; instead it is a substrate that phosphorylates the inhibitor sequence in RIIβ. When the RIIβ holoenzyme is phosphorylated, it is easier to active with cAMP. The structures, combined with functional and biochemical data, reveal distinct isoform-specific quaternary structures and allosteric mechanisms. Both the *in vitro* and *in vivo* studies reveal that elevating ATP levels could turn on RIIα/RIIβ-related signaling pathways, while RIα/RIβ -related signaling would be triggered by depressing the levels of ATP.

Another part of my research focused on a fusion oncogene of the C-subunit, DnaJB1-PKAc (J-C) that drives fibrolamellar hepatocellular carcinoma (FL-HCC). DnaJB1-PKAc holoenzymes formed with RIα and RIIβ reveal different PKA dysfunctions. The crystal structure and biochemical properties of the $RI\alpha_2$J-C_2 holoenzyme are similar to the wild-type holoenzyme. However, this mutant can disrupt RIα holoenzyme localization and cAMP signaling compartmentation. The $RII\beta_2$J-C_2 cryoEM structure is similar to the wild-type holoenzyme, whereas MD simulations and biochemical studies reveal that J-C can alter RIIb dynamics and make the RIIβ holoenzyme easier to be activated by cAMP.

My research highlights distinct PKA isoform-specific allostery in addition to the structural diversity of the isoforms. I also demonstrated that the J-C affects PKA signaling in isoform-specific ways. My studies not only shed light on our mechanistic understanding of PKA signaling, but also provides new insights for future therapeutic directions. How to target different isoforms of J-C holoenzymes and develop unique treatments for different holoenzyme isoforms will be future challenges and directions for curing FL-HCC.

Chapter 1 Introduction of Protein Kinase A

Cell signaling transduction is a way that a cell communicates by giving and receiving messages from the environment or internally with itself. The process of transduction relies on the crosstalk of numerous signaling pathways, which form a complex network in the cells. Each part of the pathway typically contains several signaling proteins, and these signaling proteins are like the nodes in a network, forming a signaling network where each node interacts with and regulates upstream and downstream targets. Any stimulation or perturbation would affect the whole network and cause distinct cellular responses. Signaling proteins thus play a critical role in translating cellular signals. There are many kinds of signaling proteins with different functions, such as receptors, G-proteins, protein kinases, phosphatase, and ubiquitinases. Among all these signaling proteins, protein kinases constitute one of the largest gene families in humans and account for about 2% of the human genome(1).

A kinase is a class of enzymes that transfer the γ-phosphate group from the high energy ATP molecule to its substrates. This event, which is called phosphorylation, is universal in all cell communication. According to the type of kinase substrates, kinases can be subclassified as protein kinases, lipid kinases, and carbohydrate kinases. In contrast to the metabolic kinases are highly regulated and constitute one of the largest and most disease-relevant gene families. Protein kinases can be further divided as; serine/threonine protein kinases, tyrosine kinases, and histidine or lysine kinases based on the amino acid residues that the protein kinase can phosphorylate on. Using bioinformatic analysis has identified more than 500 different of protein kinases in humans, and these protein kinases compose the human kinome (Figure 1-1A)(1). Based on their functions and

sequence similarities, the kinome can be divided into 9 different sub-families, AGC, CAMK, CK1, CMGC, STE, TK, TKL, other, and atypical groups(1).

Phosphorylase kinase (PhK) was the first protein kinase to be discovered and characterized by Krebs, Graves and Fischer in the 1950s(2, 3). Krebs and Fischer later realized that the activation of phosphorylase kinase was regulated and phosphorylated by another kinase, cAMP-dependent kinase or Protein Kinase A (PKA) (4). Since then, their pioneering work has opened up a new field for protein kinases in the regulation of biological processes. In 1992, Krebs and Fischer were awarded the Nobel Prize in Physiology or Medicine for their discoveries and the work on phosphorylation and dephosphorylation as a mechanism for biological regulation.

Protein Kinase A, a serine/threonine kinase that belongs to AGC kinase family, not only regulates PhK, but also plays a critical role in numerous signaling pathways and biological processes in every mammalian cell. Its activity is tightly controlled by cAMP, a second messenger that can trigger various intracellular signaling events. PKA together with G Protein-Coupled-Receptors (GPCRs), G proteins (G_s, G_β and G_γ), Adenylyl Cyclase (AC) form a classic signal transduction cascade in cell communication, which is called the cAMP-dependent signaling pathway (Figure 1-1B)(5). In brief, GPCRs, as transmembrane receptors, can be activated by extracellular ligands such as hormones, small molecules, or neurotransmitters. Once GPCRs are activated, the conformational change can further stimulate the intracellular G protein complex. When the G protein complex is activated, the G_s subunit exchanges GDP for GTP and dissociates from the complex. The free G_s subunit then further binds to and activates AC, which catalyzes the conversion of ATP into cAMP. The elevated concentration of cAMP then leads to the activation of PKA in the cells.

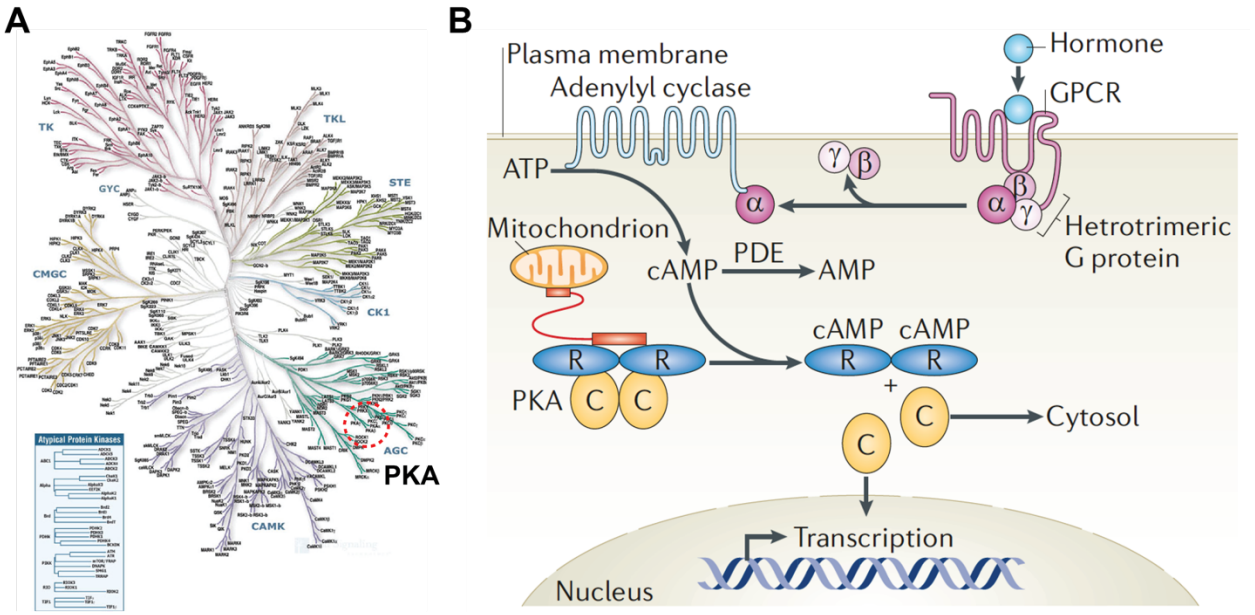

Figure 1-1. Human kinome (A) and PKA-dependent signaling pathway (B). The figures were adapted from Manning *et al.* Science 298, 1912-1934 (2002) and Taylor *et al.* Nat Rev Mol Cell Biol 13, 646-658 (2012).

The activity of PKA is tightly regulated by the direct binding of cAMP, therefore PKA has obviously emerged a central player in the cAMP-dependent signaling pathway. In the absence of cAMP, PKA exists as an inhibited holoenzyme (R_2C_2) containing a dimer of regulatory (R) subunits and two catalytic (C) subunits, while cAMP binding to the R-subunits unleashes the kinase activity of the C-subunit(5). A milestone for the whole protein kinase field was the crystal structure of the PKA C-subunit, the first solved kinase structure(6), which laid the foundation for understanding the conserved structural features of the protein kinase superfamily, and serves as the prototypical kinase against which all others are compared. Our appreciation of the protein kinase structure-function-activity relationship initiated from that first protein kinase structure, PKA C-subunit crystal structure.

1.1 PKA C-subunit

The crystal structure of the PKA C-subunit revealed for the first time a canonical kinase structure (Figure 1-2 and Figure 1-3A). The overall structure contains a dynamic bi-lobal kinase core, which is conserved throughout the kinase family. All of the protein kinases have an N-terminal lobe (N-lobe) defined by β-sheets and a mostly helical C-terminal lobe (C-lobe) (Figure 1-3B). Some of the other important conserved motifs in the protein kinase core, are listed here:

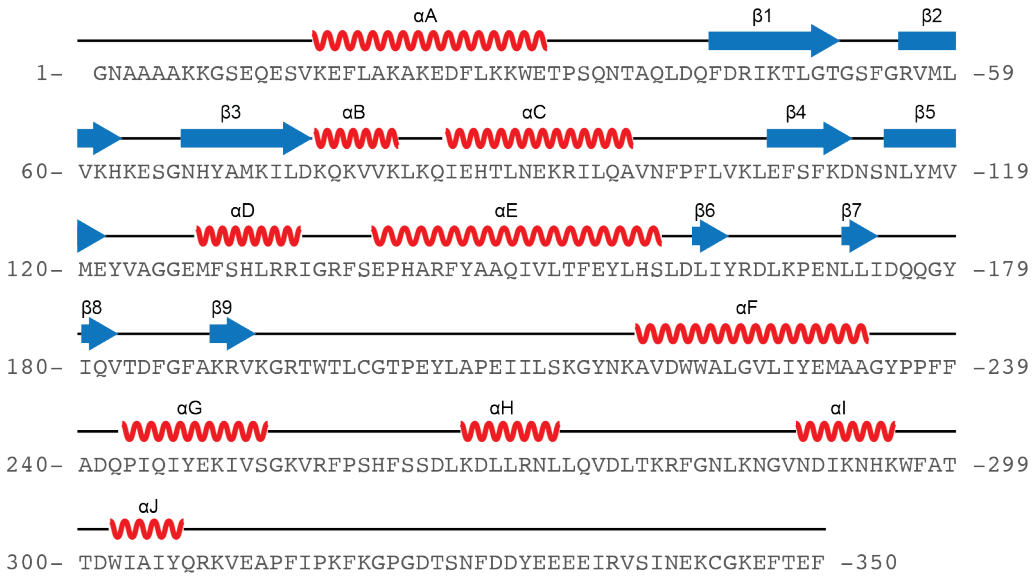

Figure 1-2. Sequence and secondary structure of PKA C-subunit.

Activation segment. Most protein kinases have either tyrosine, serine, or threonine in the activation loop, and they are activated by phosphorylation of these specific residues. The phosphorylated forms of these residues interact with the arginine residue in the H(Y)RD motif. In PKA, Thr197^{C} in the Activation segment is an auto-phosphorylation site, and its phosphorylation is essential for PKA activity. The activation loop together with the DFG motif and APE motif are referred to as the activation segment (residue 184 to 208 in PKA) (Figure 1-3B).

H(Y)RD motif. HR(Y)D is the critical motif for kinase activity. The arginine (Arg165^{C} in PKA) in the H(Y)RD motif directly interacts with the phosphorylated residue in the activation loop. The aspartate (Asp166^{C} in PKA) interacts with the P-site residue of the substrate that catalyze the phosphorylation reaction (Figure 1-3E).

DFG motif. The aspartate residue (Asp184^{C} in PKA) in the DFG motif directly interacts with metal ions in the catalytic pocket. The DFG motif is essential for kinase activity. In the active form of the kinase, the DFG motif remain inside the catalytic pocket, whereas the DFG motif often flips out when the kinase is inactive (Figure 1-3E).

αC-helix. αC-helix is another important motif that regulates kinase activity. The position of the αC-helix sometimes can be used to define the kinase's active and inactive conformations. In the active form, the kinase has a "αC-helix in" conformation, whereas "αC-helix out" is the molecular feature for many inactive conformations. In PKA, Glu91^{C}, is located in the αC-helix and forms a hydrogen bond with Lys72^{C} in the β3 strand. Lys72^{C} plays a critical role for kinase activity. It directly interacts with ATP molecule, and mutation of Lys72^{C} would abolish its kinase activity.

Glycine rich loop (G-loop). G-loop locates between β1 and β2 strands (residue GTGSFG in PKA). It reveals flexible feature and high temperature factor in simulations and in crystal

structure, respectively. G-loop is essential for ATP binding, it positions ATP molecule and facilitate its binding to the kinase pocket (Figure 1-3F).

αF-helix. αF-helix serves as the main anchor in the kinase C-lobe. It contains several hydrophobic residues and remains stable in the kinase catalysis reaction.

In addition to the conserved kinase core and motifs, PKA contains two tails tethered to either N- and C-terminal (N-tail and C-tail) of the kinase core (Figure 1-3C). These two tethering tails, where the C-tail is conserved in all AGC kinases, interact with the kinase core and are crucial for kinase regulations. There are also several post-modification sites in PKA C-subunit. The glycine residue at the N-terminus, Gly1, is myristylated, and the myristylation sites are essential for membrane anchoring. In addition, the deamidation on Asn2 is important for C-subunit localization. The auto-phosphorylation site, $Thr197^{C}$, is critical for PKA structural integrity and kinase activity, and $Ser338^{C}$ near the C-terminus is constitutively phosphorylated in PKA and essential for assembly of the active kinase(7).

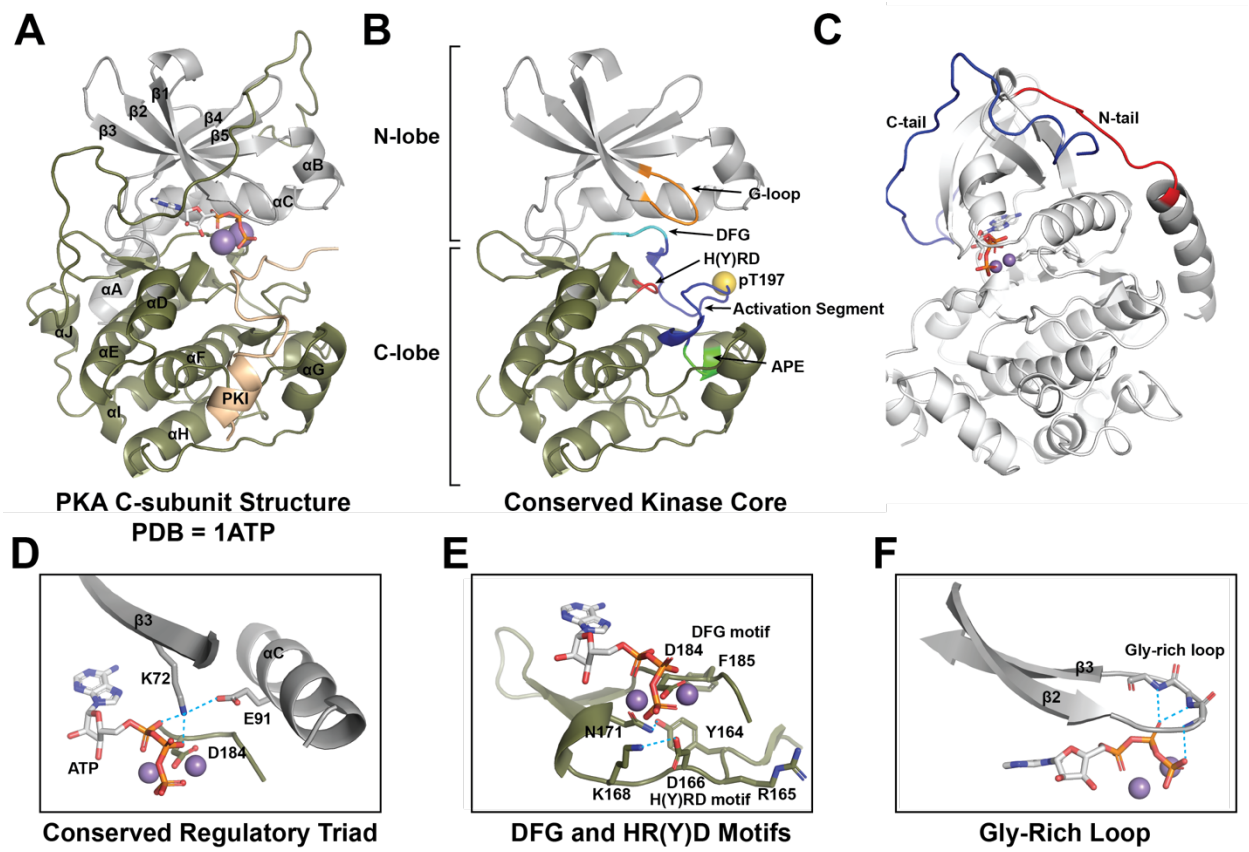

Figure 1-3. Protein kinase has several conserved motifs. (A) PKA C-subunit. (B) Conserved N- and C-lobes. (C) N- and C-tails. (D) Conserved regulatory triad. (K72, E91 and D184 in PKA C-subunit.). (D) DFG and H(Y)RD motifs. (F) Glycine rich loop.

Although the N-lobe in the apo C-subunit is highly flexible, in the presence of both ATP/Mg^{2+} and substrate, the ATP phosphates and Mg^{2+} ions are precisely positioned by a conserved regulatory triad ($Lys72^{C}$, $Glu91^{C}$, $Asp184^{C}$), which align the γ-phosphate for transfer to substrate(8) (Figure 1-3D). Binding ATP/$2Mg^{2+}$ and substrate induces a 'closed conformation', while in the absence of ATP and substrate, the more dynamic small lobe stays in an 'open conformation' (9).

1.2 PKA R-subunit

In humans, there are four functionally non-redundant R-subunit isoforms (RIα, RIβ, RIIα, RIIβ), that share the same domain organization (Figure 1-4). An N-terminal dimerization and docking domain (D/D domain) is connected by a flexible linker to two tandem C-terminal cyclic nucleotide binding (CNB) domains. Embedded within the flexible linker is an inhibitory sequence that binds to the C-subunit active site thereby preventing substrate binding(5, 10). The main distinction between RI and RII is their inhibitory sequences; RI subunits have a pseudo-substrate inhibitor motif while in RII subunits this motif is a substrate that can be phosphorylated by the C-subunit. The D/D domain is a four-helix bundle that is essential for dimerization and binding to A-Kinase-Anchoring-Proteins (AKAPs)(11, 12). Deletion of the D/D domain creates a monomeric R-subunit, which cannot be properly localized in cells, and most of the allosteric features of cAMP activation are also lost(13-16).

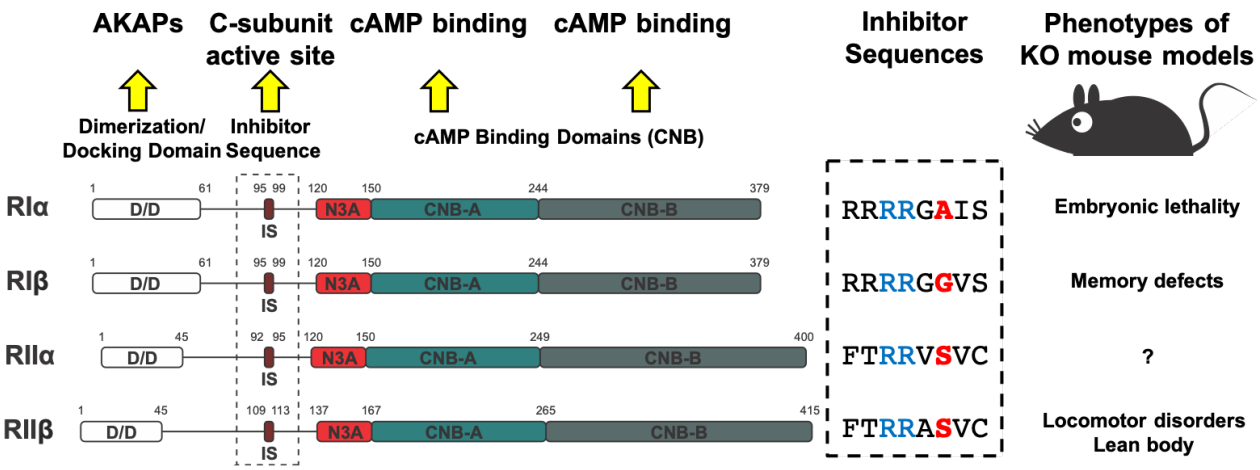

Figure 1-4. Functional non-redundant PKA R-subunits.

Each CNB domain contains α- and β-subdomains. The β-subdomain is a classic β-sandwich with a helical phosphate-binding cassette (PBC), embedded between the β7/β8-strands, and this is a signature motif for cAMP binding. The α-subdomain consists of three helical motifs - the PBC, the N-terminal N3A-motif (αN-helix, 3_{10}-loop, and αA-helix), and the C-terminal αB/C-helix. The helical subdomains undergo significant conformational changes during PKA activation(16-18). Specifically in the holoenzyme the kinked αB- and αC-helices in CNB-A fuse with the αN-helix in CNB-B to form a single αB/C/N-helix which defines the transition between the cAMP bound state (B-form) and the holoenzyme (H-form)(16, 18). In the H-form, the cAMP binding site in CNB-A is shielded by the R-C interface; in the RIα holoenzyme cAMP cannot bind to CNB-A until cAMP binds to the CNB-B domain, which acts as a 'gate keeper' for CNB-A(13, 19).

Although all four PKA R-subunits share similar sequence and domain organization, they are functionally non-redundant, and the holoenzymes have different quaternary structures(5, 16, 20-23). The various R subunits are also differentially expressed in different tissues. RIα and RIIα are ubiquitously expressed, while RIβ and RIIβ are more tissue specific (40–42). RI- subunits, like the cAMP-dependent protein kinase inhibitor (PKI), is a pseudo-substrate, while RII-subunits have a phosphorylation site (P-site) in the inhibitory sequence that undergoes single turn-over catalysis in the holoenzyme(5, 24). The R-subunits and their corresponding holoenzymes also differ in their biochemical properties, cAMP sensitivities, and localization(9, 14). In mouse models, depletion of RIβ causes memory defects(25), while RIIβ knockout mice have locomotor disorders and a lean phenotype(26, 27) (Figure 1-4). RIα, however, is the only R isoform that shows embryonic lethality in mouse knockout models(28, 29). In this thesis, we will focus on RIα and RIIβ holoenzymes (Figure 1-5).

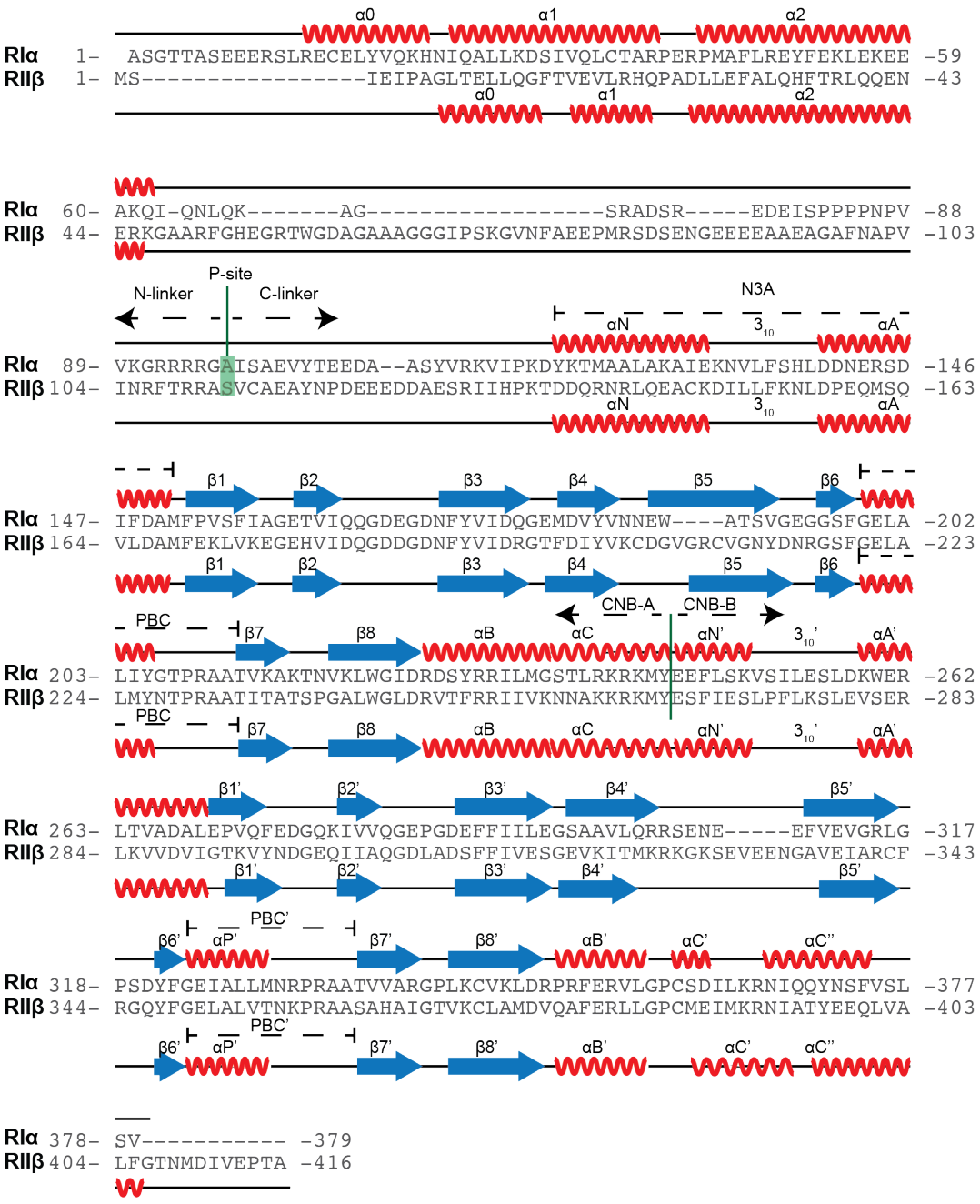

Figure 1-5. Sequence and secondary structure of PKA R-subunits.

1.3 PKA-related diseases

As key regulators in the cell signaling pathways, any impairments in the protein kinase can easily disrupt the balance of cell signaling and further lead to diseases. Therefore, many diseases-associated mutations in protein kinases have been identified. For examples, point mutations in B-Raf, a proto-oncogene Serine/Threonine kinase, can lead to lymphoma, colon cancer, melanoma, lung and brain tumors etc(30). Several studies have also shown that most patients with non-small cell lung cancer have overexpression of or point mutations in EGFR, a growth-factor-receptor tyrosine kinase, and the drugs that specifically target to EGFR are effective to inhibit tumor growth(31). Overexpression of HER2, a receptor tyrosine protein kinase, can be found in most of the aggressive breast cancers(31). Recent advances in neurodegenerative disease studies also reveal that point mutations in protein kinases such as PINK1 and LRRK2 can lead to Parkinson's disease.

In addition to point mutations or expression level impairments being drivers of many diseases, several kinase fusion protein mutations have been identified as drivers of cancers. All patients with chronic myeloid leukemia (CML) have a genetic fusion mutation, BCR-ABL(32). Other protein kinase fusion proteins, EML4-ALK, can link to non-small lung cancer(33). DnaJB1-PKAc, a fusion protein of DnaJB1 and the PKA C-subunit, is a cancer driver mutation of fibrolamellar hepatocellular carcinoma (FL-HCC)(34). Given the abundance of oncogenic kinases, many kinase inhibitors have been developed as therapeutic tools, and numerous inhibitors are used clinically or in clinical trials. Here, we will focus on the disease-associated mutations on PKA.

1.3.1 Disease mutations in the R-subunits

Most PKA-related disease mutations are in RIα: Carney Complex (CNC) disease results from an increase in PKA activity (35, 36), while acrodysostosis (ACRDYS) patients show hormone resistance and lower PKA activity(37, 38). The patients with Carney complex disorder have higher risk of developing benign tumors. Most of them carry *PRKAR1A* (gene of RIα) mutants, which result in either nonsense-mediated mRNA decay (NMD) or enhanced activation by cAMP. Thus, in CNC, PKA is easier to be activated or displays enhanced sensitivity to cAMP compared to normal tissues, and this leads to cell proliferation and the disease. In contrast, acrodysostosis patients are more resistance to cAMP and thus have lower PKA activity. Acrodysostosis are caused by mutations in *PRKAR1A* (type 1) or *PDE4D* (type 2). The symptoms in patients with acrodysostosis may include short digits, hormone resistance, and abnormal bone growth. This combined data suggests that RIα is the most essential R-subunit and can be considered as the 'master regulator' of PKA signaling. A chimera protein, RIα-RET, by the fusion of RIα and a receptor tyrosine kinase RET, has been also identified in patients with papillary thyroid carcinoma (PTC)(39).

A recent study has shown that *PRKAR1B* (gene of RIβ) is associated with of a new type neurodegenerative disorder(40). A mutation (Leu50Arg) located at the D/D domain of the RIβ has been identified in patients. This mutation presumably can either affect AKAPs binding and/or destabilize the D/D resulting in insoluble protein and aggregation in cells.

1.3.2 Disease mutations in the C-subunit

Cushing's disease, which is caused by secreting too much adrenocorticotropic hormone (ACTH) from pituitary adenoma, is an acute endocrine disorder associated with cortisol pathway and inflammation. Exome sequencing has identified the genetic mutations of PKA C-subunit are

associated with Cushing's disease(41). The mutations either show the defective inhibition of PKA C-subunit mutants by the PKA R-subunit, or higher protein expression level of PKC C-subunit. In both cases, the basal PKA activity is increased. Compare with the wt PKA C-subunit, Cushing's disease mutants not only have lower binding affinity with the PKA R-subunits but can also can alters its substrate specificity(42).

Fibrolamellar hepatocellular carcinoma (FL-HCC) is a rare liver cancer that commonly occurs in young adults with no chronic liver disease history. Recent studies of FL-HCC identified a unique kinase mutation, DnaJB1-PKAc (J-C) in most of patients. This mutation due to a ~400 kilobase pair deletion on chromosome 19, forms a chimeric transcript of the *DNAJB1* exon 1 fused with the *PRKACA* exons 2-10(34). The mutant is translated as a stable protein where the J-domain (residues 1-69) of DnaJB1 is fused to the Protein Kinase A (PKA) catalytic (C) subunit (PKAc) (residues 15-336) (Fig. 1A). This fusion protein is uniquely expressed in the tumor tissues, but not in adjacent normal tissues in FL-HCC patients. Moreover, mouse models, generated using CRISPR-Cas9 gene modification, have confirmed that this chimeric protein, DnaJB1-PKAc, is oncogenic(43, 44).

Structural studies of DnaJB1-PKAc and Cushing's disease PKA C-subunit mutants showed that their kinase core structures are nearly identical to wild-type (wt) PKAc, although DnaJB1-PKAc has four extra helices at the N-terminus adjacent to the αA-helix, and the proteins have similar biochemical properties(45). Transcriptome research has also shown that the gene expression and protein levels of the R-subunits are strongly affected in FL-HCC(46). In normal liver tissue, RIIβ is the predominate R-subunit(47). In tumors, however, RIα mRNA and protein levels are up-regulated while RIIβ mRNA and protein levels are decreased compared to the normal liver tissue(46, 48).

Chapter 2 PKA RIα holoenzyme structure reveals isoform-specific mechanism

Here we captured in crystal structures two conformational states of the PKA RIα holoenzyme. These two conformations, distinguished by the presence and absence of ATP, show how ATP plays an essential role in allosteric regulation. Because RIα is a pseudo-substrate, ATP can function as a high affinity orthosteric inhibitor instead of a substrate, while cAMP serves as a competing allosteric activator for the RIα holoenzyme. Our structures, together with biochemical studies show how the opposing competition of two nucleotides defines a unique allosteric regulatory mechanism in the RIα holoenzyme. In contrast, for the RII-holoenzymes ATP is a substrate that actually facilitates cAMP activation/dissociation. The quaternary structures, mechanism for cAMP-mediated activation, and the role of ATP are thus quite distinct for RIα and RIIβ. Molecular dynamic (MD) simulations and biochemical assays not only shed further light on the extended allosteric network that leads to activation of the RIα holoenzyme but also highlight differences with the RIIβ holoenzyme. The N3A-N3A' dimerization motif in the CNB-A domain is a unique feature of RI holoenzymes and serves as an allosteric hub for communication between the four CNB domains (CNB-A, CNB-B, CNB-A' and CNB-B'). $Glu200^{RI\alpha}$, a conserved cAMP binding residue in the PBC, also interacts directly with the N3A-N3A' motif in RIα holoenzymes but not in RIIβ holoenzymes, and this contributes directly to the allosteric mechanism for activation of RIα. Given that the R_2C_2 holoenzymes represent the relevant physiological complex

in vivo, these holoenzyme structures provide fundamental new insights into isoform-specific cAMP signaling in cells and reveal the potential role of PKA as an energy sensor.

2.1 RIα holoenzyme structures are captured in two distinct states

The RIα holoenzyme structure solved at 3.55Å (Table 2-1), captured two distinct conformations of holoenzyme in the asymmetric unit (Figure 2-1A-C). Each conformation of RIα holoenzyme is composed of one RIα dimer and two C-subunits. Although in both holoenzymes the full-length proteins are present in the crystal, based on SDS-PAGE (Figure 2-1D), the D/D domain and part of N-linker are not visible in the electron density map, most likely because the N-linker is flexible. Both holoenzyme conformations have the same R-C interface that was also defined previously in the crystal structure of (Δ1-91)RIα(Arg333^{RIα}Lys):C which represents an R:C complex with a truncated RIα(16).

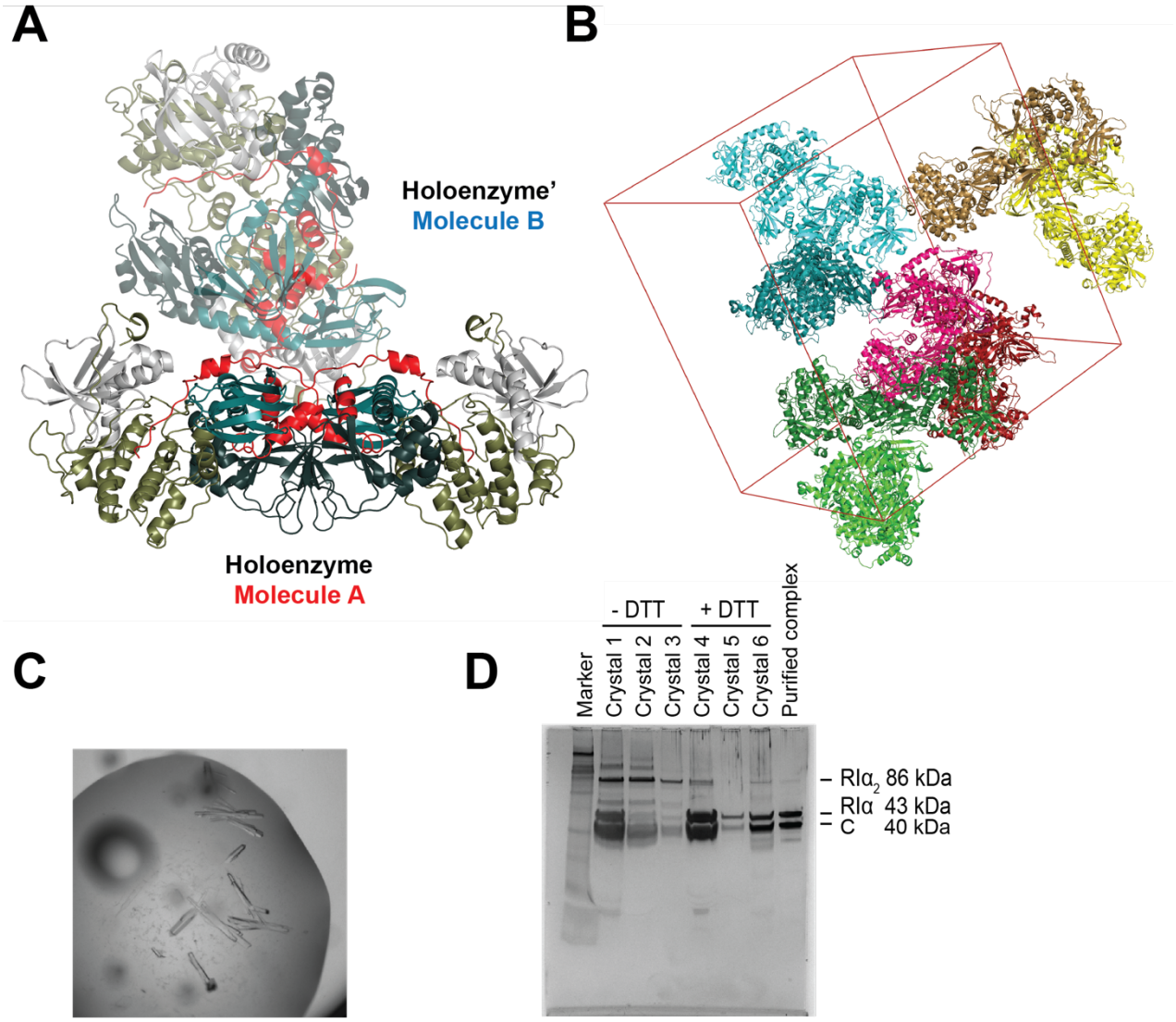

Figure 2-1. Crystal structure of the RIα holoenzyme. (A) Asymmetric unit. (B) Crystal packing. (C) Crystal. (D) Silver stained of crystals.

Table 2-1. Crystallography data collection, refinement and validation statistics.

Structure: RIα$_2$C$_2$	
Data collection	
Space group	$P2_12_12_1$
Cell dimensions	
a, *b*, *c* (Å)	139.8, 184.8, 183.4
α, *β*, *γ* (°)	90, 90, 90
No. molecules per ASU	2
Resolution (Å)	50.0-3.55 (3.63-3.55)
R_{merge}	0.126 (0.49)
I/sigma	7.6 (1.7)
Completeness (%)	87.0 (80.7)
No. reflections	58,193
Refinement	
PDB code	6NO7
Resolution (Å)	50.0-3.55
R_{work}/R_{free} (%)	25.6/26.9
RMSD	
Bond lengths (Å)	0.013
Bond angles (°)	2.0
Ramachandra angles (%)	
Favored	95.1
Disallowed	0
Twin operator	*-h*, *l*, *k*

In the full-length holoenzyme structures described here (Figure 2-2A), new holoenzyme interfaces are revealed. Although both structures are formed by two RIα:C complexes with the two CNB domains (CNB-A/CNB-B and CNB-A'/CNB-B') facing each other in an anti-parallel orientation, the two conformations nevertheless have distinct differences in this interface between the two R-subunits. In Molecule A, the N3A-motif/N3A'-motif interaction (N3A-N3A') four helix bundle nucleates the dimer interface, and this is the dominate feature that we observed earlier in the RIα dimer (Figure 2-2B). The other conformation, Molecule B, has a smaller interface which is mediated by the interactions of αN-helix/αN'-helix (αN-αN') (Figure 2-2C).

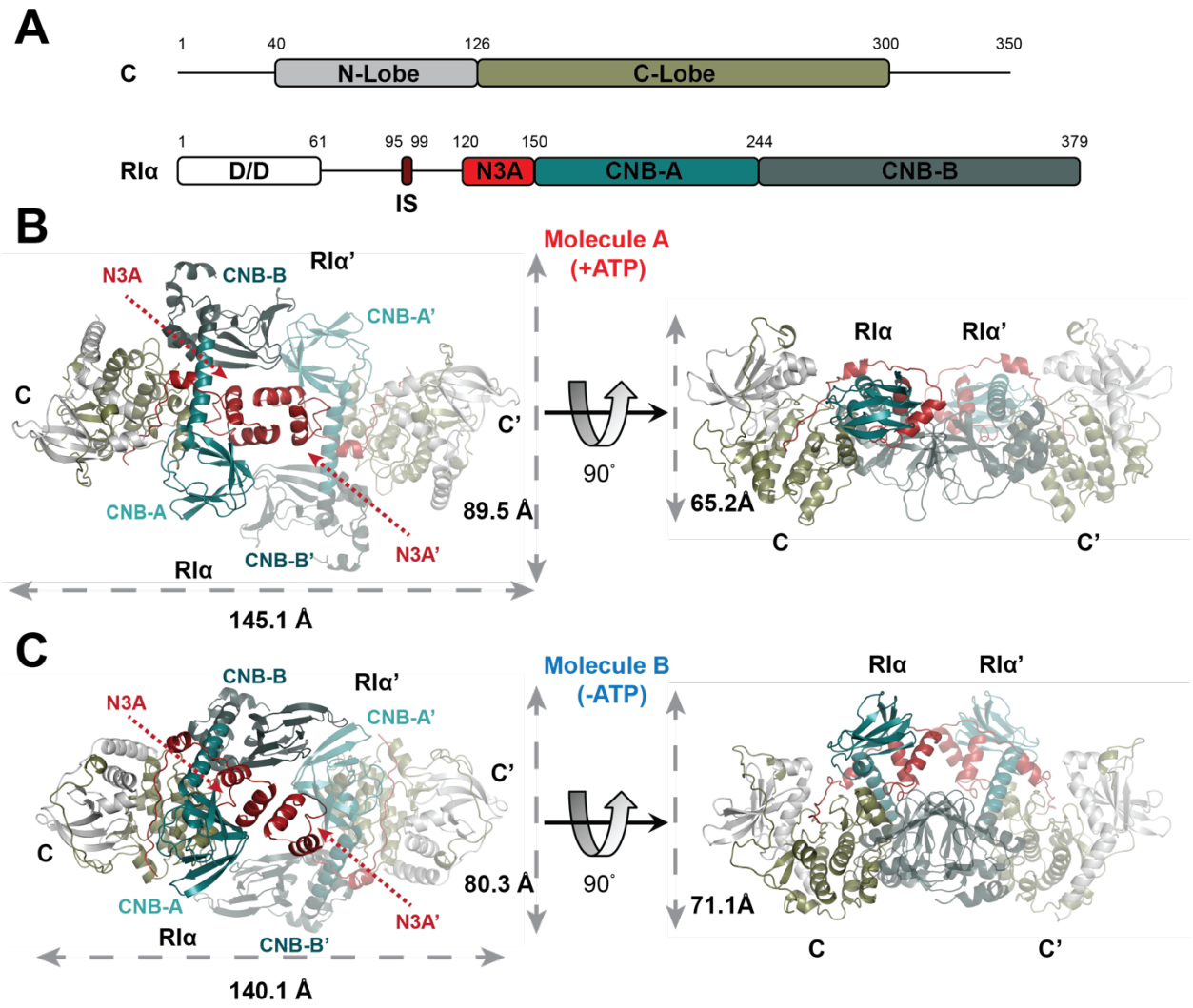

Figure 2-2. Crystal structure of two RIα holoenzyme conformations. (A) Domain diagram. (B) Structure of Molecule A. (C) Structure of Molecule B.

2.2 Role of ATP/Mg^{2+} in the holoenzyme conformation

The C-subunits in both holoenzyme structures all show 'closed' conformations. In Molecule A, each C-subunit is bound to ATP/Mg^{2+} and the inhibitory sequence of RIα, while ATP and Mg^{2+} are missing in Molecule B (Figure 2-3). The hydrodynamic radius (R_H), radius of gyration (R_g), and maximum dimension (D_{max}) of both holoenzyme structures were determined using size-exclusion chromatography and Small-Angle X-ray Scattering (SAXS) (Figure 2-4 and Figure 2-5)(49). To mimic Molecule A in solution, the holoenzyme was formed in the presence of excess ATP ('ATP-bound' state). When holoenzyme was formed in the absence of ATP under the same conditions, a reduction in the relative amount of holoenzyme ('ATP-off' state) was observed, indicating that ATP plays a key role in formation of the $RI\alpha_2C_2$ complex (Figure 2-5A).

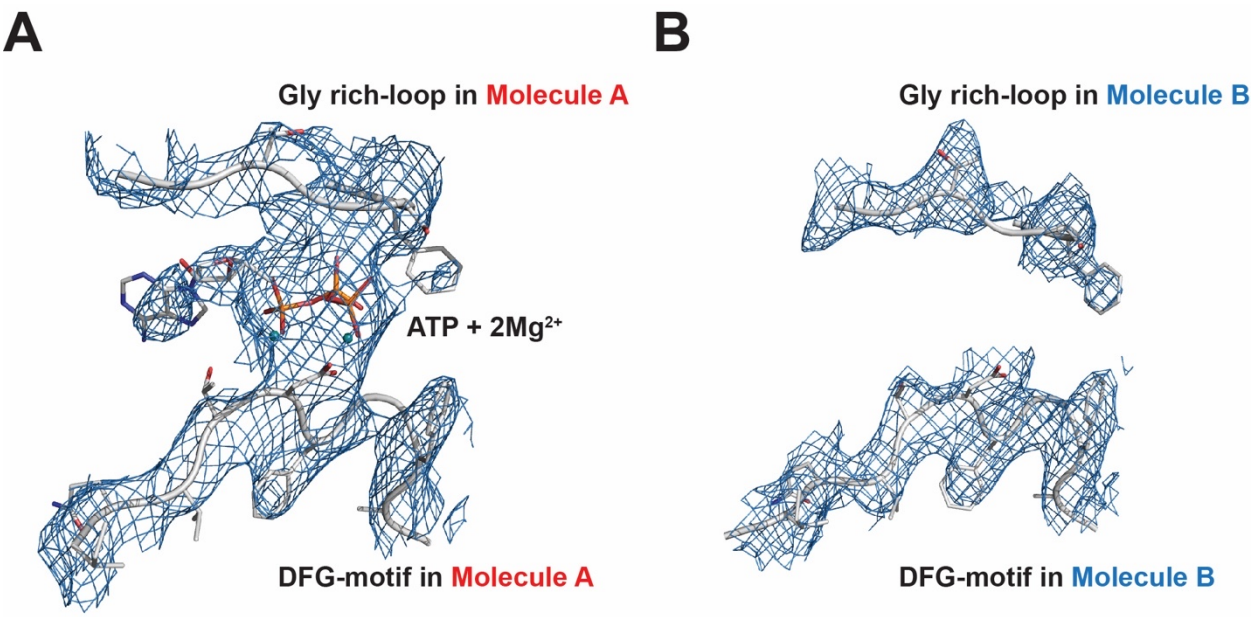

Figure 2-3. Density map of ATP binding site of the RIα holoenzyme. (A) 2Fo-Fc at density map of ATP site at 0.9σ level in Structure A. (B) 2Fo-Fc density map at 0.9σ level of ATP site in Structure B.

Based on these two chromatography profiles, two distinct holoenzyme complexes were observed. Molecule A in the presence of ATP eluted first, suggesting that the conformation of Molecule B is more compact. The hydrodynamic radius confirms that the 'ATP-bound' Molecule A is more elongated (R_H = 55.39Å), while the 'ATP-off' Molecule B is more compact (R_H = 48.15Å) (Figure 2-4). Structures A and B have Perrin Shape factors of 1.53 and 1.33, respectively, indicating that both have 'oblate' shapes, which is consistent with the crystal structures. The calculated dimensions of Molecule A are 145.1 × 89.5 × 65.2 Å, versus 140.1 × 80.3 × 71.1 Å for Molecule B (Figure 2-2B and C).

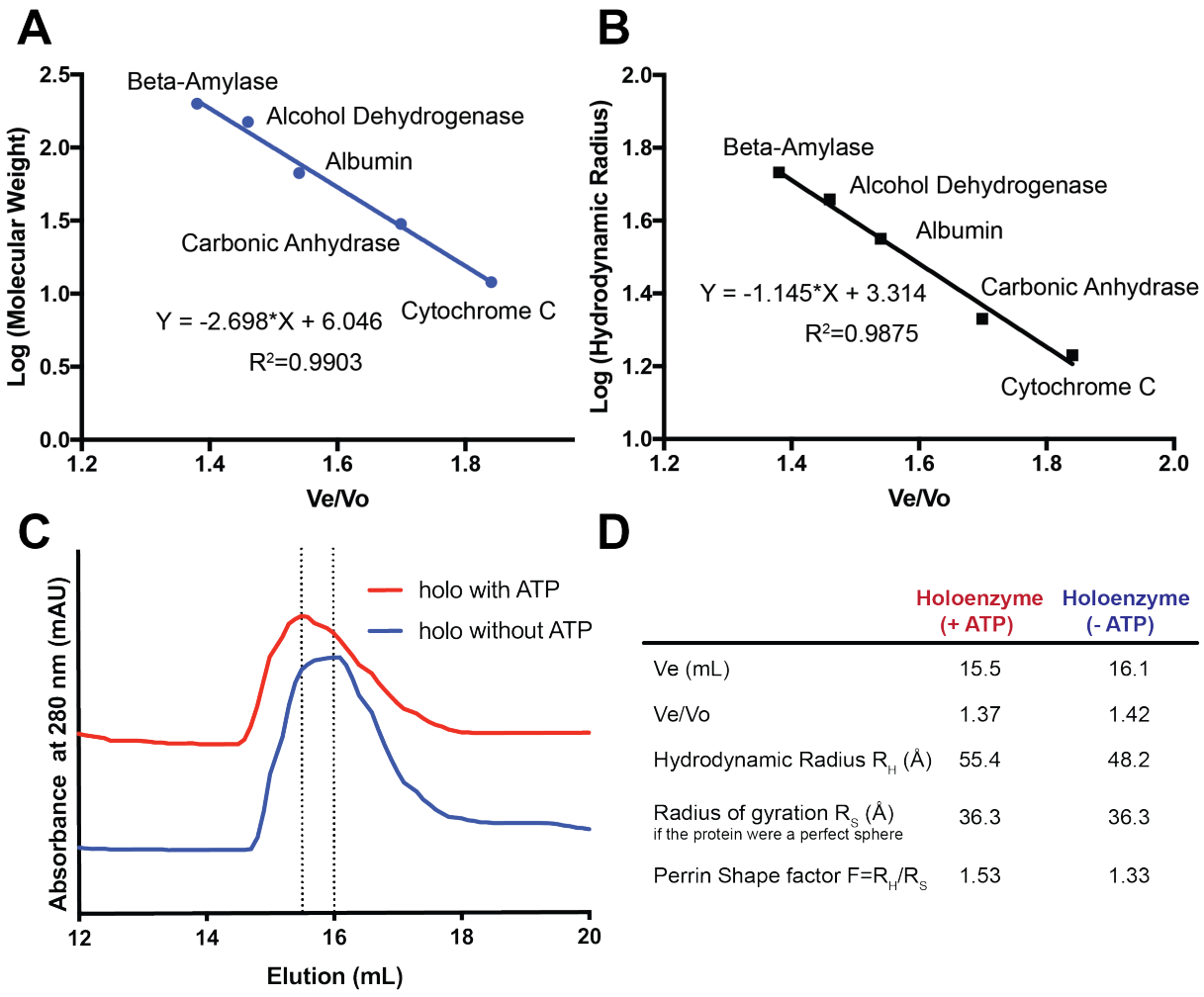

	Holoenzyme (+ ATP)	Holoenzyme (- ATP)
Ve (mL)	15.5	16.1
Ve/Vo	1.37	1.42
Hydrodynamic Radius R_H (Å)	55.4	48.2
Radius of gyration R_S (Å) if the protein were a perfect sphere	36.3	36.3
Perrin Shape factor $F=R_H/R_S$	1.53	1.33

Figure 2-4. Hydrodynamic radius analysis of two RIα holoenzyme conformations. (A) Standard curve of molecular weight. (B) Standard curve of hydrodynamic radius. (C) Gel filtration profile of RIα holoenzyme in the presence and absence of ATP. (D) The hydrodynamic radius of RIα holoenzyme in the presence and absence of ATP.

Similar results were observed with SAXS where RIα holoenzyme scattering profiles were measured in the absence and presence of ATP (Figure 2-5B). Holoenzyme in the presence of ATP is slightly larger (R_g = 52.08Å, D_{max} = 160Å, and Porod volume = 269000Å^3), based on pair-distance distribution functions *P(r)*, than the apo holoenzyme (R_g = 51.18Å, D_{max} = 154Å, Porod volume = 260000Å^3). Similar R_g values can also be obtained from Guinier analysis (R_g = 52.39Å and R_g = 48.94Å for Molecule A and Molecule B, respectively). The SAXS analyses are consistent with the hydrodynamic radius and theoretical R_g calculations based on the crystal structures. Both crystal and solution state structures thus confirm that ATP induces a conformational change in the RIα holoenzyme (Figure 2-5C), and that ATP specifically promotes a more extended conformation. The importance of ATP and Mg^{2+} ions has been discussed in prior studies. The ATP dissociation rate, for example, is in the same time range as R-C dissociation (13, 50), indicating that these two processes are probably linked. In the absence of ATP, the R-C dissociation rate is significantly reduced. However, the detailed mechanism and the exact role of ATP for RIα holoenzyme homeostasis is not yet clear.

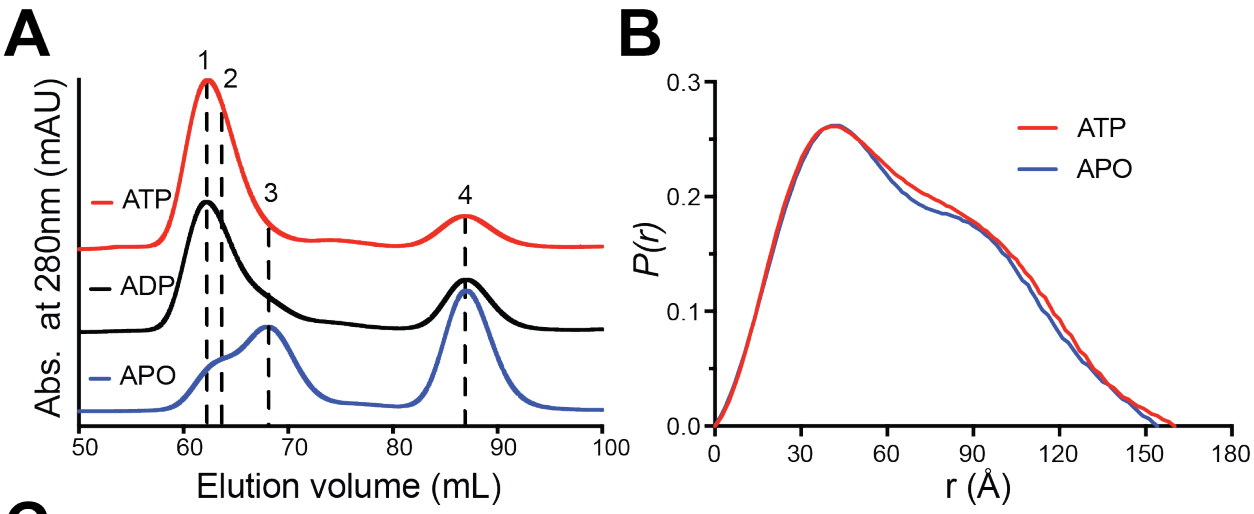

C

	Molecule A (+ATP)	Molecule B (-ATP)
Crystal structure dimensions (Å^3)	145.1 x 89.5 x 65.2	140.1 x 80.3 x 71.1
Hydrodynamic radius (Å)	55.39	48.15
R_g (Å) from crystal structure*	42.35	38.35
R_g (Å) from Guinier	52.39 ± 0.38	48.94 ± 0.14
R_g (Å) from *P(r)*	52.08 ± 0.11	51.18 ± 0.33
D_{max} (Å) from *P(r)*	160	154
Porod volume (Å^3) from *P(r)*	269000	260000

*The R_g values are smaller than experimental values, as D/D domain is unstructured in both conformations

Figure 2-5. The RIα holoenzyme has different conformations in the presence and absence of ATP. (A) Gel filtration profile of RIα holoenzyme in the presence and absence of ATP. (B) SAXS analysis of RIα holoenzyme in the presence and absence of ATP. (C) Different conformation of RIα holoenzymes in the presence and absence of ATP.

2.3 ATP regulation of the RIα holoenzyme

To further understand the allosteric features of how ATP regulates the conformational state and cAMP activation of the RIα holoenzyme, a fluorescence polarization (FP) assay was used to determine the role of ATP in cAMP-mediated dissociation and holoenzyme formation. By titrating a fluorophore-labeled C-subunit with RIα, the ratio of holoenzyme formation can be determined from the FP changes. R-C association was measured under apo conditions or in the presence of ADP or ATP. RIα showed strong binding with C-subunit in the presence of ADP or ATP (EC_{50} = 4.6 or 5.0 nM), in contrast to holoenzyme formed in the absence of nucleotide (EC_{50} = 12.5 nM) (Figure 2-6A and E). Although this assay is sufficient to show that interactions of the subunits are reduced in the absence of nucleotide, due to the limits of detection (5 nM), this assay cannot discriminate between the actual dissociation constants (K_d) in the presence of ADP vs. ATP. Both our results and previous studies indicate that ATP influences RIα holoenzyme formation(13)

Nucleotide also plays a significant role in cAMP-mediated holoenzyme dissociation. Starting from 100% inactive holoenzyme, cAMP was titrated in under apo conditions or in the presence of ADP or ATP. RIα holoenzyme is less sensitive to cAMP in the presence of ATP; the holoenzyme is easier to dissociate by the trigger of cAMP when there is no ATP or ADP present (Figure 2-6B and E). Interestingly, even though the R- and C-subunit in the holoenzyme show strong affinity in the presence of ADP, the RIα holoenzyme also has low tolerance to cAMP in the presence of ADP. It is ATP and two Mg^{2+} ions that specifically facilitates RIα holoenzyme formation and stabilizes its holoenzyme complex to have a higher threshold for cAMP activation. This also supports earlier Biacore measurements that show a significant difference between ATP and ADP as well as the importance of the second metal ion(51).

Our functional studies indicate that that Molecule B ('ATP-off' state) represents a conformation that is easier to be activated with cAMP while Molecule A ('ATP-bound' state) has a higher threshold for activation by cAMP. Thus, both nucleotides, ATP and cAMP, can contribute to regulation cAMP-mediated dissociation of the RIα holoenzyme.

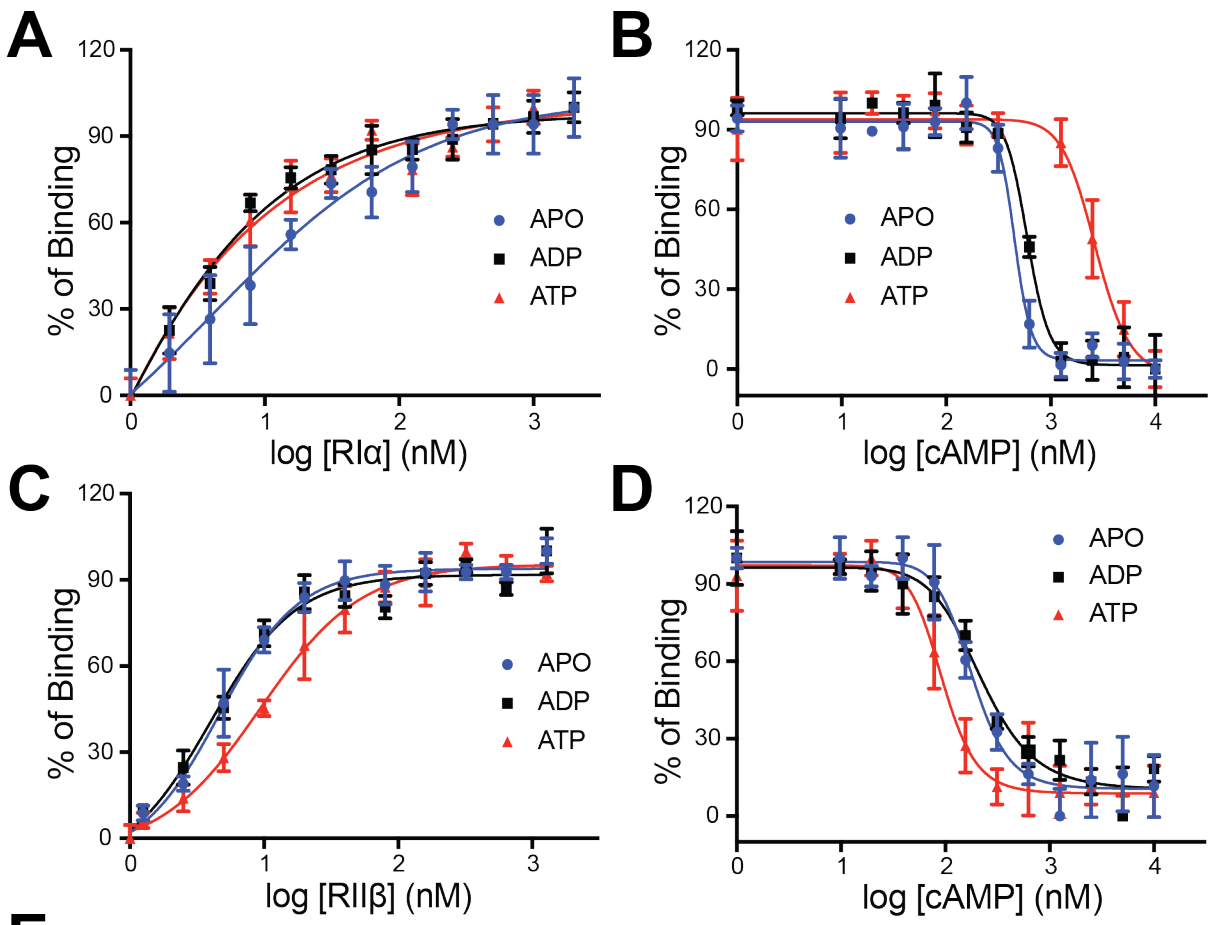

E

	RIα			RIIβ		
	APO	ADP	ATP	APO	ADP	ATP
R-C Affinity						
EC50 (nM)	12.45 ± 2.96	4.63 ± 0.56	5.05 ± 0.84	5.21 ± 0.40	4.77 ± 0.43	10.32 ± 1.00
Hill Slope	0.81 ± 0.14	1.11 ± 0.13	0.98 ± 0.15	1.62 ± 0.17	1.57 ± 0.18	1.24 ± 0.13
cAMP Activation						
EC50 (nM)	457.6 ± 26.2	599.5 ± 26.7	2643 ± 308.7	182.6 ± 18.3	218.0 ± 27.7	94.1 ± 9.1
Hill Slope	5.59 ± 0.91	4.09 ± 0.91	2.62 ± 0.69	2.40 ± 0.51	1.68 ± 0.32	2.76 ± 0.63

Figure 2-6. Isoform-specific allostery. (A) In RIα, ATP facilitates RIα-C binding. (B) RIα holoenzyme is less sensitive to cAMP when there is ATP. (C) ATP destabilizes RIIβ-C binding. (D) In the presence of ATP, RIIβ holoenzyme is easier to activate with cAMP. (E) ATP has isoform-specific effect on RIα and RIIβ.

2.4 ATP regulation of PKA holoenzymes is isoform-specific

ATP plays a different role in regulation of the RIIβ holoenzyme. In addition to being an inhibitor of the C-subunit activity, RIIβ is also a single-turn-over substrate since in the RIIβ holoenzyme the P-site in the inhibitory sequence is phosphorylated when ATP is present (24). Using FP assay the RIIβ holoenzyme displayed weaker affinity in the presence ATP (EC50 = 10 nM), compared to in the apo and ADP conditions (EC50 ~ 5nM) (Figure 2-6C and E). This is opposite to the RIα holoenzyme and indicates that affinity is modulated by phosphorylation of the substrate site. Considering the FP assay's detection limit is, the difference in K_d in the absence of ATP is likely to be at least an order of magnitude (0.6 nM vs. 5 nM) for the full-length protein(52). In cAMP activation assays, the RIIβ holoenzyme is less sensitive to cAMP in the presence of ADP or apo conditions (EC50 ~ 200 nM); while dissociation is more readily triggered by cAMP in the presence of ATP (EC50 = 94 nM) (Figure 2-6D and E). ATP thus primes the RIIβ holoenzyme for cAMP-mediated dissociation by phosphorylation of the substrate site in contrast to the stabilizing effects of ATP on the RIα holoenzyme.

In contrast to RIα holoenzyme, size-exclusion chromatography showed that all RIIβ holoenzymes eluted at the same elution volume; there are no ATP dependent conformational changes and ATP is not required to form a stable RIIβ holoenzyme complex (Figure 2-7A). Previous crystal structures also have shown similar results, apo $RII\beta_2C_2$ (PDB 3TNP) and ADP-bound/phosphorylated $RII\beta_2C_2$ (PDB 3TNQ) have essentially the same quaternary structures (Figure 2-7B) (22). ATP thus plays a critical role in both RIα and RIIβ, yet the effects are different.

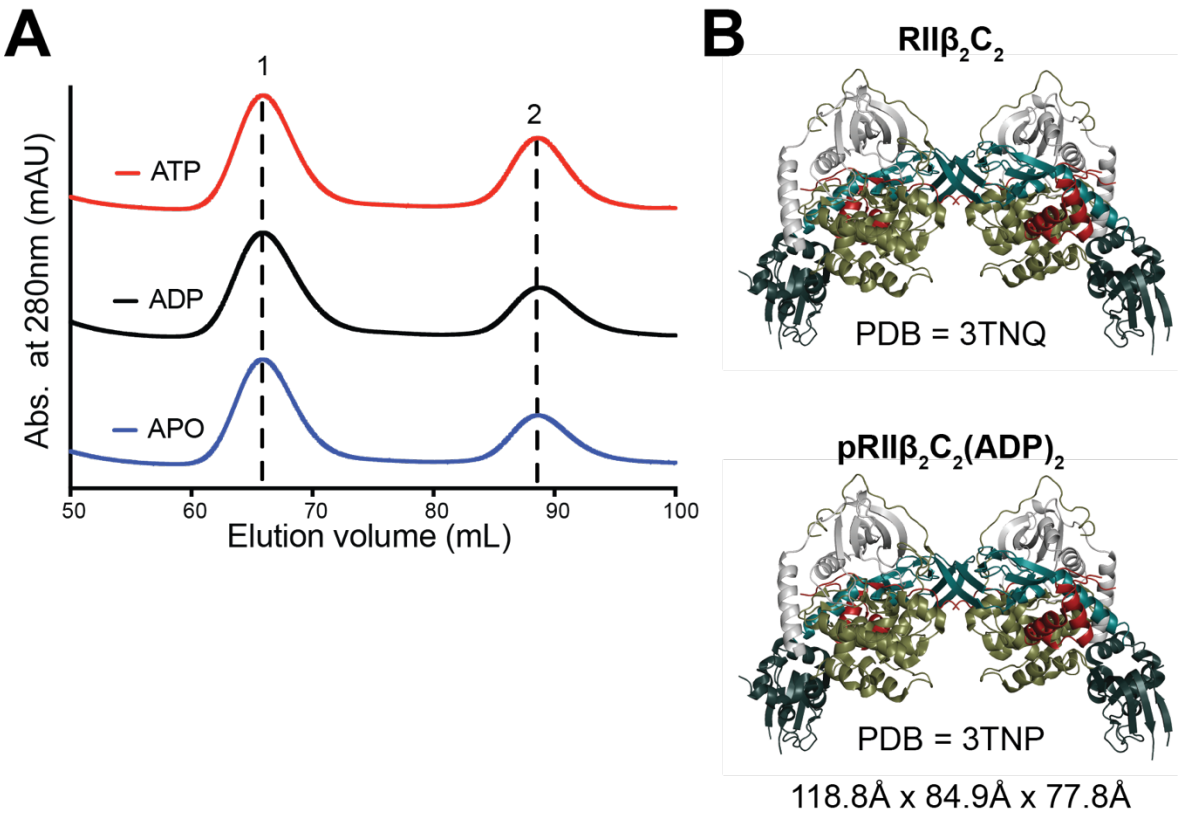

Figure 2-7. ATP has no effect on the RIIβ holoenzyme conformational changes. (A) RIIβ holoenzymes have similar hydrodynamic radius in the presence and absence of ATP. (B) Apo form and phosphorylated/ADP bound form of RIIβ holoenzyme have similar conformations.

2.5 The two conformations of the RIα holoenzyme show different subunit dynamics

2.5.1 C-subunit

To further investigate the dynamic differences between the two RIα holoenzyme conformations, 500ns MD simulations were carried out (Fig. S7, A and B). The C-subunits in each conformation have different propensities to stay in open and/or closed states. Kinases' open and closed conformations represent their substrate recognition and release states. Here, the closed, intermediate, and open conformations are defined by the distance of the α-carbon from $Lys72^{C}$ on the β3-strand to $Ala223^{C}$ on the αF-helix (Figure 2-8A)(53-55). The $Lys72^{C}$-$Ala223^{C}$ distance of each C-subunit in the two holoenzymes were determined throughout the trajectories. In Molecule A, which has the N3A-N3A' interface, both C-subunits remained stable with low fluctuation (Standard deviation (S.D.) = 0.404 and 0.426Å) (Figure 2-8B). In contrast, the distance of $Lys72^{C}$-$Ala223^{C}$ in each C-subunit of Molecule B showed significantly greater fluctuations (S.D. = 0.961 and 0.711Å), suggesting that the C-subunits are more dynamic, and that the open state is more accessible (Figure 2-8C). The higher flexibility of C-subunits in Molecule B further validates the experimentally observed weaker binding with the inhibitory site of the R-subunit in the absence of ATP.

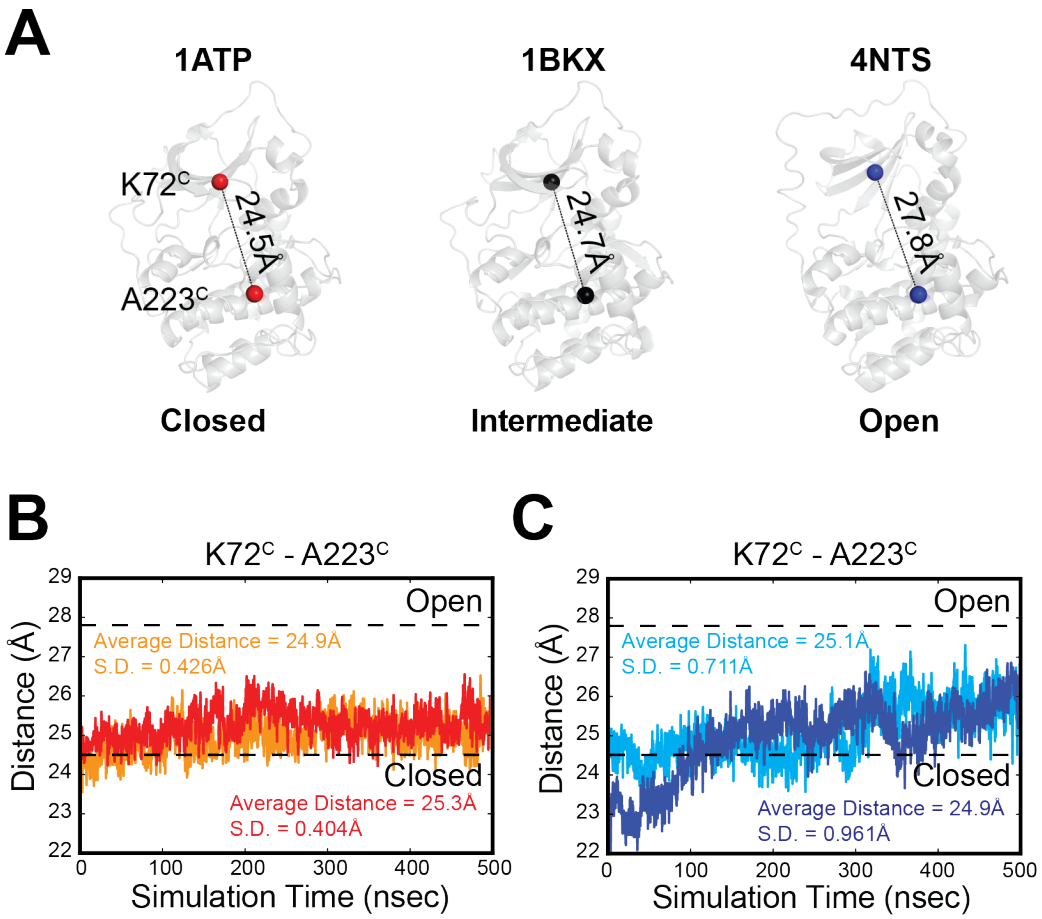

Figure 2-8. Two RIα holoenzyme conformations have distinct C-subunit dynamics. (A) Closed, intermediate and open states of PKA C-subunit. (B) The distance between $K72^{C}$-$A223^{C}$ remain stable in Molecule A. (C) In the absence of ATP, the distance between $K72^{C}$-$A223^{C}$ are flexible in Molecule B.

2.5.2 R-subunit

R-subunit dynamics are important for holoenzyme activation, as highlighted by the extended αB/C/N-helix in the holoenzyme in contrast to the kinked helices in the cAMP-bound R-subunits. Several studies have characterized the dynamic features of the αB/C/N-helix including a 'flipped-back' model for PKA activation (56-58). The thermodynamic properties of the two CNB domains are critically intertwined and sensitive to ligand binding as well as mutation of the neighbor (59). Both mutagenesis and simulations have shown that the helical propensity of the αB/C/N-helix correlates with R-C dissociation in the (Δ1-91)RIα:C complex(60). The 'flip-back' model of the R-C complex, which has been observed in long MD simulations, also highlights the dynamic properties of the αB/C/N-helix and the CNB domains for PKA activation(61).

The R-subunits in each structure also show distinct dynamic features. Although the extended αB/C/N-helix is strengthened by the RC:R'C' interface in our structures, and we did not observe a 'flip-back' conformation in the simulation, different αB/C/N-helix dynamics were observed in the two conformations. In Molecule A, the R-subunits are stable, and their αB/C/N-helices remain 100% helical throughout the simulation, which likely keeps the holoenzyme in an inactive 'locked-state' (Figure 2-9A and B). However, one of the αB/C/N-helices in the Molecule B simulations shows partial unwinding indicating the αB/C/N-helix is more flexible (Figure 2-9C and D). For this reason, we think that Molecule B can be considered as an intermediate state, which can be activated more readily by cAMP.

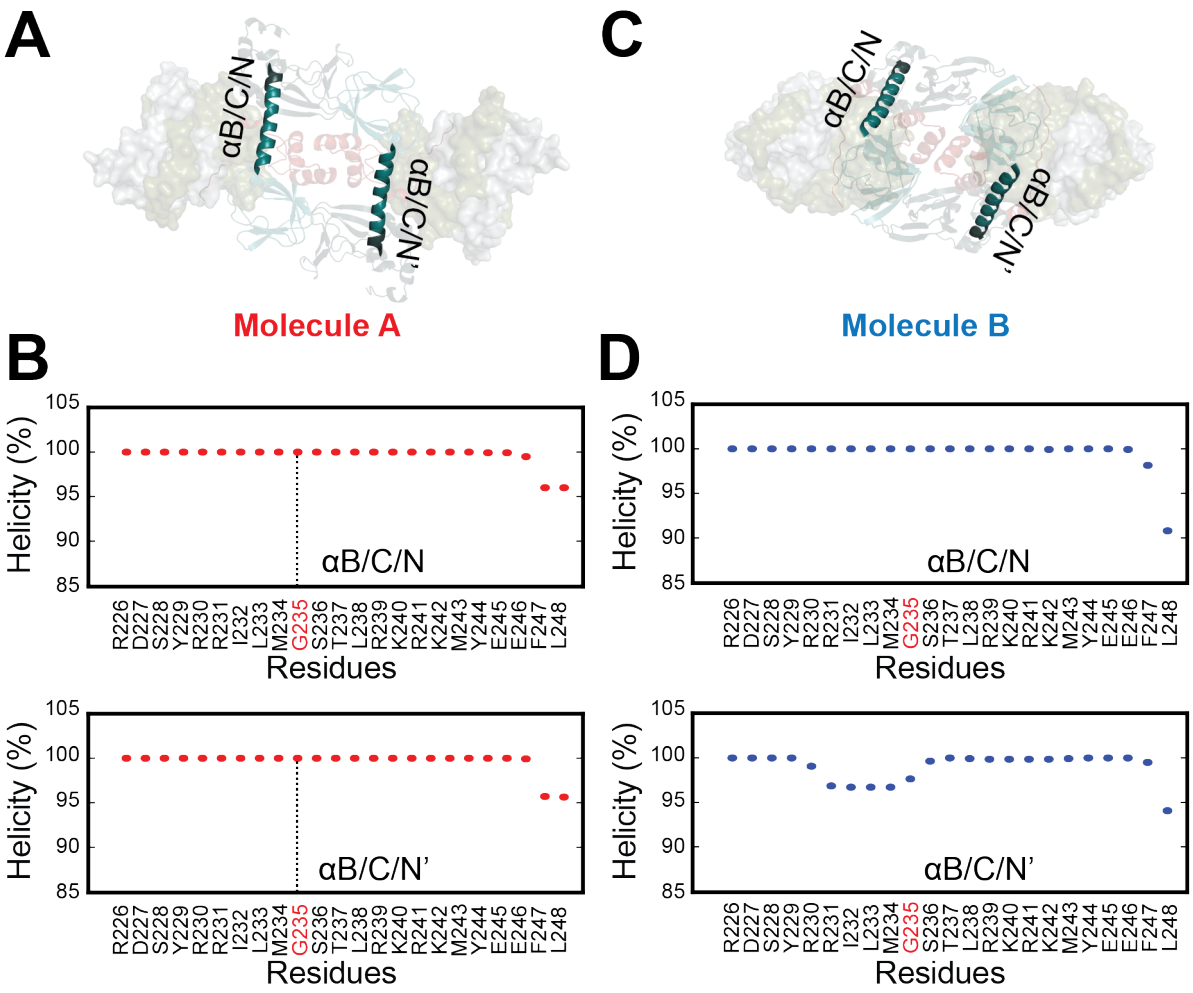

Figure 2-9. Two RIα holoenzyme conformations have distinct αB/C/N-helix dynamics. (A) αB/C/N-helix in Molecule A. (B) Helicity of αB/C/N-helix in Molecule A. (C) αB/C/N-helix in Molecule B. (D) Helicity of αB/C/N-helix in Molecule B. One of the protomer reveals lower helicity.

The holoenzyme interface in Molecule B not only shows a lower proportion of helicity of the αB/C/N-helix, but also contributes to the CNB domain dynamics. To examine the dynamic of features of the CNB domains, differences in the inter-chain CNB domain positions were represented by measuring the distance from the α-carbon of $Arg209^{RI\alpha}$ to the neighboring $Arg333^{RI\alpha'}$ in the other protomer ($R209^{RI\alpha}$ -$R333^{RI\alpha'}$/ $R333^{RI\alpha}$ -$R209^{RI\alpha'}$). Residues $Arg209^{RI\alpha}$ and $Arg333^{RI\alpha}$ have been identified as crucial amino acids for cAMP binding, and we use them here to represent the core of the CNB-A and CNB-B domains, respectively(15). In Molecule A, the distance between the two domains remains stable throughout the simulation with an S.D. = 3.22 and 2.43Å (Figure 2-10A and B). The distance fluctuation in Molecule B (S.D. = 4.61 and 3.97Å) is larger than in Molecule A, indicating the positions of CNB domains are more dynamic in Molecule B (Figure 2-10C and D). Taken together, the conformation specific dynamic and biochemical properties support the conclusion that Molecule A is in a fully inhibited more 'locked-state', while Molecule B can be considered to be an intermediate structure that can be activated more readily by cAMP.

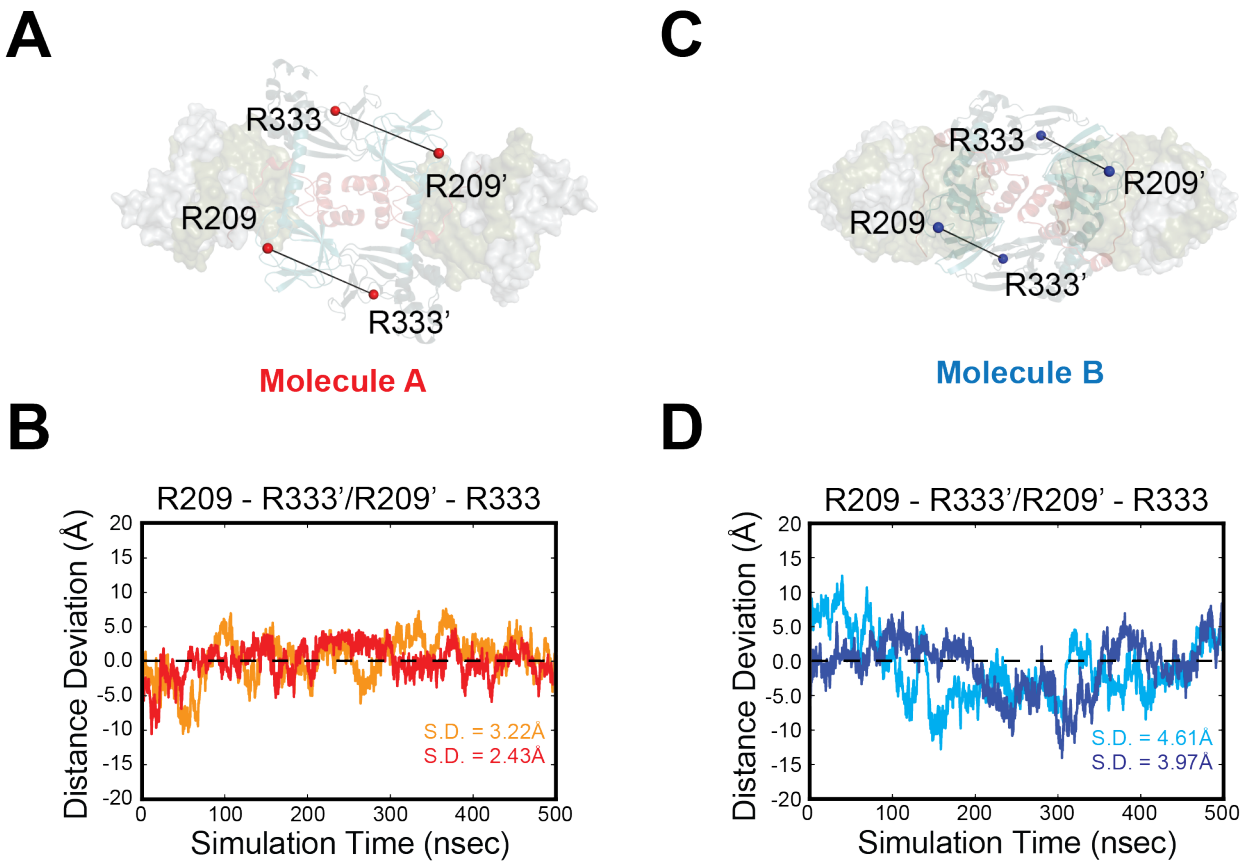

Figure 2-10. Molecule A and B have distinct R-subunit dynamics. (A) The distance between R209-R333' remain stable in Molecule A. (B) In Molecule B, the distance between R209-R333' changes dramatically.

2.6 Gly235 in RIα serves as pivot point for PKA activation

A main feature that distinguishes cAMP bound R-subunits (B-form) from the holoenzyme (H-form) is the αB/C/N-helix. In the holoenzyme, the αB- and αC-helices from CNB-A form a long contiguous helix with the αN-helix from CNB-B whereas in the cAMP-bound B-form, the αB/C/N-helix is split into three separated segments. $Gly235^{RI\alpha}$ lies at the junction between the αB- and αC-helix and serves as the pivot point for the transition from the B- to H-Form (17, 62). The strong helix propensity of the region corresponding to the αC/N-helix is also a unique feature of RIα. To study the effect of the contiguous αB/C/N-helix, $Gly235^{RI\alpha}$ was mutated to Ala/Leu/Pro. While the effects of the Leu and Ala mutations were negligible, the inhibitory effect of RIα was abolished by introducing the helix-disrupting proline mutation ($Gly235^{RI\alpha}$Pro) (Figure 2-11A and B). Even though this mutant can still form complex with C-subunit, it presumably cannot form a contiguous helix and catalytic activity is no longer inhibited (Figure 2-11C and D). These results suggest that an extended αB/C/N-helix is critical for inhibition of the catalytic activity. Once the extended αB/C/N-helix is disrupted, holoenzyme is much easier to activate while the inhibitory potential is reduced.

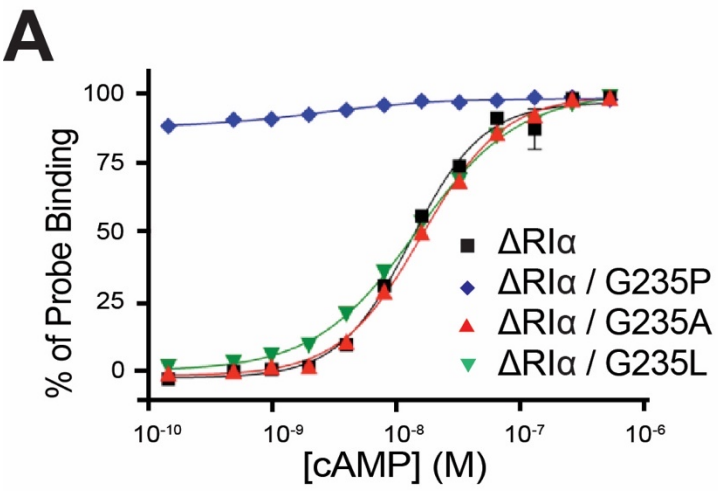

B

	EC50 (nM)	Hill Slope
WT	13.1 ± 0.9	1.50 ± 0.13
G235A	16.1 ± 0.5	1.32 ± 0.05
G235L	14.6 ± 1.4	1.07 ± 0.04
G235P	2.51± 0.93	0.90 ± 0.22

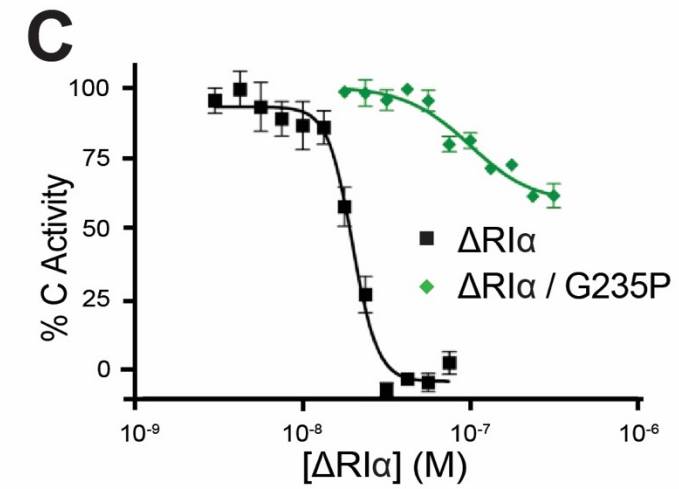

D

	EC50 (nM)	Hill Slope
WT	19.9 ± 0.8	-5.81 ± 1.13
G235P	99.2 ± 16.2	-2.28 ± 0.84

Figure 2-11. G235 is important for PKA RIα holoenzyme activation. (A) & (B) cAMP activation. (1-91Δ)RIα (Black square), (1-91Δ)RIα G235P (blue diamond), (1-91Δ)RIα G235A (red triangle), (1-91Δ)RIα G235L (green inverted triangle) (C) & (D) Kinase activity inhibition. (1-91Δ)RIα (Black square), (1-91Δ)RIα G235P (green diamond).

2.6.1 The N3A-N3A' motif nucleates the R:C/R':C' interface in Molecule A

Molecule A features an N3A-N3A' interface similar to what was described earlier in the RIα homodimer(17), and this was also seen in a recent holoenzyme structure with a cancer driving fusion protein of the C-subunit(63). Hydrophobic and hydrogen bonding interactions both contribute to the N3A-N3A' interface. The N3A-motif in each RIα protomer makes symmetric contacts with the N3A-motif in the other protomer, forming a compact 4-helix bundle. In Molecule A, the anti-parallel alignment of Met132^{RIα}, Tyr120^{RIα}, and Phe148^{RIα} on each protomer creates a hydrophobic core, while the interactions of Lys121^{RIα} to Asn142$^{RIα'}$, and Ser145^{RIα} to the main chain of Tyr120$^{RIα'}$ form the hydrogen bond network that holds the two N3A motifs together (Figure 2-12A). A smaller interface that may also contribute to allosteric crosstalk in Molecule A lies outside of the N3A-N3A' interface: Glu179^{RIα} in CNB-A forms hydrogen bonds with Arg315^{RIα} and Arg340^{RIα} in CNB-B' from the other protomer (Figure 2-12A).

2.6.2 Molecule B shows an αN-αN' interface

Molecule B has a distinct αN-αN' interface. Compared to Molecule A, the interactions are solely between αN- and αN'-helix (Figure 2-12B); the αA-helix is not involved. In Molecule B, Lys121^{RIα} forms a hydrogen bond with Thr122' on the other protomer. Moreover, the pairwise Tyr120^{RIα} /Tyr120$^{RIα'}$ hydrophobic interaction is broken and instead forms a smaller hydrophobic core together with Ala124^{RIα}, and Ala125^{RIα} between the αN-αN' interface. Lys128^{RIα} and Lys121^{RIα} form hydrogen bonds with Tyr120^{RIα} and Thr122^{RIα}/Tyr176^{RIα} on the other protomer, respectively.

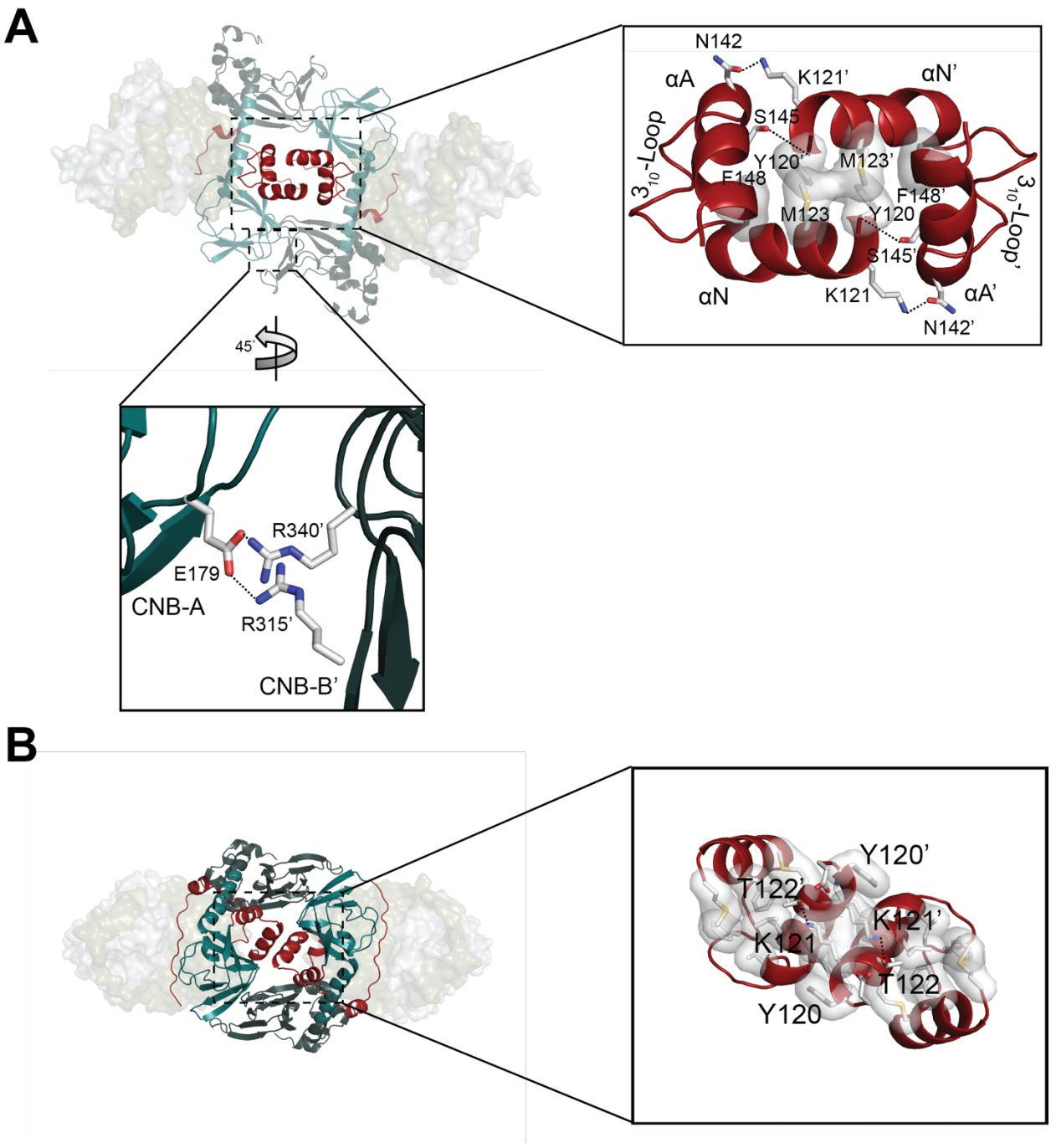

Figure 2-12. Holoenzyme interface of in two conformations of (A) Molecule A has N3A-N3A' interface. (B) Molecule B has αN-αN' interface.

2.7 N3A motifs are isoform-specific.

2.7.1 Sequence differences.

Although all four R-subunit isoforms share the same domain organizations, their quaternary structures are distinct(22), and sequence alignment show that the critical residues for forming the N3A-N3A' interfaces are RI specific (Figure 2-13A and B). The sequence of the N3A-motif in RI was analyzed across more than 130 different species, and residues involved in the N3A-N3A' interface, such as $Tyr120^{RI\alpha}$, $Met132^{RI\alpha}$, and $Phe148^{RI\alpha}$ for hydrophobic interactions and $Lys121^{RI\alpha}$, $Asn142^{RI\alpha}$, and $Ser145^{RI\alpha}$ for the hydrogen bonding network, are conserved across nearly all species (Figure 2-13A). Interestingly, from our sampling the conserved sequences in the N3A-motif of RI are only convergent in coelomates (Figure 2-13A). Other species, such as *C. elegans* and *S. cerevisiae*, do not have a conserved sequence in the αN- or αA-helix, but they can be phosphorylated on their inhibitor site (P-site). Based on our sequence analysis and the structure they are more RI-like; thus they appear to be somewhat of a hybrid (64). Since N3A-N3A' is the main interface in RIα, it is possible that higher species require a more complex system for allosteric regulation. The N3A-motif in RII-subunits also share similar sequences across most of the species, but they are different from RI-subunits and they lack the residues necessary for forming the N3A-N3A' interface (Figure 2-13B). This can explain why the RIIβ holoenzyme has a different quaternary structure where the N3A-motifs are solvent exposed(22), potentially providing a docking site for an as yet unknown protein partner. The highly conserved N3A motif sequences within but not between type I and type II R-subunits demonstrates another isoform-specific feature of the PKA holoenzyme structures.

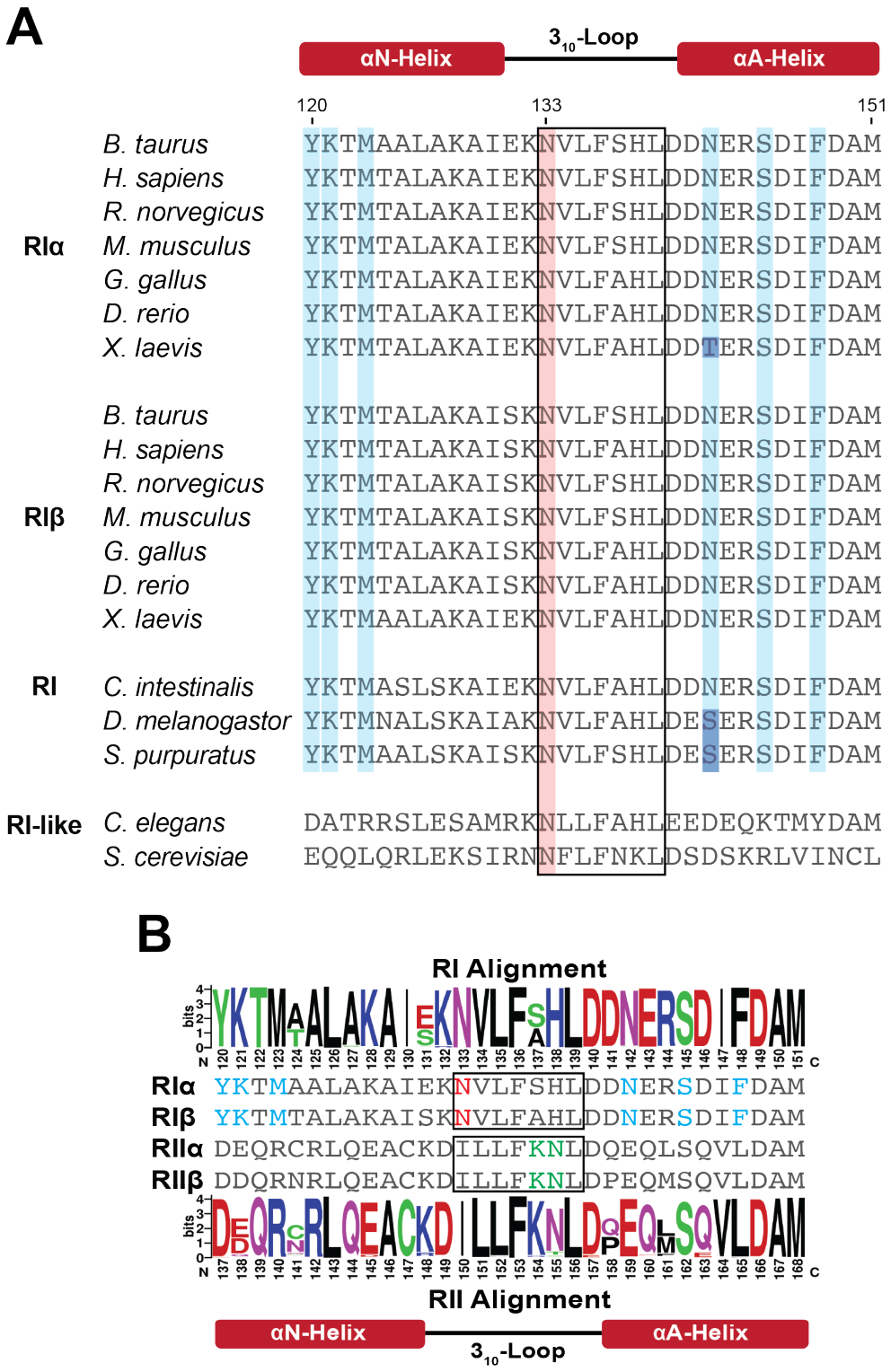

Figure 2-13. The N3A motif is highly conserved in different species. (A) The N3A motif in RI is highly conserved. (B) RI and RII have distinct conserved N3A motifs.

2.7.2 3_{10}-loop.

In addition to residues in the αN- and αA-helices, the sequences in the 3_{10}-loop that connects the αA-helix to the αN-helix is also highly conserved across species. However, this loop that also contributes to the R-C interface is different in RI and RII. In the RIα holoenzyme, the hydrophobic residues in the 3_{10}-loop, Val134^{RIα}, Leu135^{RIα}, Phe136^{RIα}, and His138^{RIα}, interact with other hydrophobic residues from the αB/C/N-helix in CNB-A and the αG-helix in the C-subunit forming a ternary motif interface (Figure 2-14A)(18). Even though hydrophobic interactions can also be observed in the RIIβ holoenzyme (Figure 2-14B), Lys154^{RIIβ} and Asn155^{RIIβ} in the 3_{10}-loop of RIIβ form water-mediated hydrogen bonds between the ternary motif interface. This solvent accessible interface would be weaker than the strongly hydrophobic interactions that dominate the RIα holoenzyme.

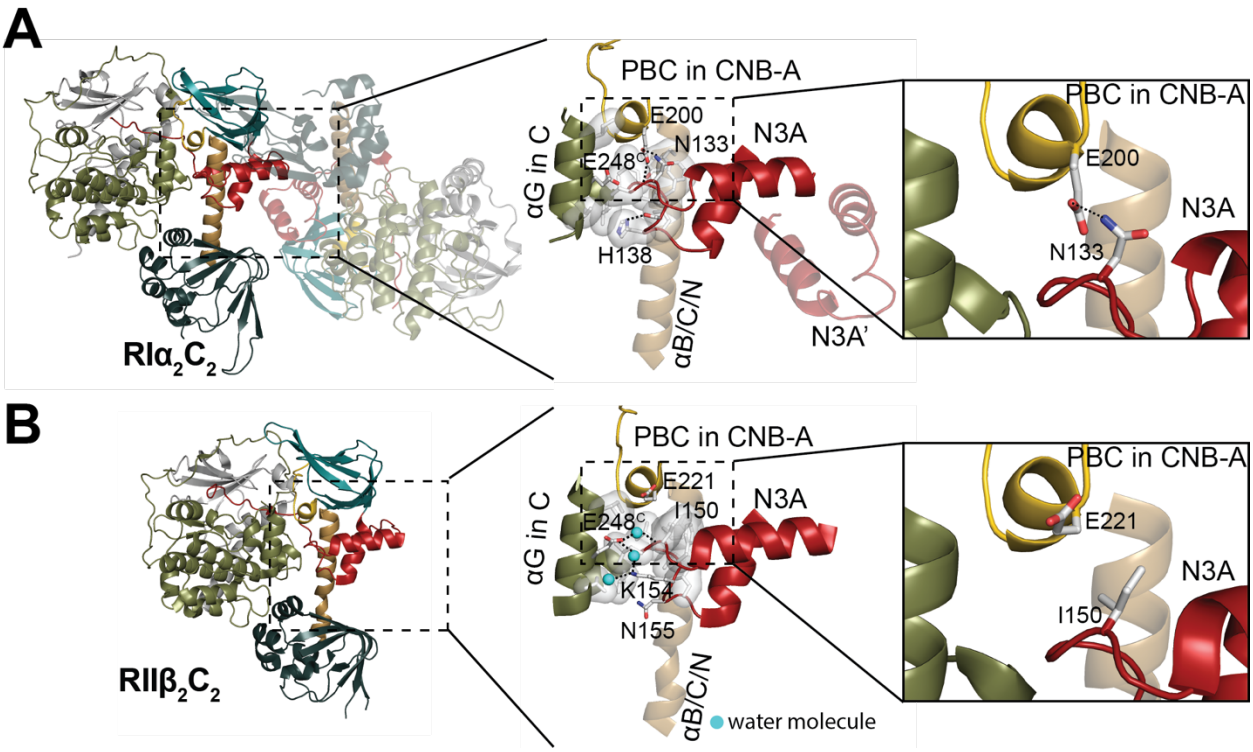

Figure 2-14. Isoform specific R-C interface. (A) E200 forms hydrogen bond with N133 in RIα. (B) E221 is solvent exposed in RIIβ.

2.8 Role of Glu200

In the RIα holoenzyme, Asn133^{RIα} in the αN-helix forms a hydrogen bond with Glu200^{RIα} in the PBC of CNB-A (Figure 2-14A). Glu200^{RIα} is essential for cAMP binding (62, 65) and is conserved in all PKA R-subunits while Asn133^{RIα} is only conserved in RI-subunits. The same hydrogen bond is found in both the RIβ holoenzyme and (Δ1-91)RIα:C structures; however, there is no hydrogen bond between the PBC of CNB-A and the 3_{10}-loop in RII. The equivalent positions of Asn133^{RIα} and Glu200^{RIα} in RIIβ are Ile150^{RIIβ} and Glu221^{RIIβ}, respectively. While Glu221^{RIIβ} is still important for binding to cAMP, it cannot hydrogen bond to Ile150^{RIIβ}, and instead is solvent exposed in the holoenzyme (Figure 2-14B); there is no direct link between the 3_{10}-loop and the PBC. Ile150^{RIIβ}, Glu221^{RIIβ}, Lys154^{RIIβ}, and Asn155^{RIIβ} are conserved in all RII- subunits. Glu221^{RIIβ} is also solvent exposed in the (Δ1-89)RIIα:C structure. The sequence differences between isoforms thus not only explain the distinct quaternary structures, but also highlight different allosteric crosstalk mechanisms between the N3A-motif, the C-subunit, and the CNB-A/CNB-B domains.

2.9 N3A-N3A' is a central hub for allosteric regulation of the RI holoenzyme

The N3A-N3A' interface forms a crosstalk network and serves as a central hub for mediating allosteric communication in both the RIα holoenzyme and RIα dimer. The N3A-motif interacts with several other motifs and links all them together. The residues on the αN-helix and αA-helix are essential to form the N3A-N3A' interface and bring the two protomers together. The 3_{10}-loop is also the crucial motif for interacting with both the αB/C/N-helix and the C-subunit(16).

Finally and perhaps the most importantly, in RIα the 3_{10}-loop also anchors directly to the PBC in the CNB-A domain and thus is a sensor for cAMP binding (Figure 2-15A). Our structures reveal that the other protomer can also be influenced through interactions of the N3A-N3A' motifs. The multi-domain crosstalk network nucleated by the N3A-N3A' interface is thus a central hub that provides a mechanistic model for the tightly regulated PKA RIα holoenzyme system.

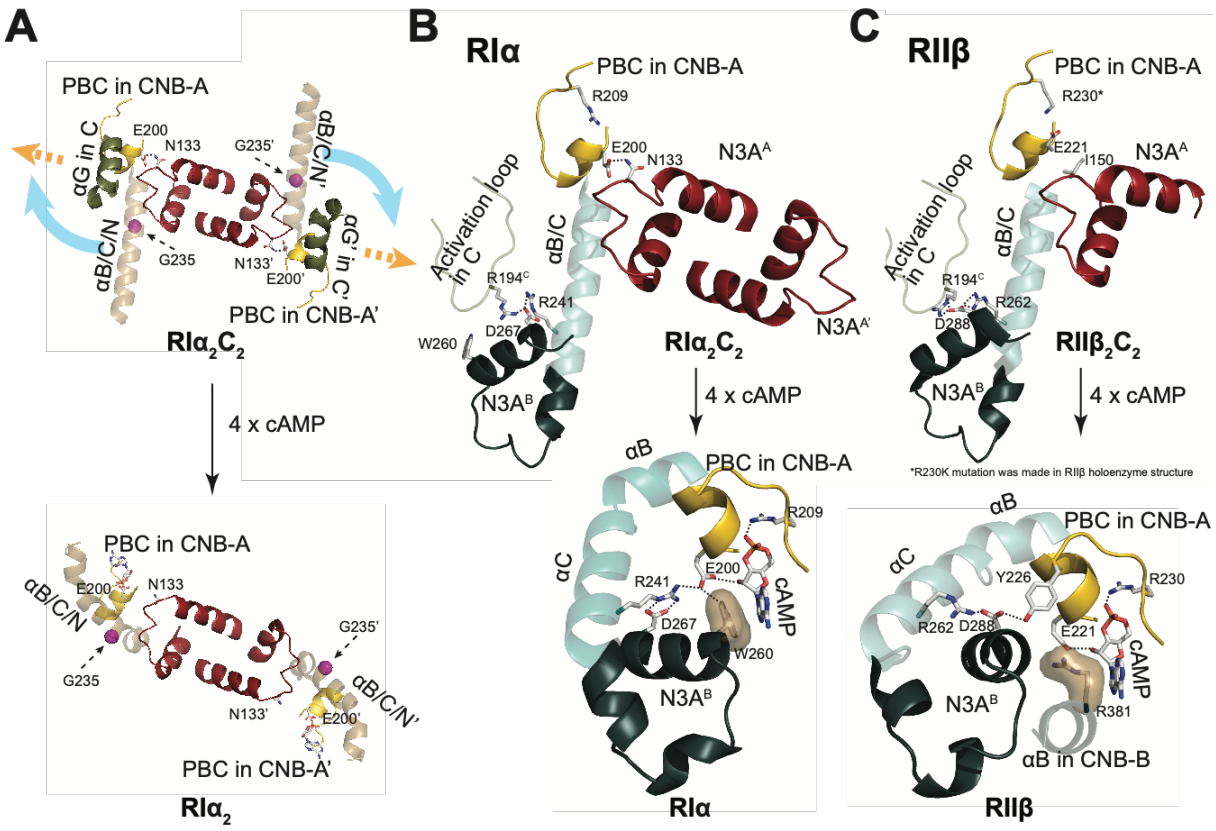

Figure 2-15. N3A-N3A' motif serves as central hub. (A) N3A-N3A' motif severs as central hub for cAMP activation. (B) N3A-N3A' motif primes the allosteric regulation in RIα. (C) RIIβ has distinct allosteric network.

2.10 Discussion

Our crystal structures of the RIα holoenzyme in the presence and absence of ATP reveal an ATP-dependent allosteric mechanism that is isoform specific. The role of ATP as an orthosteric inhibitor that controls the conformation of the RIα holoenzyme is supported by biochemical and SAXS data. ATP is an essential cofactor for all kinases serving as a substrate that donates its γ-phosphate either to water or to a protein substrate. However, because both RIα and PKI are pseudo-substrates, ATP plays a different role; it is an orthosteric inhibitor. While pseudo-kinases have been highlighted recently, less attention has been devoted to pseudo-substrates. In the RIα holoenzyme there is a competition between two nucleotides, cAMP and ATP, that allosterically controls the activity of the C-subunits that are tethered to the RIα dimer.

Our holoenzyme structures also highlight the unique importance of the N3A-mediated dimer motif in CNB-A. The four helix bundle created by the N3A-N3A' node nucleates a major interface between the two R:C heterodimers, and this serves as a finely-regulated central hub not only for the RIα dimer but also for the RIα holoenzyme(17). While RIα interacts with the C-subunit to form a high affinity RIα:C complex, this RIα:C complex does not allow us to appreciate the full extent of allosteric activation that is embedded in the tetrameric holoenzyme. The N3A-N3A' interaction introduces a direct R:C/R':C' pathway that allows the CNB-A domain to communicate not only with its own CNB-B domain, but also directly with the CNB-B' domain. This helps to explain why the full allosteric potential for cAMP-mediated activation with a high cooperativity (Hill coefficient 1.3-1.5) is achieved only in the holoenzyme, but not in the R:C heterodimer where the Hill coefficient is only around 1.1(13). Our further dissection of this allosteric node also shows how $Glu200^{RI\alpha}$, a residue that is essential for binding to cAMP in the

PBC, also contributes directly to the N3A-N3A' crosstalk in RIα but not in RIIβ, and this is another key difference between the two holoenzymes. The allosteric implications of this node are discussed below and then the differences between the RIα and RIIβ holoenzymes.

2.10.1 N3A-motifs

The idea that N3A-N3A' serves as central hub and can pass activation signals to different domains now reveals new levels of domain crosstalk in the RIα holoenzyme. This crosstalk network of four CNB domains underlines how finely regulated the RIα system is, and helps to explain the high cAMP activation cooperativity of RIα. Two interacting residues, $Arg241^{RI}$ and $Asp267^{RI,}$ have been shown previously to be important for allosteric activation of PKA. $Arg241^{RI\alpha}$ in the αB-helix in CNB-A interacts directly with $Asp267^{RI\alpha}$ at the end of the αA^{B}-helix in CNB-B (Figure 2-15B)(66), and this node ($Arg241^{RI\alpha}$ -$Asp267^{RI\alpha}$) that links CNB-A to CNB-B is universally conserved in all holoenzymes and in all cAMP bound conformations (Figure 2-15B and C). The exception is the ACRDYS mutant of RIα holoenzyme, where residues 366-379 are deleted, in the case $Asp267^{RI\alpha}$ is ordered differently(66). The two key residues for binding to cAMP in the PBC are $Arg209^{RI\alpha}$ and $Glu200^{RI\alpha}$ in CNB-A, and these are also conserved in all of the CNB domains. Each bound cAMP also has a hydrophobic capping residue, and this is not only different for CNB-A and CNB-B but is also different in RI- and RII-subunits(67). For cAMP bound to the RIα CNB-A, the capping residue is $Trp260^{RI\alpha}$, which also lies in the αA^{B}-Helix. Another residue in the αA^{B}-Helix is $Glu261^{RI\alpha}$, which is anchored to $Arg366^{RI\alpha}$ in the αC-Helix of CNB-B in the holoenzyme. These electrostatic interactions are conserved in all PKA holoenzymes and in the R:C complexes (Figure 2-15B and C). If we now consider the N3A-N3A' node, we see an additional interaction that is RIα specific. $Asn133^{RI\alpha}$ in the 3_{10}-loop of the N3A

motif in RIα interacts with Glu200$^{RI\alpha}$ in the PBC of CNB-A', and this link is missing in the RIIβ holoenzyme where both Arg230$^{RII\beta}$ and Glu221$^{RII\beta}$ are solvent exposed (Figure 2-15C). Each N3A motif in RIα is thus linked directly to its own PBC as well as to the N3A' motif. What are the consequences for allosteric activation and how do the CNC disease mutations emphasize the importance of these contacts?

2.10.2 Allosteric regulation

Although Glu200$^{RI\alpha}$/Glu221$^{RII\beta}$ both contribute directly to cAMP binding in CNB-A, they play different allosteric roles in the cAMP-bound B-Form in RIα and RIIβ (Figure 2-15B and C). In RIα, Glu200$^{RI\alpha}$ nucleates an extended allosteric node that involves Arg241$^{RI\alpha}$, Asp267$^{RI\alpha}$, and cAMP, and this node is stabilized by the capping residue Trp260$^{RI\alpha}$. In the B-form of RIIβ, Glu221$^{RII\beta}$ interacts only with cAMP, while the capping residue (Arg262$^{RII\beta}$), which in this case is in the αB-helix of CNB-B and still anchored to Asp288$^{RII\beta}$, now interacts with Tyr226$^{RII\beta}$ in the PBC of CNB-A. This shows how specific residues can multi-task and also highlights how a few amino acids can completely change allosteric signaling and domain interactions.

2.10.3 Disease mutations

Disease mutations associated with CNC (Arg144$^{RI\alpha}$Ser and Ser145$^{RI\alpha}$Gly) as well as critical residues in the N3A-N3A' interface (Lys121$^{RI\alpha}$Ala and Tyr120$^{RI\alpha}$Ala) further highlight the physiological and allosteric importance of this node, which is unique to RI holoenzymes. Tyr120$^{RI\alpha}$ and Lys121$^{RI\alpha}$ anchor the N-terminus of the αN-helix to the C-terminus of the αA'-helix, and mutation of either residues almost completely abolishes all cooperativity (Hill Coefficient = 1-1.1 vs 1.75 in wild-type)(17). CNC mutations in the αA-helix (Arg144$^{RI\alpha}$Ser and Ser145$^{RI\alpha}$Gly) that flank the hydrophobic interface between αA- and αA'-helix reduce the Hill

Coefficient to 1.45. These will likely weaken the hydrophobic interface while mutation of Lys121$^{RI\alpha}$ will break the dimer. Based on SAXS, these mutations also effect the shape of the RIα dimers; both types of mutation create a more extended conformation that resembles the RII dimer(17). Tyr120$^{RI\alpha}$Ala, which abolishes cooperativity, is the most extended while the Ser145$^{RI\alpha}$Gly dimer is intermediate. We predict that these mutations will also likely influence the compact vs. extended conformation of the RIα holoenzyme as they do for the RIα dimer.

2.10.4 Holoenzyme allostery

Our holoenzymes show how an additional level of crosstalk can occur through CNB-B and CNB-A', and this is highly significant because previous studies established that the first cAMP that binds to the RIα holoenzyme binds to the CNB-B domain(15, 19). With our structure we can see how binding to the CNB-B domain will not only communicate a signal to its own CNB-A domain through the αB/C/N-helix, but will also give an immediate signal to the opposite CNB-A' domain. Our structure of the apo holoenzyme shows furthermore how the removal of ATP dramatically changes the dynamic portrait of the holoenzyme poising it for activation/dissociation. Weakening of the specific CNB-B:CNB-A' interface will likely be the first step in the signaling process following binding of cAMP to CNB-B which will essentially release Glu200$^{RI\alpha}$ from the N3A-N3A' interface. Can this lead to activation of the C'-subunit, or at least release of the inhibitor site that blocks substrate binding to the C'-subunit, by a mechanism that will not require dissociation of the holoenzyme? This is a future challenge. If the holoenzyme is tethered in close proximity to the tail of a receptor or channel or transporter that contains the site of PKA phosphorylation then all that would be required is that the peptide harboring the phosphorylation site has access to the active site cleft of one C-subunit. While the first step following cAMP binding would be transmitted to CNB-A', subsequent steps leading to the actual dissociation of the R- and

C-subunits would involve signaling to the αB/C/N-helix which would need to bend. The extended αB/C/N-helix is well protected in this holoenzyme complex. This model for communication between CNB-B and CNB-A' would also provide an explanation for why the point mutations associated with ACRDYS and CNC diseases are dominant. It also suggests that there is an inherent asymmetry in the signaling process.

2.10.5 Isoform-specific allostery

The RIα and RIIβ holoenzymes have distinct quaternary structures (Figure 2-16A and B). In both of our RIα holoenzymes and the RIα dimer, the interacting N3A-N3A' motifs are the dominant feature of the protein interface (Figure 2-16A and C). In contrast, in RIIβ holoenzymes, the N3A domains are exposed to solvent and do not contribute to the major interface between RC and R'C' (Figure 2-16B and D). Instead in the RIIβ holoenzyme structure, the major holoenzyme interface is based on the interaction of the β4-β5 loop in the CNB-A domain of RIIβ with the adjacent C'-subunit(22).

The two RIα holoenzyme structures allow us to appreciate not only how cAMP controls PKA activation, but also how ATP serves as an allosteric co-factor, and this is in striking contrast to the RIIβ holoenzyme. Even though all PKA R-subunit isoforms share the same domain organization, the role that is played by ATP is fundamentally different (Figure 2-16E). In the RIα holoenzyme, ATP induces a more extended conformation and enhances the affinity of the R- and C-subunits (<0.05 nM in the presence of ATP, and 125 nM in the absence of ATP)(13). In addition, the ATP-bound conformation (Molecule A) is more stable and more resistant to activation by cAMP. These two nucleotides, ATP and cAMP, thus are competing in the RIα holoenzyme. ATP serves as an orthosteric inhibitor that blocks access of the protein substrate to the active site, while cAMP docking to the CNB domains of the R-subunit facilitates activation by releasing the

inhibitory sequence (Figure 2-16A). In the RIIβ holoenzyme, ATP has a different role. The dimensions of the RIIβ holoenzyme are the same in the presence and absence of ATP, and ATP is not required to form a stable complex(22). For the RIIβ holoenzyme, ATP is a substrate that controls the phosphorylation state of the inhibitor site and enhances opening and closing of the active site cleft by a single-turn-over mechanism (Figure 2-16B). When the RIIβ holoenzyme is phosphorylated, it is easier for cAMP to release the inhibitor sequence from the active site cleft of the C-subunit(24). Since RIα and RIIβ localize differently and ATP concentrations vary in different cellular compartments, it is likely that the two holoenzymes have very distinct ATP-dependent roles(14). The sensitivity of the RIα holoenzyme to ATP is especially relevant for localization to mitochondria where RIα-related signaling would be triggered by depressing the levels of ATP and/or Mg^{2+}. Elevating ATP levels could turn on RIIβ-related signaling pathways, while RIα-related signaling would be triggered by depressing the levels of ATP. This also highlights the potential importance of the RIα holoenzyme as a stress responsive holoenzyme; it is not required when energy levels are high. The ATP-dependent holoenzyme activation allows the PKA holoenzyme to serve as an energy sensor, which is consistent with recent studies showing that PKA can be activated more by metabolic stress such as glucose deprivation than by cAMP stimulation; lowering the energy levels may be sufficient to influence PKA activation(68). Since the second Mg^{2+} ion is essential for the high affinity ATP binding to the RIα holoenzyme, we hypothesize that this holoenzyme can be also tightly regulated by metal homeostasis in cells(69, 70).

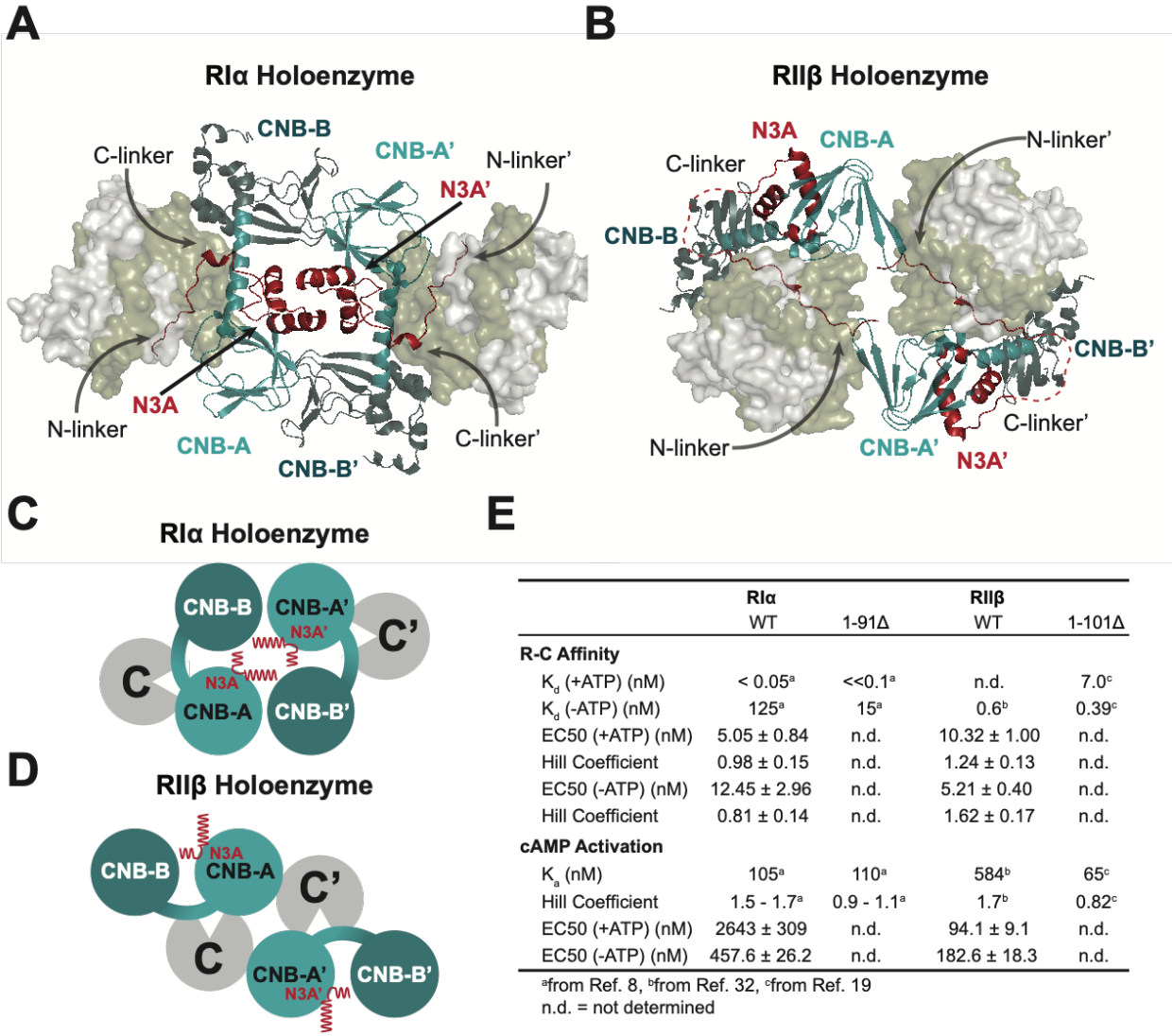

E

	RIα		RIIβ	
	WT	1-91Δ	WT	1-101Δ
R-C Affinity				
K_d (+ATP) (nM)	< 0.05[a]	<<0.1[a]	n.d.	7.0[c]
K_d (-ATP) (nM)	125[a]	15[a]	0.6[b]	0.39[c]
EC50 (+ATP) (nM)	5.05 ± 0.84	n.d.	10.32 ± 1.00	n.d.
Hill Coefficient	0.98 ± 0.15	n.d.	1.24 ± 0.13	n.d.
EC50 (-ATP) (nM)	12.45 ± 2.96	n.d.	5.21 ± 0.40	n.d.
Hill Coefficient	0.81 ± 0.14	n.d.	1.62 ± 0.17	n.d.
cAMP Activation				
K_a (nM)	105[a]	110[a]	584[b]	65[c]
Hill Coefficient	1.5 - 1.7[a]	0.9 - 1.1[a]	1.7[b]	0.82[c]
EC50 (+ATP) (nM)	2643 ± 309	n.d.	94.1 ± 9.1	n.d.
EC50 (-ATP) (nM)	457.6 ± 26.2	n.d.	182.6 ± 18.3	n.d.

[a]from Ref. 8, [b]from Ref. 32, [c]from Ref. 19
n.d. = not determined

Figure 2-16. Isoform specific quaternary structure and allostery. (A) & (C) RIα holoenzyme. (B) & (D) RIIβ holoenzyme. (E) R-C affinity and cAMP activation of RIα and RIIβ holoenzyme in the presence and absence of ATP.

2.10.6 Summary

In summary, our structures together with biochemistry and simulations provide new insights into the biological function and complex regulation of the RIα holoenzyme. We show how ATP, by serving as a high affinity orthosteric inhibitor, plays a crucial role in influencing not only the RIα holoenzyme conformation but also its biological properties. We have also captured the crosstalk between the CNB and CNB' domains and show how the N3A-N3A' interface in CNB-A serves as a central hub for allosteric regulation, in contrast to the RIIβ holoenzyme, where these N3A motifs are solvent exposed (Figure 2-16A-D). Our results together with previous studies further confirm that the allosteric regulation of the RIα and RIIβ holoenzymes are quite distinct (Figure 2-16E). In addition to localization, we can see that isoform diversity of the PKA holoenzymes extends to function, allostery, and quaternary structure. We can also now better appreciate how isoform diversity is controlled in mechanistically distinct ways by ATP. Our enhanced allosteric portrait of the RIα holoenzyme also lays the foundation for further tackling the pathogenic mechanisms that underlie diseases such as CNC and ACRDYS which highlight the unique importance of the RIα holoenzyme as a general sensor for stress.

2.11 Acknowledgment

Chapter 2 includes the material that appears appears in Lu, T.-W.; Wu, J.; Aoto, P. C.; Weng, J.-H.; Ahuja, L. G.; Sun, N.; Cheng, C. Y.; Zhang, P.; Taylor, S. S. "Two PKA RIα holoenzyme states define ATP as an isoform-specific orthosteric inhibitor that competes with the allosteric activator, cAMP" *Proc National Acad Sci* **2019**, *116*, 16347-16356. The dissertation author is the primary author of this manuscript.

Chapter 3 The RIα holoenzyme with DnaJB1-PKAc

To understand the pathological consequences of FL-HCC, we focused on the RIα and RIIβ holoenzyme formed with J-C and solved its structure at near atomic level resolution using X-ray crystallography and cryoEM single particle reconstruction respectively in the following two chapters. Our studies of the DnaJB1-PKAc RIα holoenzyme ($RI\alpha_2J\text{-}C_2$) (Chapter 3) and RIIβ holoenzyme ($RII\beta_2J\text{-}C_2$) (Chapter 4) structures and functions provide us with a better understanding of FL-HCC and shed light on new potential therapeutic strategies.

In this chapter, which is a summary of our published work(63), we show that J-C is inhibited by full-length RIα and capable of forming the canonical holoenzyme with activation still under the control of cAMP. In the structural studies of the $RI\alpha_2J\text{-}C_2$ holoenzyme, the fused J-domain is tucked underneath the C-lobe of the conserved kinase core (*16*). To explore whether the addition of the J-domain affects the conformational landscape of each RIα holoenzyme, we furthermore report on MD simulations of the chimeric and wt RIα holoenzymes. We found that the J-domain in $RI\alpha_2J\text{-}C_2$ holoenzyme was dynamic and flexible. Altogether, the structural and dynamic description of the driver of FL-HCC provides insights for understanding the molecular mechanism of this disease.

3.1 Effects of the J-domain attachment to C-subunit

To study the effect of J-domain fusion on the C-subunit, we first characterized the biochemical and biophysical properties of J-C-subunit alone and compared with the wt C-subunit.

First, to evaluate their thermostability we used a ThermoFluor assay to determine their protein melting temperature (Figure 3-1 and Table 3-1). The apo form of wt C-subunit reveals a higher melting temperature than the J-C-subunit, indicating that the C-subunit is thermally more stable. We also confirmed that the PKA substrates (ATP and/or PKI peptide) can stabilize the PKA C-subunit. After adding the PKA substrates, the melting temperature of the C-subunit increases, showing that the substrates can stabilize the C-subunit. The substrates also have similar effects on the J-C-subunit, where PKI and/or ATP can increase its thermostability; however, the fusion protein remains thermally less stable than the wt C-subunit after adding the PKA substrates. In general, the fusion protein is less stable than the wt C-subunit.

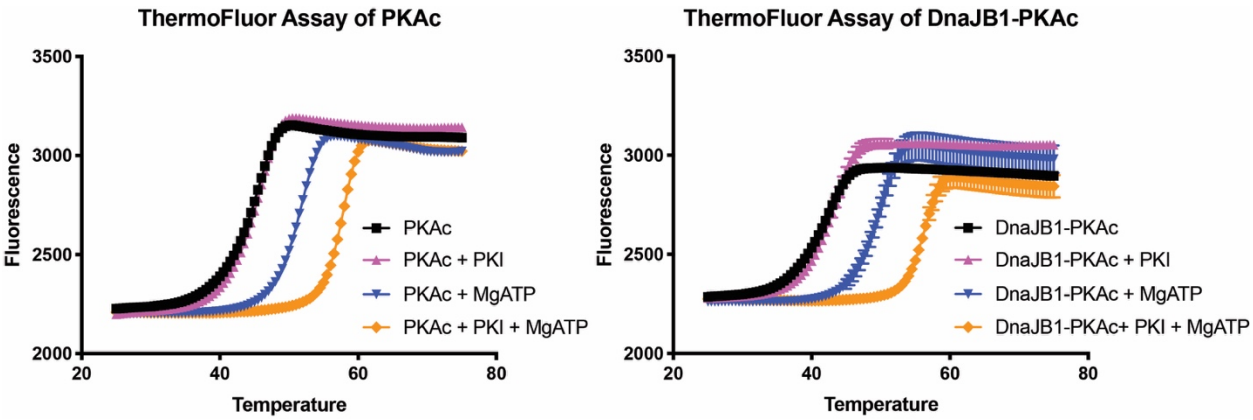

Figure 3-1. Melting temperature of C-subunit and J-C-subunit with peptides and ATP/Mg

Table 3-1. Melting temperature of PKA C-subunit and J-C-subunit.

Tm (°C)	Apo	+ PKI	+ MgATP	+ PKI/MgATP
PKAc	43.84 ± 0.07	44.46 ± 0.05	50.71 ± 0.06	57.16 ± 0.04
DnaJB1-PKAc	40.93 ± 0.06	42.43 ± 0.04	48.90 ± 0.09	55.76 ± 0.06
Δ Tm (WT/mutant)	2.91 ± 0.09	2.03 ± 0.06	1.81 ± 0.11	1.40 ± 0.07

Next, we examined the binding affinity of PKA kinase substrates. By using the ThermoFluor assay, we are able to measure the melting points of C- and J-C-subunits with different amounts of ATP which allows us to determine the binding ability for ATP (Figure 3-2A and Table 3-2). Both wt C- and J-C-subunit show similar dissociation constants for ATP. For peptide substrate binding, we used the PKI-derived peptide (residue 5-24), labeled with an N-terminal fluorophore as substrate. The fluorescence polarization increases once the proteins bind with the peptide forming a larger complex (Figure 3-2B and Table 3-2). Therefore, based on the fluorescence polarization changes, we can determine the dissociation constant (K_d). Both wt C- and J-C-subunit show similar dissociation constants (K_d) towards the PKI peptide. These results show that both C-subunit and J-C-subunit have similar binding ability toward ATP and peptide substrates. J-C-subunit displayed unaltered binding affinities for ATP and inhibitor peptide.

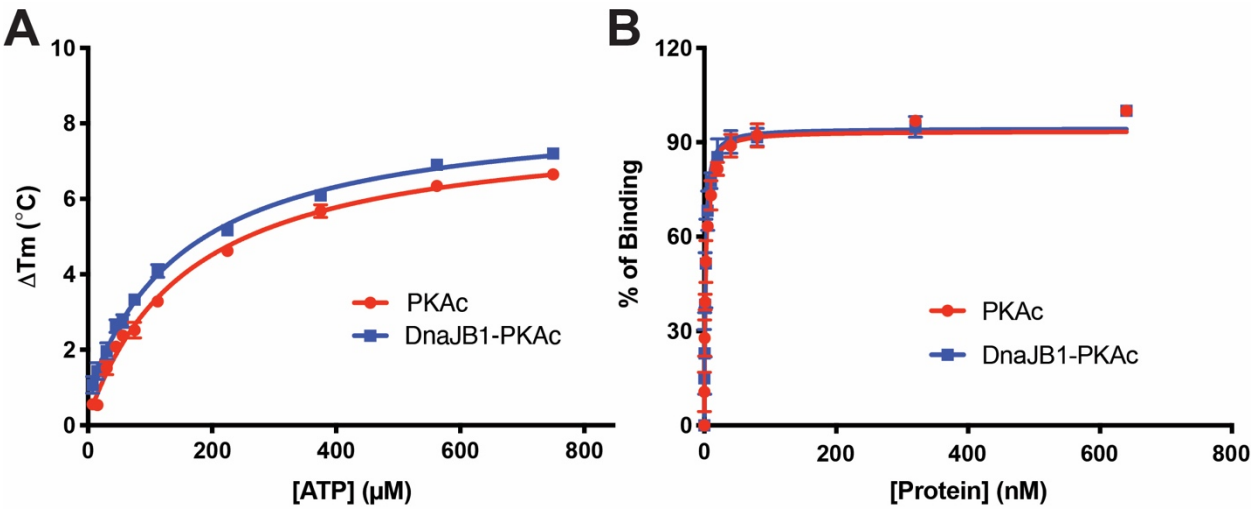

Figure 3-2. Substrate binding measurement of C- and J-C-subunits. (A) ATP binding. (B) PKI peptide binding.

Table 3-2. Dissociation constants of PKA C-subunit and J-C-subunit with ATP and PKI peptide.

K_d	ATP	PKI (5-24)
PKAc	159.8 ± 12.2 μM	1.75 ± 0.06 nM
DnaJB1-PKAc	152.5 ± 10.8 μM	1.63 ± 0.09 nM

To compare the activity difference of C- and J-C-subunit, we then further measured their Michaelis-Menten kinetics. The fusion protein reveals a higher k_{cat} than the wt C-subunit, whereas the wt C-subunit has a smaller K_m value for ATP than the J-C-subunit. These results are in agreement with previous reports (*16*), the chimeric protein was thus slightly more active than its wt counterpart with unchanged enzymatic efficiency as shown by k_{cat}/K_m values (Figure 3-3 and Table 3-3), suggesting that the J-domain may affect C-subunit enzyme kinetics.

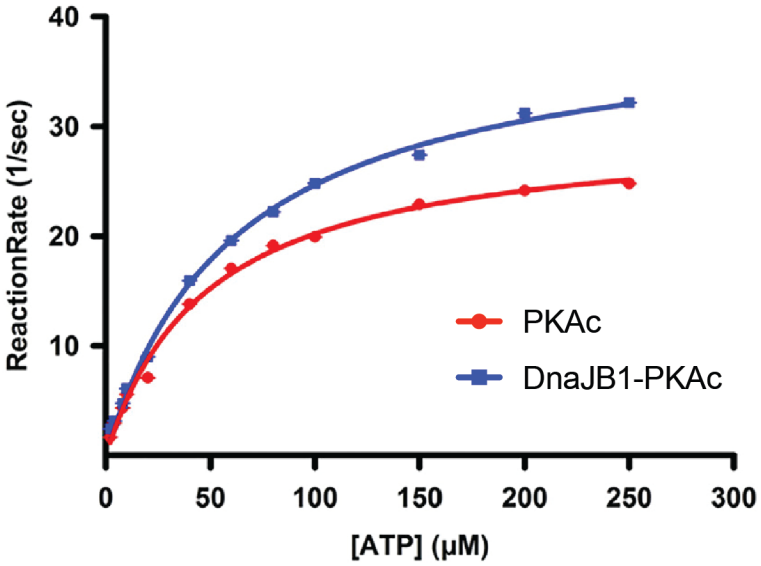

Figure 3-3. Michaelis-Menten Kinetics of C- and J-C-subunits.

Table 3-3. Michaelis-Menten Kinetics of C- and J-C-subunits.

	PKAc	DnaJB1-PKAc
k_{cat} (s^{-1})	27.5 ± 2.5	37.0 ± 3.0
K_m (μM)	51.1 ± 2.6	70.0 ± 8.0
k_{cat}/K_m ($s^{-1}\mu M^{-1}$)	0.54 ± 0.06	0.53 ± 0.07

3.2 Structure of the chimeric RIα$_2$J-C$_2$ holoenzyme

3.2.1 X-ray crystal structure

The complex of the full-length RIα and J-C-subunit was formed *in vitro* by mixing the individually purified subunits followed by gel filtration. The full-length holoenzyme structure was determined at 3.66Å resolution (Figure 3-4 and Table 3-4). The dimensions of RIα$_2$J-C$_2$ holoenzyme crystal structure are 143.7 × 87.7 × 73.8Å, similar as wt RIα$_2$C$_2$ holoenzyme. Each asymmetric unit contains one holoenzyme molecule consisting of an RIα homodimer and two chimeric J-C subunits, thus the chimeric holoenzyme has the same stoichiometry as the previously published wt holoenzymes (*17*). The interface between the two protomers in the chimeric holoenzyme, similar to wt RIα holoenzyme, contains a four-helical bundle forming an N3A-N3A' interface with a two-fold rotation axis in the central of holoenzyme (Figure 3-4). The two J-C subunits bind at opposite sides of the holoenzyme with the two RIα-subunits forming the dimer interface in the middle. Similar to the wt RIα crystal structure, residues 1-91 of RIα are missing in the electron density; however, SDS-PAGE and silver staining confirm that the full-length RIα and J-C are present in the protein crystal. The absence of electron density for the D/D domain and part of the following N-linker is likely related to the flexible nature of this region similar to what was observed for the wt holoenzyme (*30*).

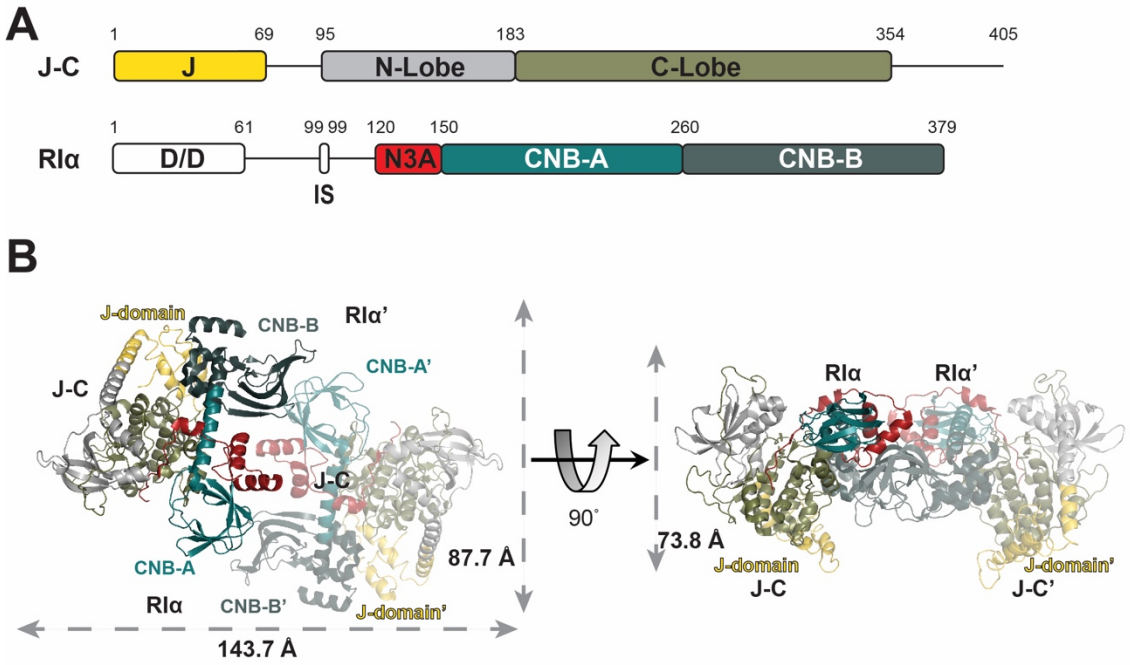

Figure 3-4. The RIα$_2$J-C$_2$ holoenzyme structure. (A) Domain diagram of RIα- and J-C-subunits. (B) Crystal structure.

Table 3-4. Crystallography data collection, refinement and validation statistics.

Structure: RIα$_2$J-C$_2$	
Data collection	
Space group	$P6_522$
Cell dimensions	
a, *b*, *c* (Å)	166.5, 166.5, 332.7
α, *β*, *γ* (°)	90, 90, 120
No. molecules per ASU	1
Resolution (Å)	50.0-3.66 (3.79-3.66)
R_{merge}	0.135 (0.50)
I/sigma	29.5 (8.7)
Completeness (%)	100.0 (100.0)
No. reflections	30,810
Refinement	
PDB code	6BYR
Resolution (Å)	50.0-3.66
R_{work}/R_{free} (%)	20.0/25.0
RMSD	
Bond lengths (Å)	0.003
Bond angles (°)	0.623
Ramachandra angles (%)	
Favored	93.0
Disallowed	0
Twin operator	N/A

3.2.2 Small Angle X-ray Scattering

The SAXS analyses reveal the structural and dynamic difference of RIα$_2$J-C$_2$ and RIα$_2$C$_2$ holoenzyme in solution. Based on pair-distance distribution functions *P(r)*, both holoenzymes have similar but different dimensions (Figure 3-5A, Figure 2-5B and Table 3-5). The RIα$_2$C$_2$ holoenzyme has slightly smaller R_g and D_{max} values (R_g = 52.08Å, D_{max} = 160Å) than the RIα$_2$J-C$_2$ holoenzyme (R_g = 52.59Å, D_{max} = 165Å) (Figure 3-5B and Table 3-5). The D_{max} values are consistent with our crystal structures, where the 3-dimensional organization of RIα$_2$C$_2$ and RIα$_2$J-C$_2$ holoenzymes are similar. This size difference is mainly due to the presence of J-domain. The extra molecular weight and the presence of J-domain were reflected on the larger Porod volumes of DnaJB1-PKAc holoenzyme (269000Å^3 for RIα$_2$C$_2$ vs. 323000Å^3 for RIα$_2$J-C$_2$) as well as their molecular weight estimations (Table 3-5).

Similar R_g values can also be obtained from Guinier analysis (R_g = 52.39Å and R_g = 53.03Å for RIα$_2$C$_2$ and RIα$_2$J-C$_2$ holoenzyme, respectively) (Figure 3-5C). Based on the dimension of the crystal structures, the calculated R_g values for both RIα$_2$J-C$_2$ and RIα$_2$C$_2$ holoenzymes were determined. The calculated R_g value based on the RIα$_2$J-C$_2$ crystal structure is 43.48Å, which is slightly larger than the RIα$_2$C$_2$ holoenzyme (R_g = 42.35Å). Both of the Guinier and pair-distance distribution functions analyses are consistent with R_g values derived from the crystal structures, where RIα$_2$C$_2$ holoenzyme is smaller than RIα$_2$J-C$_2$ holoenzyme (Table 3-5).

Kratky plot analyses of the RIα$_2$J-C$_2$ holoenzyme, similar as wt holoenzyme, showed bell-shape peaks at low q, however neither of them converges to the q-axis at high q (Figure 3-5D). indicating that the complex, similar to the RIα$_2$C$_2$ holoenzyme, is a multi-domain protein with flexible regions. The results are consistent with our structures and MD simulations where we identified several dynamic/flexible domains as well as a flexible linker.

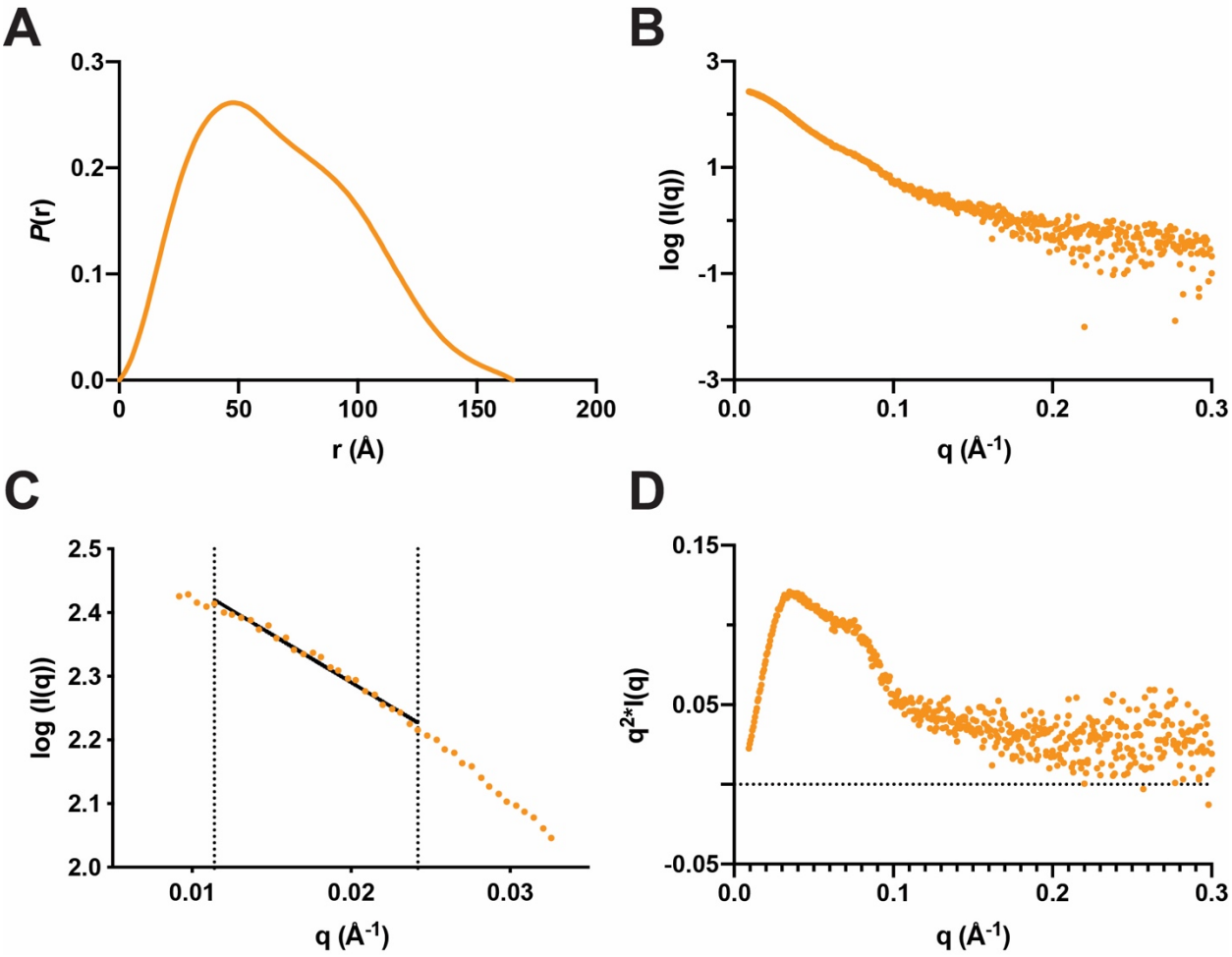

Figure 3-5. SAXS analysis of RIα_2J-C$_2$ holoenzyme. (A) P(r) function. (B) Scattering plot. (C) Guiner analysis. (D) Krakty plot.

Table 3-5. R_g and D_{max} values of $RI\alpha_2C_2$ and $RI\alpha_2J\text{-}C_2$ holoenzymes from SAXS.

	$RI\alpha_2C_2$	$RI\alpha_2J\text{-}C_2$
Crystal structure dimension (Å)	145.1 × 89.5 × 65.2	143.7 × 87.7 × 73.8
R_g (Å) from crystal structure	42.35	43.48
R_g (Å) from *P*(r)	52.08 ± 0.11	52.59 ± 0.11
D_{max} (Å) from *P*(r)	160	165
Porod Volume ($Å^3$) from *P*(r)	269000	323000
R_g (Å) from Guinier	52.39 ± 0.38	53.10 ± 0.42
MW estimation* (kDa)	166	190
Theoretical MW (kDa)	158	180

*Molecular weight estimation was obtained by Porod Volume / 1.7

3.3 Comparison between chimeric RIα$_2$J-C$_2$ and RIα$_2$C$_2$ holoenzyme

In both of the holoenzymes, the C-subunit part of the chimera is almost identical to the PKI-bound wt C-subunit structure (*31*). The only structural alteration is a more linear and extended αA-helix fused with the J-domain. Additionally, the J-C in the chimeric holoenzyme is superimposable to the previously reported (*16*) structure of the PKI-bound chimera, with a Cα atom RMSD of 0.40 Å. The fused J-domain in the chimeric holoenzyme is still tucked underneath the C-lobe with a contact area of ~380 Å^2. The J-domain in the chimeric holoenzyme structure is positioned in close proximity to the CNB-B domain of the adjacent RIα subunit, with the shortest Cα atoms distance at ~8 Å. The dynamic J-domain and the D/D domain with the N-linker regions may lead to the observed larger dimension of the chimeric RIα holoenzyme in SAXS experiments compared to the crystal structure (Table 3-5). The RIα:J-C protomer in the chimeric holoenzyme is structurally similar to the previously solved RIα:C heterodimers (*17*).

Besides the structural comparison, we also compared cAMP activation of the holoenzyme formed with J-C to holoenzyme formed with wt C-subunit. Holoenzyme formed with the fusion protein has similar cAMP activation properties as wt holoenzyme (EC_{50} = 29.86nM for C-subunit vs. EC_{50} = 30.37nM for J-C-subunit) (Figure 3-6). The EC_{50} and the cooperativity for cAMP activation are similar for both RIα$_2$J-C$_2$ and RIα$_2$C$_2$ holoenzyme.

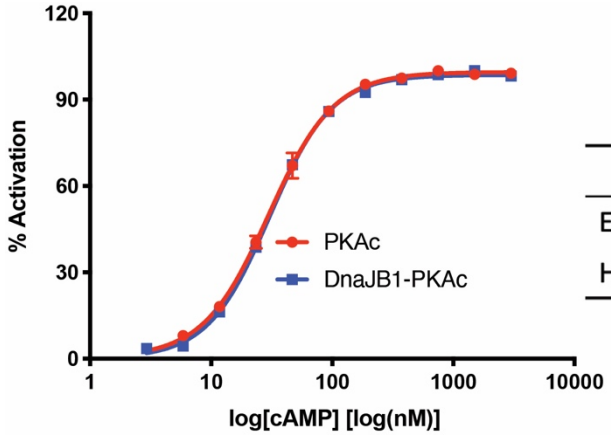

	PKAc	DnaJB1-PKAc
EC50 (nM)	29.86 ± 0.05	30.37 ± 0.07
HillSlope	1.61 ± 0.05	1.7 ± 0.07

Figure 3-6. Both RIα$_2$C$_2$ and RIα$_2$J-C$_2$ holoenzymes have similar cAMP sensitivity.

3.4 Dynamics

The MD simulation of RIα$_2$J-C$_2$ holoenzyme reveals a highly dynamic J-domain. Previous MD simulations and NMR studies of J-C-subunit alone also identified the dynamic feature of the J-domain(71). The J-domains in the holoenzyme remain flexible and assume several conformations in the simulations. According to the relative position of the J-domain in the holoenzyme, we could identify J-domain-In and J-domain-Out conformations. In the J-domain-In conformation the J-domain faces the holoenzyme core, whereas the J-domain flips out from the holoenzyme core to form J-domain-Out conformation.

In addition to the MD simulations, the structural analysis of RIα$_2$J-C$_2$ holoenzyme also reveals the flexible feature of J-domain(63). The J-domain in the chimeric holoenzyme has higher temperature factors (B-factor) than the rest of the holoenzyme, suggesting that it retains a high degree of flexibility in the holoenzyme similar to its PKI-bound state in solution based on NMR experiments (*29*) (Figure 3-7). This analysis is consistent with computational data, where the J-domain was flexible in the simulations.

Moreover, the J-domain can also affect the whole holoenzyme dynamics. Comparing the temperature factors of three holoenzymes, RIα$_2$J-C$_2$, RIα$_2$C$_2$ Molecule A, and RIα$_2$C$_2$ Molecule B, it is clear that not only different conformations have distinct holoenzyme dynamics, but also the presence of J-domain can affect the whole holoenzyme. Our temperature factor analysis shows the dynamic regions in RIα$_2$J-C$_2$ and RIα$_2$C$_2$ Molecule A are distinct. The high dynamic J-domain primes the flexibility of other motifs and domains in the other parts of holoenzymes.

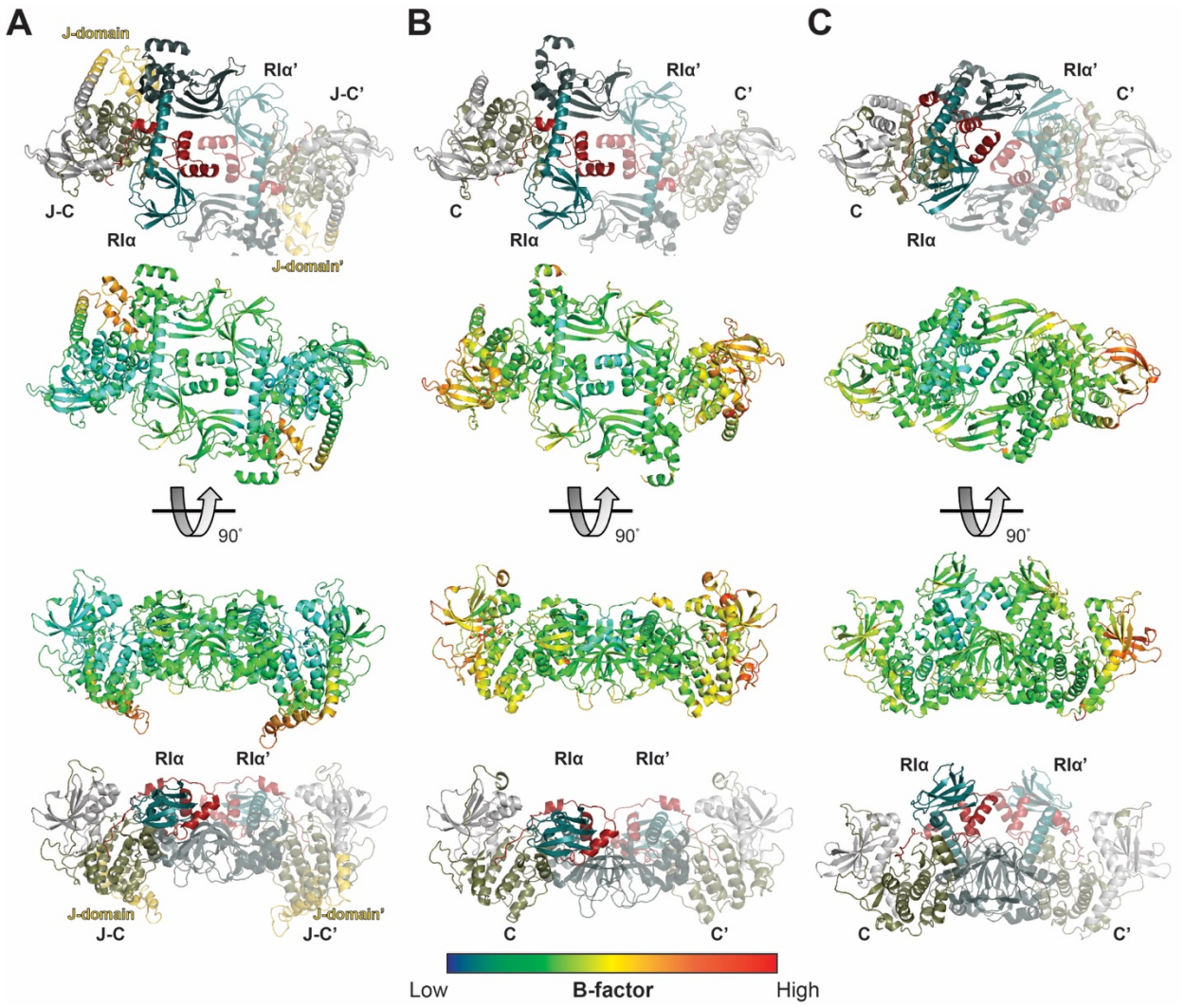

Figure 3-7. Different holoenzymes have different dynamics. (A) Temperature factor of the RIα$_2$J-C$_2$ holoenzyme crystal structure. (B) Temperature factor of the RIα$_2$C$_2$ Molecule A holoenzyme crystal structure. (C) Temperature factor of RIα$_2$C$_2$ Molecule B holoenzyme crystal structure.

3.5 Discussion

The oncogenic J-C has been crystallized here in one of its most important physiological states where it is associated in a holoenzyme complex with the RIα-subunit. The identification of different conformational states for both wt and chimeric RIα holoenzymes may guide the development of drugs that selectively target not only the J-domain and catalytic core to directly block chimera activity, but also regions present only at the holoenzyme level to block holoenzyme activation. Using a strategy that simultaneously blocks the oncogenic driver kinase and its holoenzyme would significantly reduce the possibility that a random mutation in the driver enables the tumor cells to escape treatment. RIα is a critical master switch for regulating PKA activity in cells, and it is likely that unregulated PKA activity is important, at least in part, for driving FL-HCC.

The importance of RIα is further supported by the recent finding that in a few rare cases, CNC mutations in RIα can drive FL-HCC(72). This study can now link CNC disease and FL-HCC to a specific structural feature at the PKA holoenzyme level. The increased PKA activity in patients with CNC who harbor N3A motif mutations is likely the result of increased cAMP sensitivity for holoenzyme activation and decreased inhibition capacity of the R-subunit for the catalytic subunit. MD simulations show that the J-domain is highly dynamic in the chimeric RIα holoenzyme. The presence of the J-domain will likely alter the phospho-proteome of the tumor cells. At this point it is not clear how the presence of the J-domain influences the function of the PKA holoenzymes in cells. It will be of interest to elucidate how the conformational state and abundance of the different holoenzymes in the tumor cells and the holoenzymes communicate with their neighbors and substrates. In particular, it is important to determine how these macromolecular assemblies are altered in FL-HCC by comparing paired tumor and adjacent normal liver samples. Understanding

in detail how J-C signaling pathways drive disease will shed light on understanding its transformation to FL-HCC and is expected to improved diagnosis and therapeutic treatment for this cancer.

3.6 Acknowledgment

Chapter 3 includes the material that appears appears in Cao, B.*; Lu, T.-W.*; Fiesco, J. A. M.*; Tomasini, M.; Fan, L.; Simon, S. M.; Taylor, S. S.; Zhang, P. “Structures of the PKA RIα Holoenzyme with the FLHCC Driver J-PKAcα or Wild-Type PKAcα” *Structure* **2019**, *27*, 816-828 e814. The dissertation author is one of the primary authors of this manuscript. *contributed equally.

Chapter 4 The RIIβ holoenzyme with DnaJB1-PKAc

To understand the pathological consequences of FL-HCC, we used single particle cryo-electron microscopy (cryo-EM) to determine a structure of the RIIβ holoenzyme formed with J-C. The organization of the DnaJB1-PKAc RIIβ holoenzyme ($RII\beta_2J\text{-}C_2$) is similar to what was found earlier in the previously solved crystal structure of the wt RIIβ holoenzyme ($RII\beta_2C_2$); the overall quaternary organization was not altered by the addition of the J-domain, which is also resolved in our structure. In contrast to the previous wt RIIβ holoenzyme crystal structure, where the D/D domain was not visible, the general position of the D/D domain is seen in the cryo-EM structure and confirmed by small-angle X-ray scattering (SAXS). Both our MD simulation data and the cryo-EM structure showed that the presence of the J-domain in this protein complex can change the dynamic features of holoenzyme compared to the wt RIIβ holoenzyme, especially the CNB-B domains, and both methods reveal an intrinsic asymmetry in the two RIIβ:J-C protomers. MD simulations of the wt RIIβ holoenzyme also reveal a dramatic asymmetry in the CNB-B domains that was hidden in the crystal structure. The asymmetry in the mutant holoenzyme is due to the flexibility in one protomer of the CNB-B domain in the RIIβ-subunit and the J-domain and the αA-helix in the J-C-subunit. In addition to the chimeric protein holoenzyme with RIIβ is activated more readily by cAMP than the wt RIIβ holoenzyme. Our studies of the $RII\beta_2J\text{-}C_2$ structure, dynamics and function demonstrate the power of combining crystallography, MD simulations and cryo-EM to elucidate the dynamic features of a holoenzyme complex and also provide us with a better understanding of FL-HCC that hopefully shed light on new potential therapeutic strategies.

4.1 Structural analysis of DnaJB1-PKAc RIIβ holoenzyme

In the DnaJB1-PKAc chimera, the extra J-domain replaces exon 1 (residue 1-14) of wt C-subunit and forms four helices with the terminal helix being contiguous with the αA-helix (Figure 4-2A). In order to confirm the architecture of the complex, we first performed negative stain single-particle EM and single-particle analysis on the $RII\beta_2J\text{-}C_2$ holoenzyme (Figure 4-1 and Figure 4-2). Inspection of both micrographs and 2D class averages indicated that the $RII\beta_2J\text{-}C_2$ holoenzyme possessed a similar overall structure as the wt RIIβ holoenzyme forming a tetrameric complex with a C2 axis of symmetry at the central hole (Figure 4-1B and C). Comparison of reprojections of the wt RIIβ holoenzyme (PDB = 3TNP) with 2D averages further confirmed a similar architecture (Figure 4-1C). These data allowed us to conclude that the mutant $RII\beta_2J\text{-}C_2$ holoenzyme is similar to the wt RIIβ holoenzyme at low resolution.

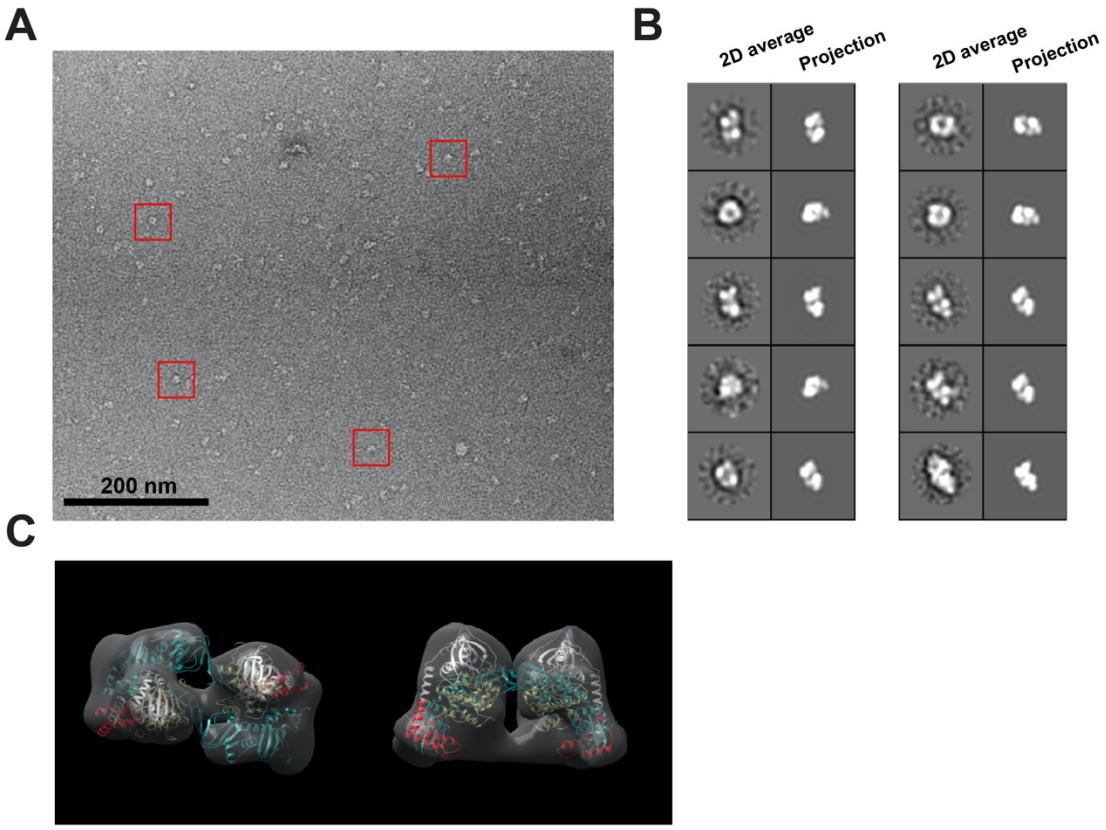

Figure 4-1. Negative stain EM confirms that RIIβ$_2$J-C$_2$ and WT RIIβ holoenzymes have similar architectures. (A) Representative micrograph for negatively-stained RIIβ$_2$J-C$_2$ holoenzyme. Example particles are shown in red boxes. (B) 2D class averages of RIIβ2J-C2 shown alongside projections of WT RIIβ holoenzyme crystal structure. The WT RIIβ$_2$C$_2$ crystal structure was filtered to 20Å. (C) Model and negatively stained EM density of RIIβ$_2$J-C$_2$ holoenzyme.

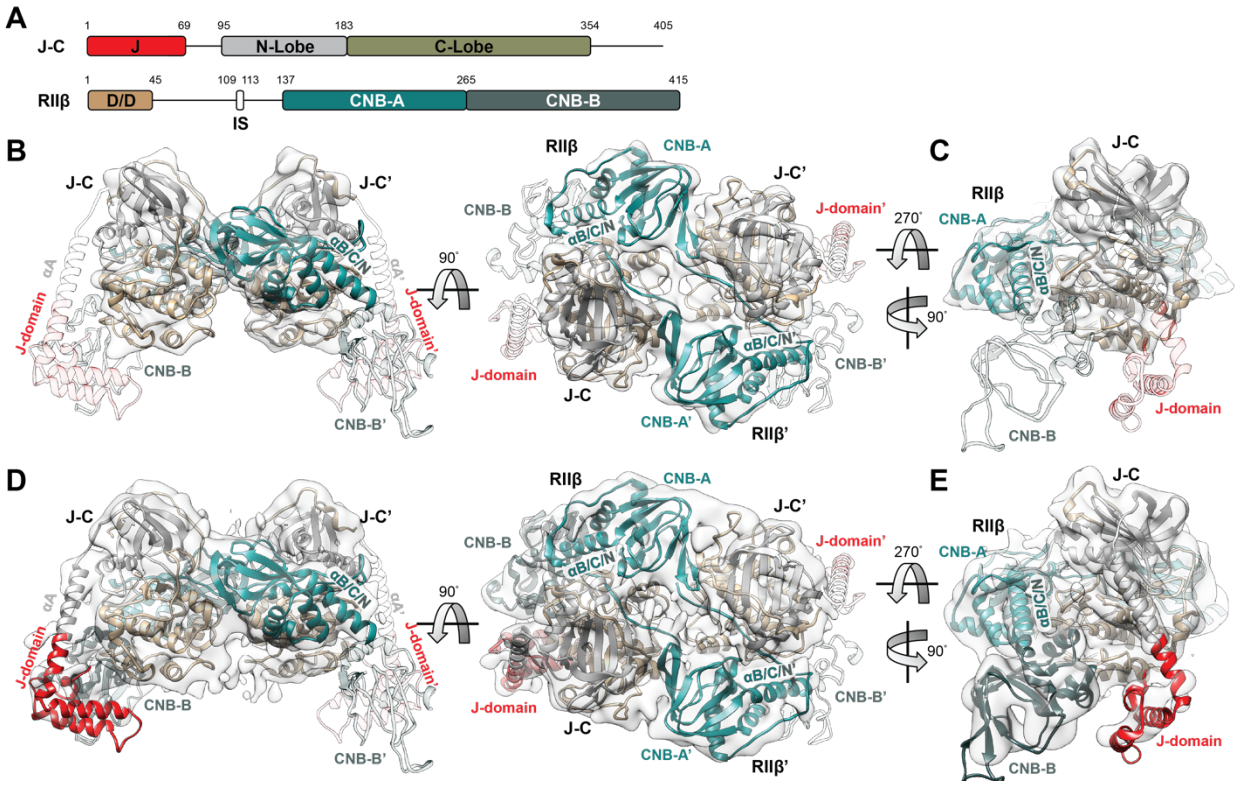

Figure 4-2. CryoEM structure of RIIβ$_2$J-C$_2$ holoenzyme. (A) Domain diagram and color coding of RIIβ$_2$J-C$_2$ holoenzyme. (B) & (C) Cryo-EM structure RIIβ2J-C2 holoenzyme at 6 .2Å with C2 symmetry imposed. (D) & (E) Structure of RIIβ$_2$J-C$_2$ holoenzyme structure at 7.5Å after classification reveals presence of ordered J-domain and CNB-B domain.

To obtain higher-resolution information, we used cryo-EM to determine a structure of the RIIβ_2J-C_2 holoenzyme. Due to a preferred orientation on the cryo-EM grid, data were collected using a tilt angle of 40°. After 2D classification and 3D reconstruction, we are able to get the structure to an average resolution of 6.2Å with C2 symmetry imposed (Figure 4-2B and C and Table 4-1). The structures revealed clear density in the core region of RIIβ_2J-C_2 holoenzyme, but density for the J-domain in the J-C-subunits as well as for the CNB-B domains in the RIIβ-subunits was missing (Figure 4-3). In addition, the density for the entire αA-helix as well as the linker that wraps around the N-lobe that connects the αA-helix to the β-strand 1 was missing. It is flexible with a break at $Asp96^{J\text{-}C}$ (equivalent to $Asp41^{C}$ in the WT C-subunit) (Figure 4-3A). The density for the αB/C/N-helix ends after the αC-helix in the CNB-A domain ($Tyr265^{RII\beta}$), while density for the αN-helix in the CNB-B domain is missing (Figure 4-3B). Presumably, these un-resolved or flexible domains are dynamic regions that form continuous states under cryo-EM conditions.

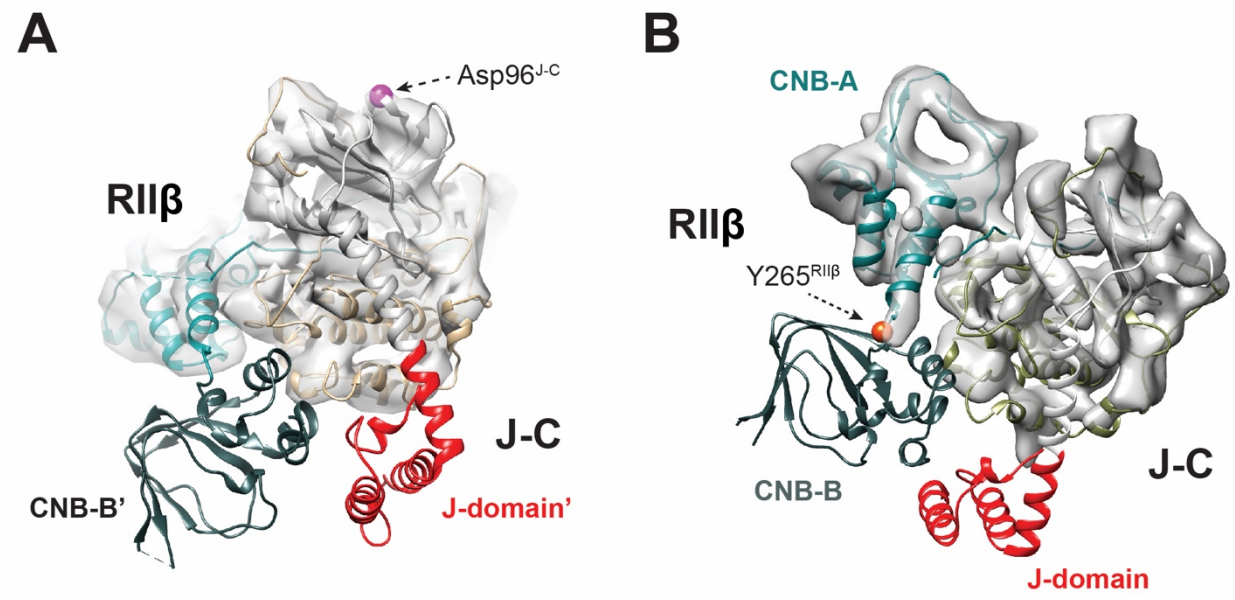

Figure 4-3. CryoEM structure of RIIβ$_2$J-C$_2$ holoenzyme reveals domain dynamics. (A) The electron density of the J-C-subunit starts at Asp97^{J-C}. (B) The electron density of the RIIβ-subunit ends at Tyr265^{RIIβ}.

We then further masked the core regions and focused on local areas for refinement. After continued classification and refinement, we were able to visualize one side of the J-domain and CNB-B domain together with clear density for the αB/C/N-helix (Figure 4-2D). The overall structure reveals distinct density for one complete RIIβ:J-C protomer, especially the contiguous αB/C/N-helix (αB-helix, αC-helix, and αN-helix), the CNB-B domain and the J-domain. In this protomer, the J-domain and CNB-B domain are in close proximity (Figure 4-2E). In contrast, the J-domain and CNB-B domain as well as the αA-helix in the J-C-subunit remain un-resolved in the other protomer. This asymmetry could be an essential mechanistic feature of the RIIβ holoenzyme. This phenomenon has not been observed previously, and most likely cannot be trapped by conventional crystallography. For example, in our previous crystal structure of the RIIβ holoenzyme, the temperature factors are high in αA-helix of the C-subunits and in the CNB-B domains of RIIβ-subunit; however, any potential asymmetry is averaged out in the crystal structure and/or obscured by crystal. By using cryo-EM 3D reconstruction, we are able to observe this state that could represent an important event in PKA activation.

Table 4-1. Cryo-EM data collection, refinement and validation statistics.

Structure: RIIβ$_2$J-C$_2$		
Data collection		
Grids	Gold UltrAuFoil 1.2/1.3	
Vitrification method	FEI Vitrobot	
Microscope	Titan Krios	
Magnification	29000X	
Voltage (kV)	300	
Stage tilt (°)	40	
Detector	K2 Summit	
Recording mode	Counting	
Dose rate (e^-/pix/sec)	7.789	
Total electron exposure (e^-/Å^2)	77.9	
Number of frames	100	
Defocus range (μm)	1 - 3	
Pixel size (Å)	1.0	
Number of micrographs	1,129	
Initial particle images (no.)	642,843	
Data processing: C2 symmetry		
Final particle images (no.)	69,605	
Symmetry	C2	
Map resolution (Å)	6.2	
Data processing: C1 symmetry		
Final particle images (no.)	11,182	
Symmetry	C1	
Map resolution (Å)	7.5	
Refinement		
Initial model used (PDB code)	3TNP, 4WB7	
Symmetry	C1	C2
PDB code	6WJF	6WJG
EMDB code	EMD-21692	EMD-23693
Model resolution (Å)	7.5	6.2
FSC threshold	0.143	0.143
Map sharpening *B* factor (Å^2)	-500	-302
Model composition		
Non-hydrogen atoms	9527	7708
Protein residues	1172	944
Ligands	0	0
B factors (Å^2)		
Protein (min/max/mean)	30/850/350	30/550/300
Ligand	N/A	N/A
R.m.s. deviations		
Bond lengths (Å)	0.004	0.003
Bond angles (°)	0.878	0.875
Validation		
MolProbity score	1.88	1.81
Clash score	4.64	3.72
Rotamer outliers (%)	0	0
Ramachandran plot		
Favored (%)	85.65	85.36
Allowed (%)	14.35	14.64
Disallowed (%)	0	0

4.2 Molecular dynamics simulations reveal asymmetry in the RIIβ holoenzyme

To further explore the dynamic features of the two RIIβ holoenzymes we used Molecular Dynamics (MD) simulations and found surprisingly that RIIβ holoenzymes form with wt C-subunit and the J-C-subunit have very different domain dynamics. Three independent 500ns MD simulations were carried out to further explore these differences. The Root-Mean-Square-Fluctuation (RMSF) analyses of each holoenzyme demonstrated distinct backbone dynamics between wt and fusion holoenzymes. In all structures, the first 14 residues of the C-subunit and the last 23 residues of the RIIβ subunit in addition to its linker region and D/D domain (residues 1-103) are not included in the simulations.

4.2.1 Wild-type RIIβ holoenzyme.

In the $RII\beta_2C_2$ holoenzyme, both N- and C-lobes of the C-subunit are stable with the exception of the first 14 residues (exon 1) which are not seen in the crystal structure and not included in the simulation. Indeed, both lobes show low RMSF throughout the entire simulation (Figure 4-4A). In contrast, one of the CNB-B domains in the RIIβ-subunit is highly flexible (Figure 4-4B). The flexible region begins approximately at residue $Tyr265^{RII\beta}$, which is at the junction of the αC-helix in the CNB-A domain and the αN-helix in the CNB-B domain (Figure 4-4B and C). Within the highly dynamic features of the CNB-B domains, some local regions, such as the N-terminal linker and the β4-β5 loops in the CNB-B domains showed especially high RMSF. In addition, one small dynamic region (residues 122 to 129) was also seen in the linker that joins the inhibitor sequence to CNB-A (Figure 4-4B); this dynamic segment wraps around the αB/C/N-helix. These regions, as well as the C-terminal 23 residues, are both un-resolved in the previous $RII\beta_2C_2$

crystal structure(22). A deeper analysis of our simulation results further confirmed the dynamic properties of these two regions. By overlaying the conformational ensemble from the simulations, we can more clearly appreciate the distinct dynamic properties of the two CNB domains in the $RII\beta_2C_2$ holoenzyme (Figure 4-4D and E). One of the protomers reveals a relatively stable CNB-B domain, while the other CNB-B domain is highly flexible. In both protomers, $Tyr265^{RII\beta}$ serves as a pivot point; however, in one of the protomers, the entire CNB-B domain, including the αN-helix, is extremely flexible after $Tyr265^{RII\beta}$. The MD simulation data further confirms the dynamic regions that we observed in the cryo-EM structure both being characterized by breaks at $Tyr265^{RII\beta}$.

$Tyr265^{RII\beta}$ and the dynamic properties of the αB/C/N-helix are important for RIIβ holoenzyme activation. The long αB/C/N-helix is the signature feature of all PKA holoenzymes. Once activated by cAMP, the αB/C/N-helix divides into three segments (αB-helix, αC-helix and αN-helix) (Figure 4-4F and G). Several studies have already pointed out the importance of the flexibility of the αB/C/N-helix in activation of the RIα holoenzyme (60, 61, 73). Here we show that the αB/C/N-helix is also very dynamic, but different, in the RIIβ holoenzyme. Each isoform has the same hinge points, one is between the αB-helix and the αC-helix and the other is between the C-helix and the αN-helix. Most importantly, however, the major hinge points are different. The major hinge point in RIIβ, $Tyr265^{RII\beta}$, is located at the junction of the αC-helix and the αN-helix (Figure 4-4F); while $Leu233^{RI\alpha}$, between the αB- and the αC-helix, is the more prominent pivot point for RIα (Figure 4-4G). To quantitate these differences, we measured the hinge angles of αB-helix/αC-helix and αC-helix/N-helix in the cAMP-bound form structures of both RIα and RIIβ (PDB=1RGS and 1CX4, respectively). The angle between the αB- and αC-helix is larger in RIα than in RIIβ; however, RIIβ has larger hinge angle between the αC- and αN-helix (Figure 4-4F and G), which is the precise junction between the two CNB domains.

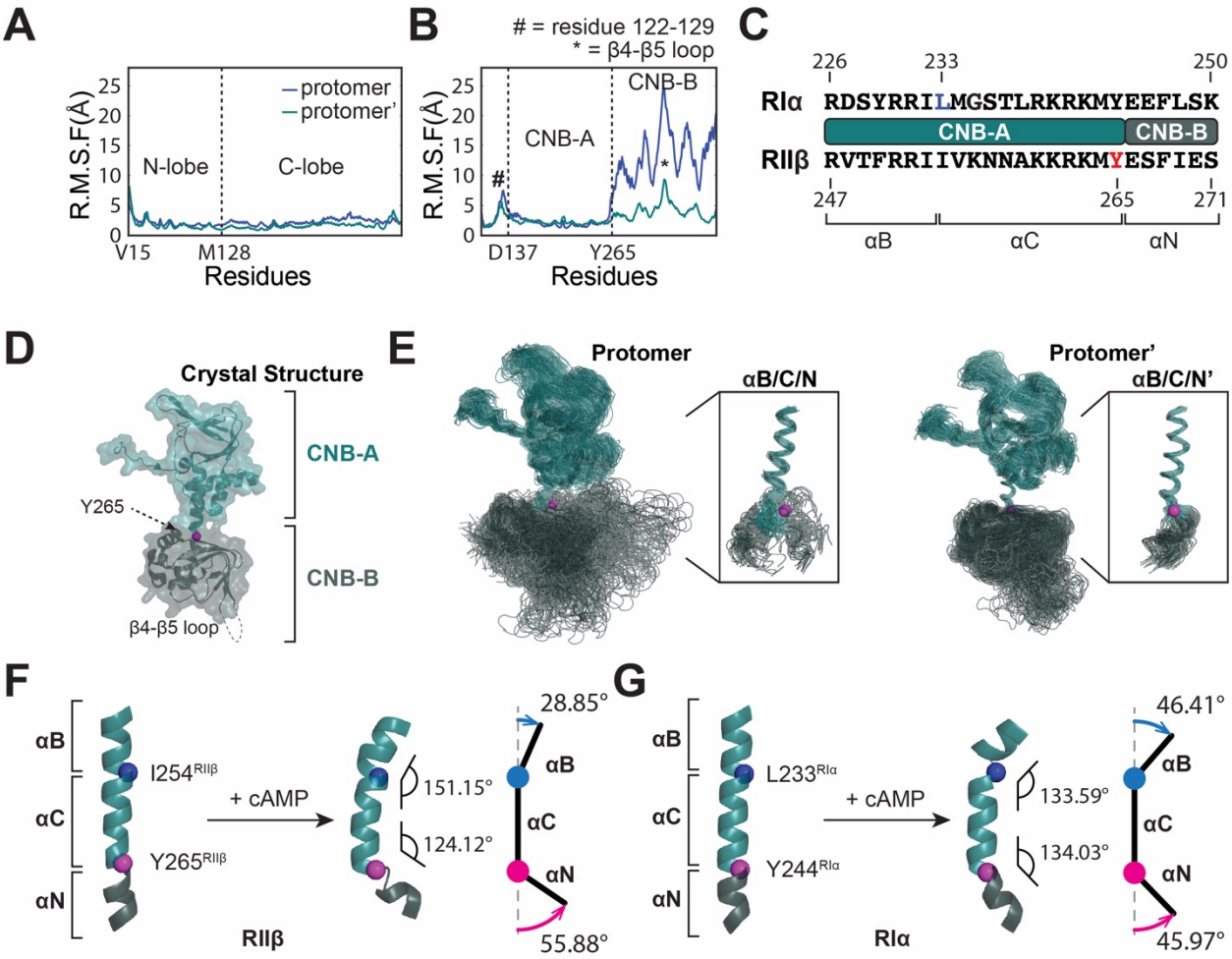

Figure 4-4. MD simulations of RIIβ$_2$C$_2$ holoenzyme reveal functional and isoform-specific dynamics. (A) Both N- and C-lobe of C-subunit remain stable in the RMSF analysis of RIIβ$_2$C$_2$ holoenzyme. (B) CNB-B domain of RIIβ-subunit in one of the protomers is flexible in the RMSF analysis in RIIβ$_2$C$_2$ holoenzyme. (C) Domain diagram and residues of αB/C/N-helix in RIα and RIIβ-subunit. (D) RIIβ-subunit in RIIβ$_2$C$_2$ holoenzyme crystal structure (PDB ID=3TNP). (E) The overlaid of all states of each RIIβ-subunit protomer in RIIβ2C2 holoenzyme from MD simulations. CNB-domain in one of the protomers is more flexible than the other, and both of the protomers have breakages at Tyr265. Residue Tyr265^{RIIβ} was shown as pink ball. (F), (G)The conformational change of RIIβ (F) and RIα (G) αB/C/N-helices upon cAMP stimulation. The main pivot point of RIIβ αB/C/N-helix is at Tyr265^{RIIβ} (G), while the main pivot point of RIα αB/C/N-helix is at Leu233^{RIα} (G).

In addition to differences in their dynamics, the αB/C/N-helix in RIα and RIIβ, which share 53% sequence identity, also have distinct helical, N-capping, and C-capping propensities (Figure 4-5A, B, and C). The αB/C/N-helix of RIα has very high helical propensity with a local minimum at $Gly235^{RI\alpha}$, which is near the primary hinge point ($Leu233^{RI\alpha}$) for the cAMP-bound RIα (73). In RIIβ, the helical propensity of the αB/C/N-helix is much lower compared to RIα, perhaps allowing it to take advantage of the natural hinge point between the two CNB domains, $Tyr265^{RII\beta}$ (Figure 4-4E and Figure 4-5A).

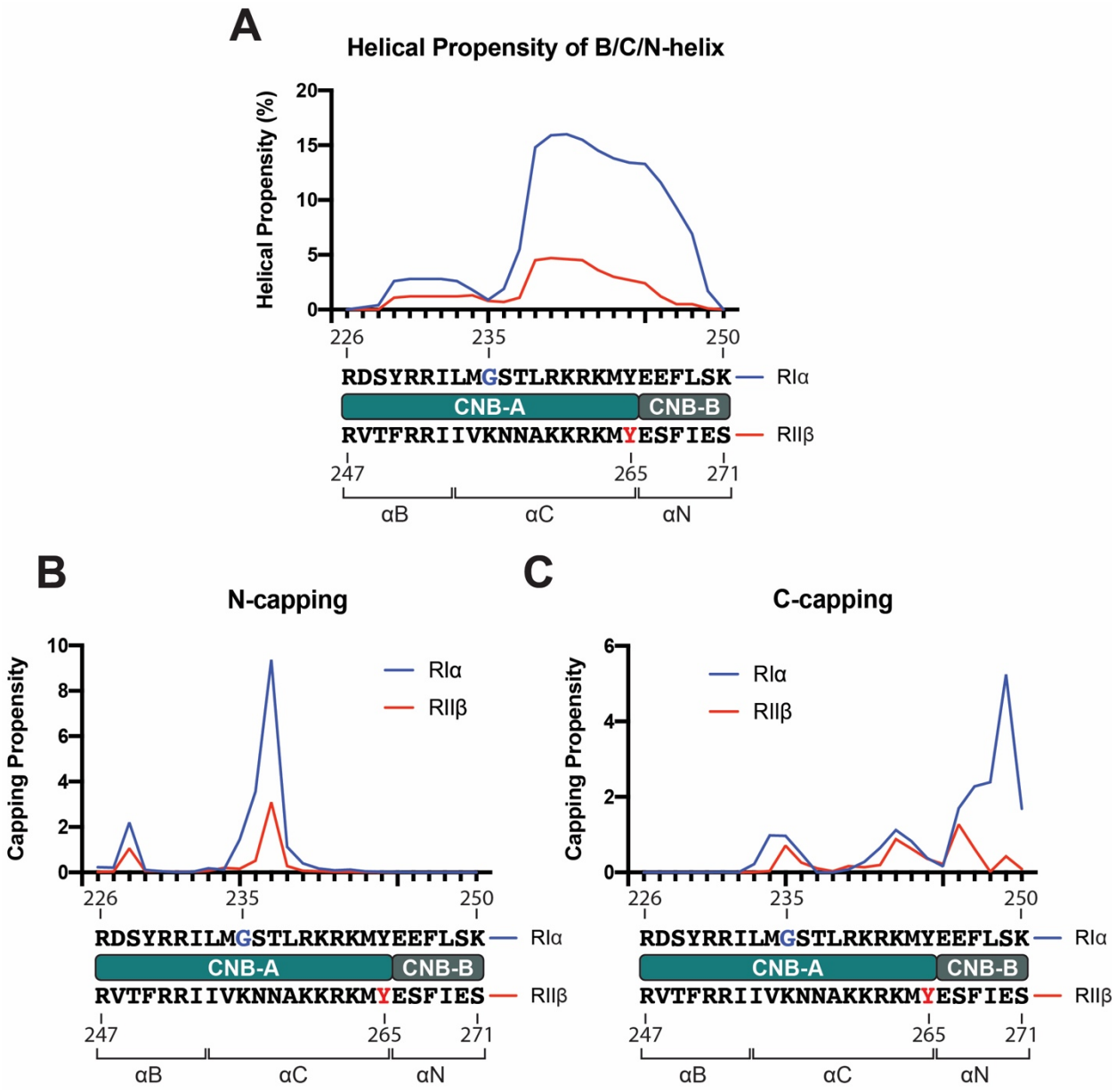

Figure 4-5. Helical propensity and capping residues analyses of αB/C/N-helix. (A) Helical propensity of αB/C/N-helix. (B) N-capping residue analysis of αB/C/N-helix. (C) C-capping residue analysis of αB/C/N-helix.

4.3 RIIβ$_2$J-C$_2$ holoenzyme

The RIIβ$_2$J-C$_2$ holoenzyme simulations showed different dynamics compared to wt holoenzyme. Both the N- and C-lobes of J-C-subunit are as stable as wt; however, the extra J-domain in the J-C-subunits show much higher RMSF values than the kinase portion of the fusion protein (Figure 4-6A). The addition of J-domain in the J-C-subunit also has an effect on the dynamics of the RIIβ-subunit. Unlike the CNB-B domains in the RIIβ$_2$C$_2$ holoenzyme, both of the CNB-B domains in RIIβ$_2$J-C$_2$ holoenzyme remain strikingly more stable during the simulation (Figure 4-6B and Figure 4-7). The J-domain presumably can stabilize the CNB-B domains either through spatial steric effects or direct interactions. This close communication between the J-domain and the CNB-B domain is captured in one of the protomers in our cryo-EM structure (Figure 4-2D and Figure 4-6C). The close proximity of the J-domain and the CNB-B domain suggests that their dynamic properties are coupled. The other feature that is revealed by the cryo-EM structure is that the αA-helix in one J-C-subunit is also missing suggesting that the J-domain influences not only the CNB-B domain but also the αA-helix that it is directly fused to β-strand 1 in the N-lobe (Figure 4-2D and Figure 4-6C).

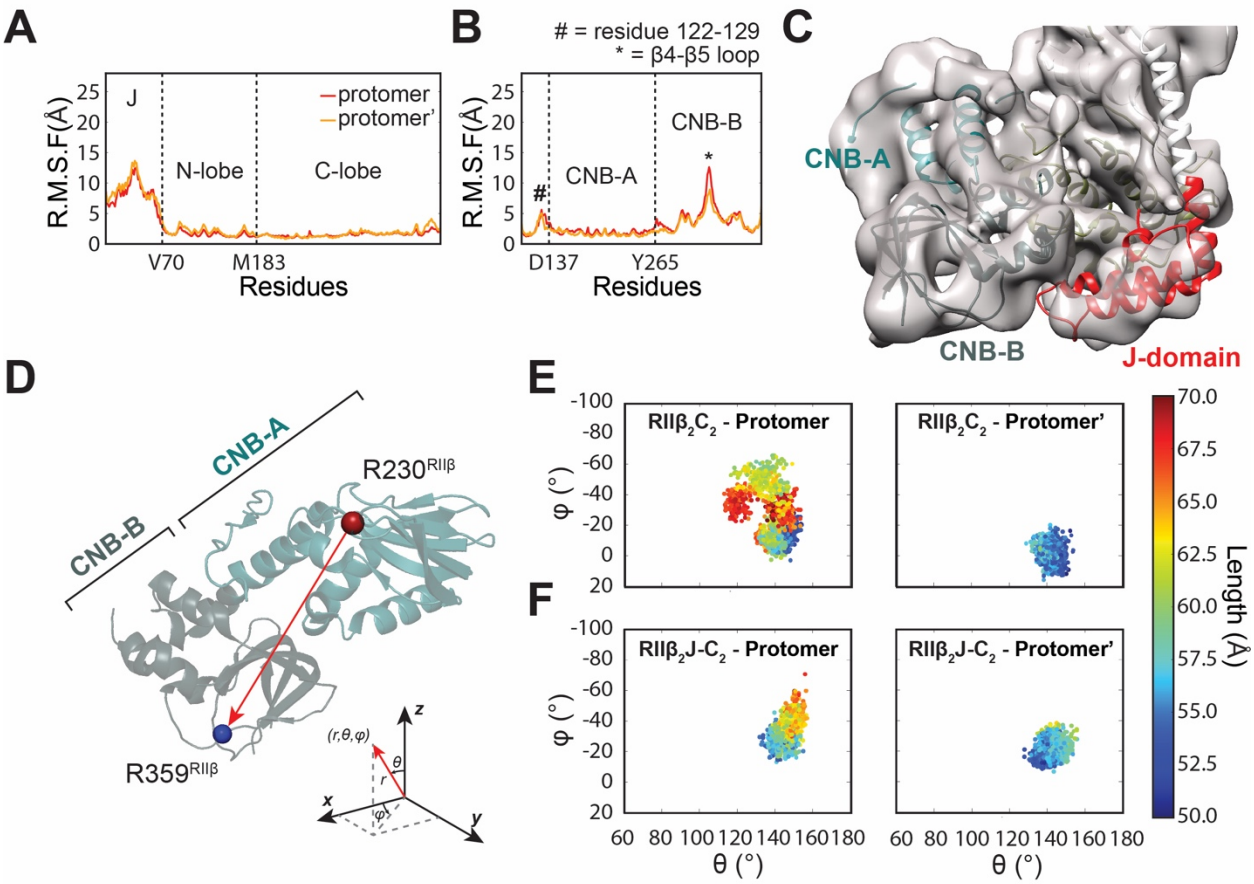

Figure 4-6. MD simulations of RIIβ$_2$J-C$_2$ holoenzyme reveal distinct dynamics. (A) Both N- and C-lobe of J-C-subunit remain stable but J-domain is flexible in the RMSF analysis of RIIβ$_2$J-C$_2$ holoenzyme. (B) CNB-B domain of RIIβ-subunit in both protomers remain stable in the RMSF analysis in RIIβ$_2$C$_2$ holoenzyme. (C) J-domain and CNB-B domain of RIIβ$_2$J-C$_2$ holoenzyme are in close proximity. (D) The representation of polar coordinate vector from Arg230^{RIIβ} to Arg359^{RIIβ}. (E), (F) The plots of φ, θ, and length of the vectors from Arg230^{RIIβ} to Arg359^{RIIβ} in MD simulations of RIIβ$_2$C$_2$ (E) and RIIβ$_2$J-C$_2$ holoenzymes (F). The vector in one of the protomers of RIIβ$_2$C$_2$ holoenzyme moves and fluctuates significantly (E), whereas the vectors in both protomers of RIIβ$_2$J-C$_2$ holoenzyme remain stable (F).

We can also visualize the differences in dynamics of the CNB domains in the DnaJB1-PKAc and wt RIIβ holoenzymes by measuring the polar vector between CNB-A and CNB-B domains. The vector was chosen from $Arg230^{RII\beta}$ in the PBC of CNB-A domain to $Arg359^{RII\beta}$ in the PBC of CNB-B domain (Figure 4-6D). The plots of φ, θ, and length of the vectors demonstrated clearly the different dynamics between the two CNB domains in the DnaJB1-PKAc and in wt PKAc RIIβ holoenzymes. In the $RII\beta_2C_2$ holoenzyme, the vector in one of the protomers moves and fluctuates significantly; distance between domains varies from 50 to 70Å with a wide range of φ and θ angles movements (Figure 4-6E). The vector in the other protomer, however, is relatively less dynamic in both the φ and/or θ axis and length. The asymmetric dynamics of the CNB domains in each protomer of the $RII\beta_2C_2$ holoenzyme can also be observed here. In contrast, the vectors in both protomers of $RII\beta_2J\text{-}C_2$ holoenzyme remain relatively more stable. The plot of φ, θ, and length of the vectors in $RII\beta_2J\text{-}C_2$ holoenzyme showed less disperse angles and lengths movements (Figure 4-6F), and both vectors in the protomers populate a smaller φ, θ-space with less diverse length fluctuations. Asymmetric dynamics is also present in the $RII\beta_2J\text{-}C_2$ holoenzyme (Figure 4-6F).

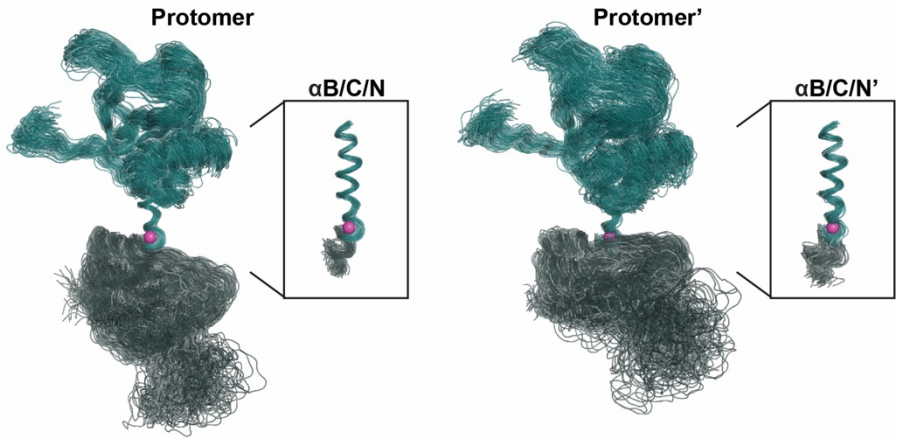

Figure 4-7. The overlaid of all states of each RIIβ-subunit protomer in RIIβ$_2$J-C$_2$ holoenzyme from MD simulations. Both of the protomers have breakages at Tyr265. Residue Tyr265^{RIIβ} was shown as pink ball.

4.4 SAXS analysis and localization of the D/D domain

The solution structures of both wt and DnaJB1-PKAc RIIβ holoenzymes were also determined by SAXS coupled with size-exclusion chromatography to support our cryo-EM structure. Based on pair-distance distribution functions *P(r)*, both holoenzymes have similar dimension (D_{max} = 129.09Å for wt holoenzyme and D_{max} = 128.63Å for DnaJB1-PKAc holoenzyme). The D_{max} values are consistent with our cryo-EM structure, where the 3-dimensional organization of $RII\beta_2C_2$ and $RII\beta_2J\text{-}C_2$ holoenzyme are similar. (Figure 4-8A, B and Table 4-2). However, the DnaJB1-PKAc holoenzyme has a larger R_g value than wt holoenzyme (R_g = 41.69Å for wt holoenzyme and R_g = 43.13Å for DnaJB1-PKAc holoenzyme). A similar trend of R_g values can also be obtained from Guinier analyses (R_g = 41.41Å and R_g = 43.29Å for wt and DnaJB1-PKAc holoenzyme, respectively) (Figure 4-9A, B, and Table 4-2). The higher molecular weight of DnaJB1-PKAc can explain why $RII\beta_2J\text{-}C_2$ holoenzyme has a larger radius of gyration.

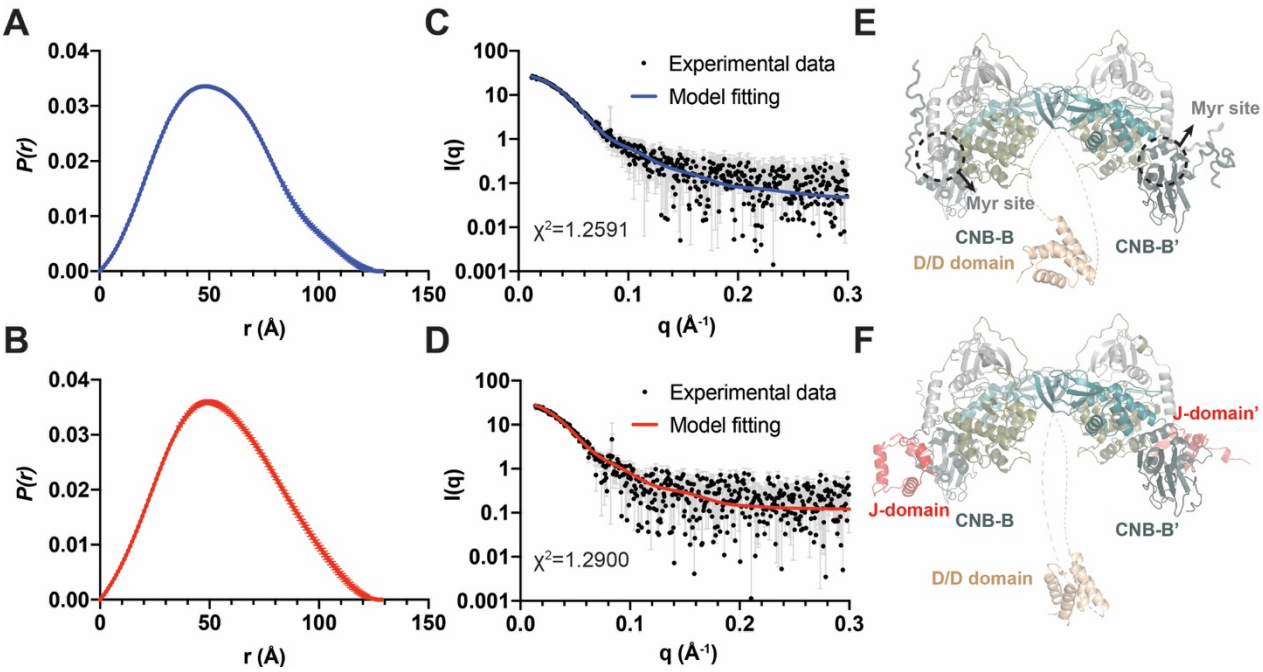

Figure 4-8. SAXS analyses of RIIβ$_2$C$_2$ and RIIβ$_2$J-C$_2$ holoenzymes. (A) & (B) P(r) functions of RIIβ$_2$C$_2$ (A) and RIIβ$_2$J-C$_2$ (B) holoenzymes. (C) & (D) Scattering plots and the model fittings of RIIβ2C2 holoenzyme with χ2=1.2591 (C) and RIIβ2J-C2 holoenzyme with χ2=1.2900 (D). (E) & (F) The SAXS models of RIIβ$_2$C$_2$ (E) and RIIβ$_2$J-C$_2$ holoenzymes (F).

Table 4-2. R_g and D_{max} values of RIIβ$_2$C$_2$ and RIIβ$_2$J-C$_2$ holoenzymes from SAXS.

	RIIβ$_2$C$_2$	RIIβ$_2$J-C$_2$
R_g (Å) from *P*(r)	41.69 ± 0.28	43.13 ± 0.41
D_{max} (Å) from *P*(r)	129.09	128.63
Porod Volume (Å^3) from *P*(r)	290000	347000
R_g (Å) from Guinier	41.41 ± 0.49	43.29 ± 0.61
MW estimation* (kDa)	171	204
Theoretical MW (kDa)	173	187

*Molecular weight estimation was obtained by Porod Volume / 1.7

The higher molecular weight and the presence of the J-domain were also reflected in the larger Porod volumes of DnaJB1-PKAc holoenzyme (290000Å^3 for RIIβ$_2$C$_2$ vs. 347000Å^3 for RIIβ$_2$J-C$_2$) (Table 4-2). The molecular weight can be estimated by dividing the Porod volume by 1.7 according to the method of Petoukhov *et al.* (74). The estimated molecular weight of RIIβ$_2$C$_2$ was obtained as 171kDa in comparison to its theoretical molecular weight of 173kDa (Table 4-2). The estimated molecular weight of the RIIβ$_2$J-C$_2$ holoenzyme was 204kDa, while its theoretical molecular weight is 186kDa (Table 4-2). Considering that the flexible J-domain enhances the domain dynamics of the holoenzyme, the result is that it delocalizes over a larger volume(75). This can explain why RIIβ$_2$J-C$_2$ holoenzyme has a larger deviation between estimated and theoretical molecular weights than wt holoenzyme.

We further analyze Kratky plots of these two holoenzymes, which can provide a way to assess the degree of flexibility within the scattering macromolecules. Kratky plot analyses of these two holoenzymes showed bell-shape peaks at low q, however neither of them converges to the q-axis at high q (Figure 4-9C and D) indicating that both of the complexes are multi-domains proteins with flexible regions(75). These results are consistent with our structures and MD simulations where we identified several dynamic/flexible domains as well as a flexible linker.

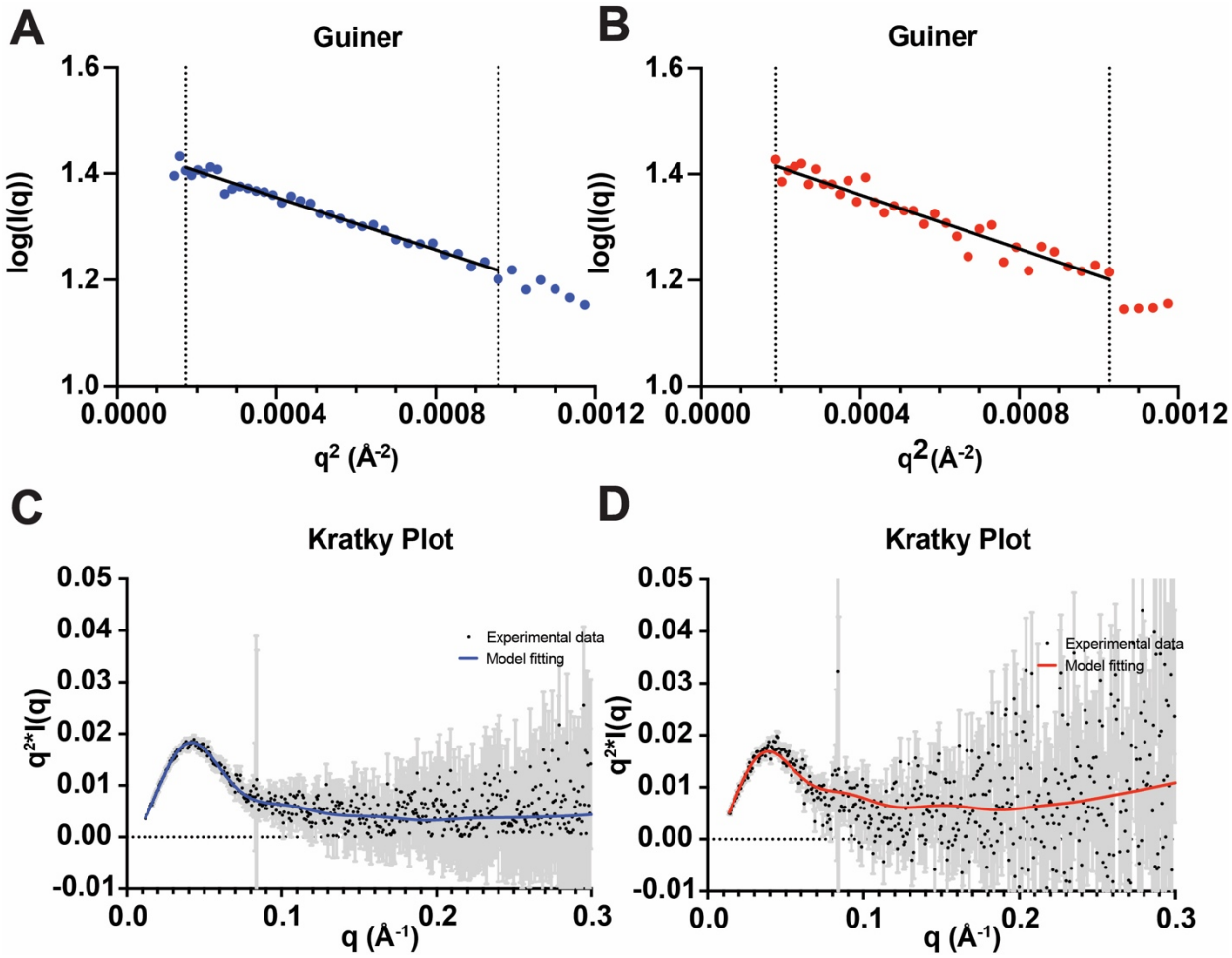

Figure 4-9. Guiner analysis and Krakty plot of RIIβ$_2$C$_2$ (A) & (C) and RIIβ$_2$J-C$_2$ holoenzymes (B) & (D).

To fit the SAXS data, we used the wt crystal structure as a starting model and further considered the dynamic properties of each domain. The missing linkers were built as flexible poly-Gly chains while the missing D/D domain was generated using homology models from an online protein structure prediction software program, I-TASSER(76). Both of our holoenzyme models fit the experimental SAXS data well (χ^2=1.2591 and χ^2=1.2900 for wt and J-C holoenzyme, respectively) (Figure 4-8C and D). In both of the holoenzyme models, the D/D domain of RIIβ localizes on the same face as the CNB-B domains and the myristylation (Myr) sites of the C-subunit (Figure 4-8E and F).

Although the position of the D/D domain cannot be identified unambiguously in our cryo-EM structure due to its flexibility, the extra density in our structure nevertheless provides supporting evidence for the position of the D/D domain (Figure 4-10). The first visible N-terminal residue in our RIIβ structure is Ile104^{RIIβ}, which positions at the hole formed by the two RIIβ:J-C protomers (Figure 4-10A). The extra density locates at the center of the RIIβ holoenzyme, close to Ile104^{RIIβ} and extends along the central hole to the same surface where the CNB-B domains and J-domains are located (Figure 4-10B). It suggests that the previously un-resolved N-terminal regions of RIIβ thread through the central hole of the RIIβ holoenzyme and that the D/D domain tethers on the bottom side of RIIβ holoenzyme in close proximity to the CNB-B domains, the J-domain, and the bottom surface of the C-lobe in the kinase domain. The cross-linking studies from the Gold group also suggests that the D/D domain is proximity to the CNB-B domains(77).

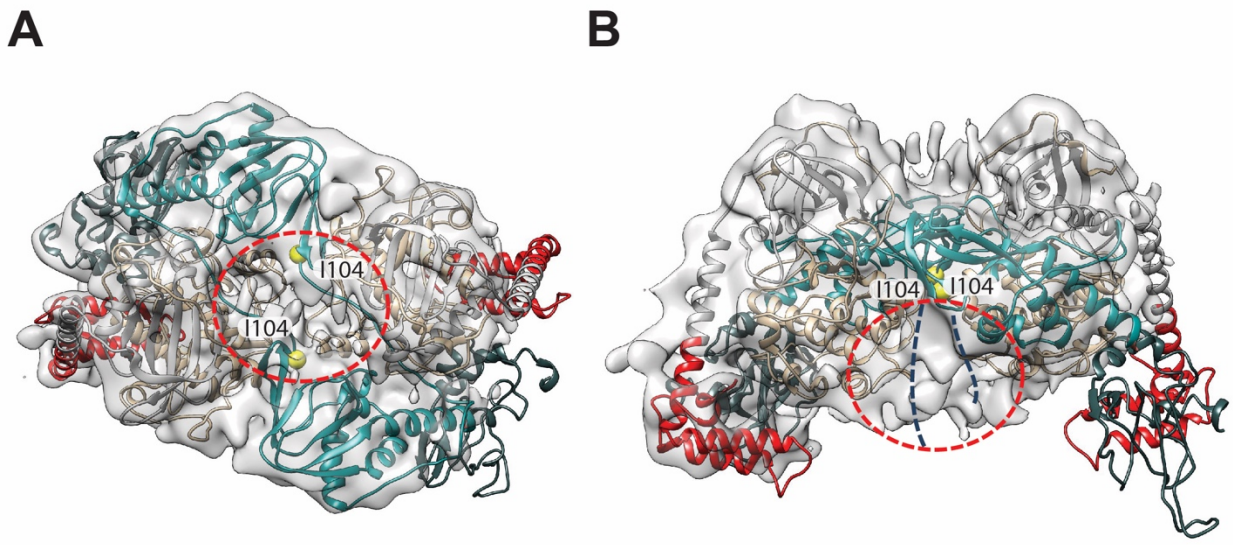

Figure 4-10. The extra density reveals the general position of D/D domain.

4.5 Altered biochemical function of DnaJB1-PKAc in RIIβ holoenzyme

We next asked whether the fusion protein affects not only RIIβ holoenzyme dynamics but also its biochemical properties. Both our MD simulations and our cryo-EM structure suggest that one J-domain moves in a correlated way with its adjacent CNB-B domain and interferes with the overall dynamic properties of the holoenzyme (Figure 4-2D, Figure 4-4 and Figure 4-6), In addition, several studies have shown that the dynamic features of the CNB domains play a significant role in the allosteric activation of the RIα holoenzyme by cAMP (18, 19, 56, 59, 78), and pathogenic mutations in RIα cluster in the two CNB domains(66). We thus compared cAMP activation of the holoenzyme formed with J-C to holoenzyme formed with wt C-subunit.

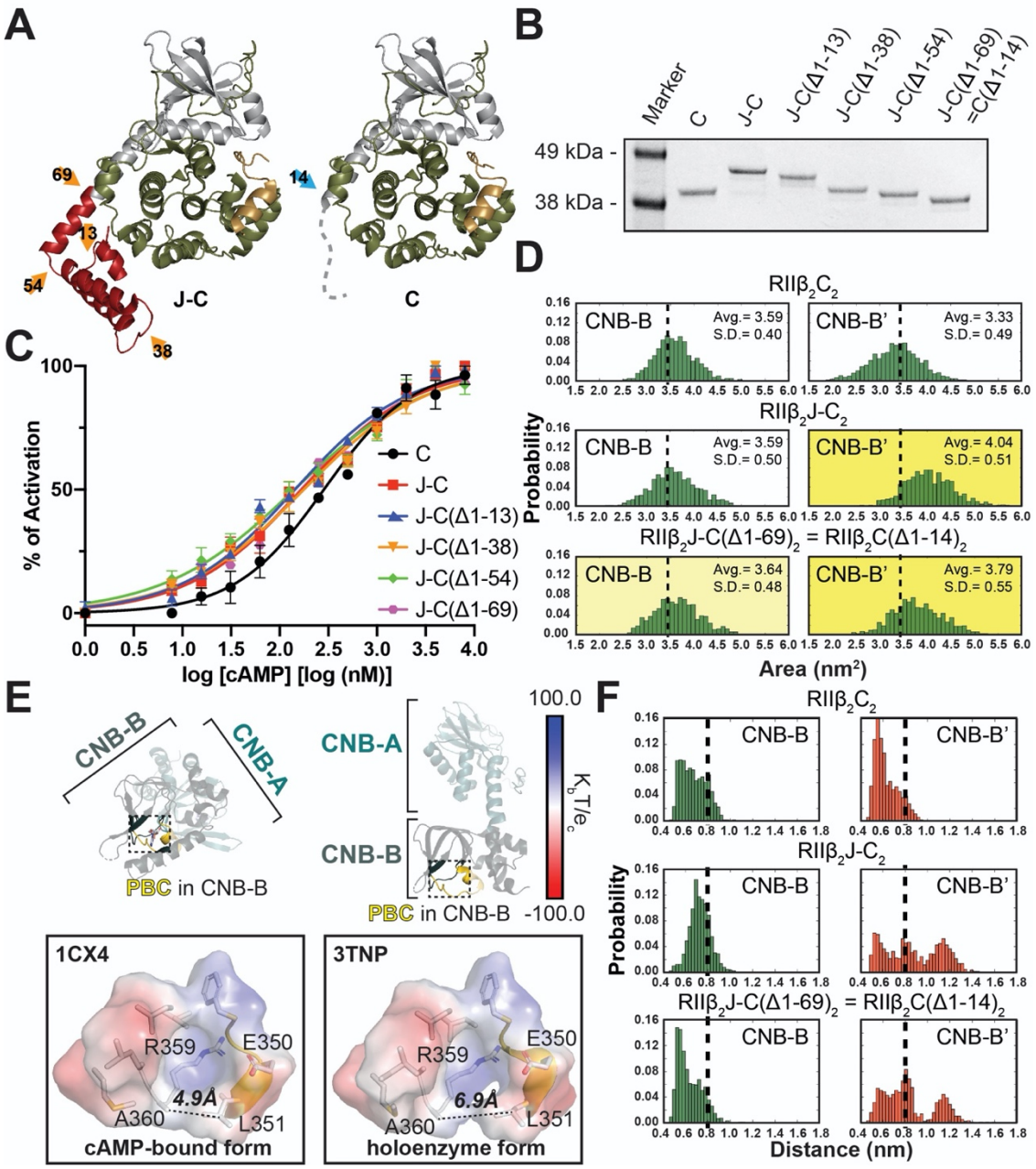

Figure 4-11. The RIIβ2J-C2 holoenzyme is easier to activate with cAMP than the $RII\beta_2C_2$ holoenzyme. (A) Structure of J-C-subunit (left) and C-subunit (right). The junctions of four helices in J-domain are labeled as orange arrows, where the first exon junction is labeled as blue arrow. (B) Coomassie blue staining SDS page of purified C-, J-C-, J-C(Δ1-13)-, J-C(Δ1-38)-, J-C(Δ1-54)-, and J-C(Δ1-69)-subunits. J-C(Δ1-69)-subunit is equivalent to C(Δ1-14)-subunit. (C) The fusion protein $RII\beta_2J\text{-}C_2$ holoenzyme and its deletion mutants were easier to activate with cAMP than the WT $RII\beta_2C_2$ holoenzyme. (D) The CNB-B domains in $RII\beta_2J\text{-}C_2$ and $RII\beta_2J\text{-}C(\Delta1\text{-}69)_2$ holoenzymes have larger cAMP accessible surface area than $RII\beta_2C_2$ holoenzyme. (E) The distance between Cβ atom in $Ala360^{RII\beta}$ and Cγ atom in $Leu351^{RII\beta}$ in the CNB-B domain of cAMP-bound (left, PDB = 1CX4) and holoenzyme forms (right, PDB = 3TNP). (F) The distance population probability of the PBC pocket in $RII\beta_2C_2$, $RII\beta_2J\text{-}C_2$ and $RII\beta_2J\text{-}C(\Delta1\text{-}69)_2$ holoenzymes. The CNB-B domains in the $RII\beta_2J\text{-}C_2$ and $RII\beta_2J\text{-}C(\Delta1\text{-}69)_2$ holoenzymes are more prone to open than the $RII\beta_2C_2$ holoenzyme. Both of the $RII\beta_2J\text{-}C_2$ and $RII\beta_2J\text{-}C(\Delta1\text{-}69)_2$ holoenzymes reveal intrinsic asymmetry in the CNB-B domains.

Holoenzyme formed with the fusion protein was easier to activate than the wt holoenzyme (EC_{50} = 285nM for C-subunit vs. EC_{50} = 170nM for J-C-subunit) (Figure 4-11 and Table 4-3). To investigate the importance of the J-domain in the RIIβ holoenzyme activation by cAMP vs. the absence of the first 14 residues (exon 1), we engineered and expressed several deletion constructs (Figure 4-11A and B). Each of the four extra helices in the J-domain was deleted sequentially, generating J-C(Δ1-13), J-C(Δ1-38), J-C(Δ1-54), and J-C(Δ1-69) deletion mutants (J-C(Δ1-69) is equivalent to C(Δ1-14)). All of these mutants expressed as stable proteins and formed holoenzymes with RIIβ. The deletion mutants were all easier to activate with cAMP, and all showed lower Hill coefficients compared to the wt RIIβ holoenzyme. (Figure 4-11C and Table 4-3). The mutant that simply lacked the first exon, J-C(Δ1-69) or C(Δ1-14), also showed a reduced EC_{50}, indicating that the presence of the first exon (residues 1-14) is crucial for proper activation and allosteric regulation of the RIIβ holoenzyme. Moreover, the Hill coefficient for cAMP activation actually showed negative cooperativity once exon 1 was removed (Table 4-3). Deletion of the first 14 residues in the PKA C-subunit as well as the addition of the J-domain not only changed CNB-B domain dynamics but also affected the finely tuned allosteric activation of the RIIβ holoenzyme by cAMP.

Table 4-3. EC_{50} and Hill coefficient of $RII\beta_2C_2$, $RII\beta_2J\text{-}C_2$ $RII\beta_2J\text{-}C(\Delta 1\text{-}13)_2$, $RII\beta_2J\text{-}C(\Delta 1\text{-}38)_2$, $RII\beta_2J\text{-}C(\Delta 1\text{-}54)_2$, and $RII\beta_2J\text{-}C(\Delta 1\text{-}69)_2$ holoenzymes from cAMP activation curves.

	C	J-C	J-C(Δ1-13)	J-C(Δ1-38)	J-C(Δ1-54)	J-C(Δ1-69)
EC_{50} (nM)	285 ± 54	170 ± 32	144 ± 22	177 ± 31	141 ± 32	166 ± 38
HillSlope	0.949 ± 0.155	0.742 ± 0.091	0.749 ± 0.077	0.690 ± 0.074	0.645 ± 0.085	0.744 ± 0.119

To investigate the correlation between the J-domain and exon 1 of the C-subunit with cAMP activation of the RIIβ holoenzyme, Gaussian accelerated MD simulations (GaMD) on $RII\beta_2C_2$, $RII\beta_2J\text{-}C_2$, and $RII\beta_2J\text{-}C(\Delta 1\text{-}69)_2$ were carried out. Using the radius of cAMP as a probe, we calculated the solvent accessible surface area of the PBC pocket of the CNB-B domains in each of the complexes. Both $RII\beta_2J\text{-}C_2$, and $RII\beta_2J\text{-}C(\Delta 1\text{-}69)_2$ complexes have higher accessible surface area than the wt complex (Figure 4-11D), suggesting that it is easier for cAMP to dock into the PBC pockets, which will facilitate activation. To further analyze the cAMP accessibility in the PBC pocket, we measured the distance between the Cβ atom in $Ala360^{RII\beta}$ and the Cγ atom in $Leu351^{RII\beta}$ (Figure 4-11E). This distance in the RIIβ holoenzyme is 6.9Å, while the PBC pocket is more closed (4.9Å) once it binds cAMP (Figure 4-11E). We then calculated the distance populations in our simulations. Consistent with our solvent accessible surface analysis, both the $RII\beta_2J\text{-}C_2$, and $RII\beta_2J\text{-}C(\Delta 1\text{-}69)_2$ complexes reveal more open states than the wt holoenzyme (Figure 4-11F). In both analyses, there is a noticeable asymmetry between protomers in the cAMP accessibility of the PBC pockets for the $RII\beta_2J\text{-}C(\Delta 1\text{-}69)_2$ and $RII\beta_2J\text{-}C_2$ holoenzymes, supporting our earlier observations of asymmetry. The full-length wt holoenzyme exhibits milder asymmetry, consistence with our hypothesis that the protomers are tightly coupled (Figure 4-11D and F). These results may help to explain why the J-C holoenzyme formed with RIIβ as well as the 1-14 deletion mutant of wt C, is easier to activate with cAMP, while also having reduced cooperativity as measured by the Hill coefficient, compared to the wt RIIβ holoenzyme.

To further explore the effect of exon 1 deletion vs. the J-domain fusion on the αA-helix stability, we analyzed the helical propensity of the αA-helix in three different constructs, wt C-, J-C-, and J-C(Δ1-69)-subunits (Figure 4-12A). The αA-helix in the wt C-subunit, which is part of the N-terminal linker that flanks the N- and C-lobes of the kinase core and is flanked by

intrinsically disorder regions, has a surprisingly high helical propensity. Either deleting exon 1 or fusing with the J-domain decreases the predicted helical propensity (Figure 4-12A). Moreover, the last residue in the exon 1, $Ser14^{C}$, serves as a significant N-capping residue (Figure 4-12B). Decreasing the αA-helix stability and missing the N-capping residue, as demonstrated in our computational and biochemical data, can influence the function and allosteric properties of the entire RIIβ holoenzyme.

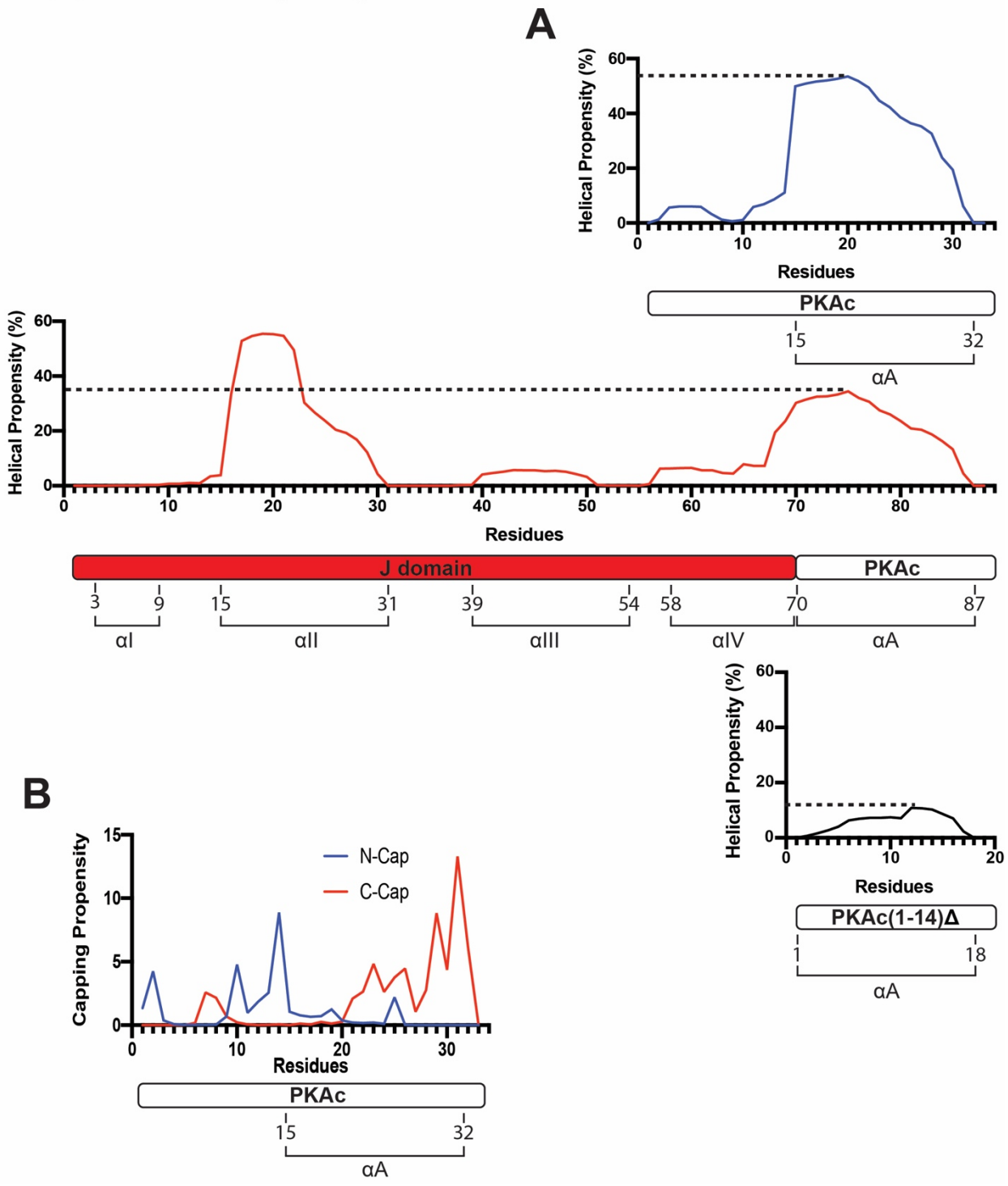

Figure 4-12. Helical propensity (A) and capping residues (B) analyses of αA-helix.

4.6 Discussion

We describe here the structure of the RIIβ$_2$J-C$_2$ holoenzyme solved by cryo-EM single-particle 3D reconstruction. Although the overall 3D organization of the two RIIβ:J-C protomers in the holoenzyme structure is similar to the previous wt RIIβ holoenzyme crystal structure, there are several differences in both the structure and dynamics in the DnaJB1-PKAc RIIβ holoenzyme, which could result in the mis-regulation of PKA signaling. With cryo-EM we are now able to observe more details about the dynamic features of the RIIβ holoenzyme that could not be captured by conventional X-ray crystallography including the general localization of the D/D domain and the asymmetry of the CNB-B domains. Our structure together with MD simulations and biochemical studies not only allows us to better understand how DnaJB1-PKAc disrupts RIIβ holoenzyme function and dynamics, but also makes us appreciate for the first time the intrinsic asymmetry of the RIIβ holoenzyme that is likely an inherent feature of the activation mechanism that was masked in the earlier crystal structure.

4.6.1 Structure and dynamics of wt and DnaJB1-PKAc of RIIβ holoenzyme

The cryo-EM structure and MD simulation data both reveal new and previously unappreciated features of the RIIβ holoenzyme. First is the asymmetry of the RIIβ holoenzyme, which is seen with MD simulations in the wt holoenzyme and captured in the cryo-EM structure but hidden in the previous crystal structure. With MD simulations we observed an intrinsic asymmetry in the wt RIIβ holoenzyme where one protomer has a more flexible CNB-B domain than the other. This same asymmetry is observed in the cryo-EM structure formed with the DnaJB1 fusion C-subunit. The collective results suggest that the activation process most likely initiates from one protomers and then passes to the other. Does it then eventually spread to the entire

holoenzyme or does the intrinsic asymmetry simply involve toggling between the two protomers without resulting in full dissociation of the C-subunits? Is the asymmetric feature an intrinsic part of the activation mechanism? How does the activation signal pass from one protomer to the other? These are major future challenges.

Second are the correlated motions of the CNB-B domain with the J-Domain, which is revealed in the cryo-EM structure. As seen in previous structures, the J-domain is very flexible (63, 71), however, in the RIIβ holoenzyme we see that the flexibility of the J-domain is correlated with its adjacent CNB-B domain as well as with the αA-helix that it is fused to. The J-domain can also further influence the dynamic features of the CNB-B domains in the RIIβ holoenzyme, which we did not see in the RIα holoenzyme. Several studies have demonstrated that the dynamic features of the CNB domains in RIα are essential for PKA activation and allostery(56, 58, 59, 79). Here, for the first time, we are able to show that the RIIβ holoenzyme also has flexible CNB-B domains, although it is different from RIα in terms of its structure and allosteric regulation(52, 62, 80).

In summary, we show here that J-domain can influence the dynamic properties and the symmetry of the CNB-B domains. Our MD simulation data clearly indicated that the J-domain can stabilize the CNB-B domains, while the cryo-EM structure revealed how the J-domain and the CNB-B domain interact and together control the αA-helix. We believe that this effect can be significant for stability, activation, cAMP binding and/or interaction with other binding partners.

4.6.2 D/D domain, myristylation site and AKAP binding

Cryo-EM, confirmed by SAXS, also allowed us to localize the general position of the D/D domain. The D/D domain is essential for PKA localization. PKA holoenzymes, especially RII holoenzymes, typically bind with high affinity to an amphipathic helix that is embedded in scaffold proteins referred to as A-Kinase-Anchoring Proteins (AKAPs) through their D/D domains(11, 12,

81). In this way, AKAPs bring the PKA holoenzyme to specific locations in the cell where it is in close proximity to dedicated substrates such as receptors, transporters and ion channels(5, 82). and several lines of evidence have demonstrated that disrupting this interaction can affect not only PKA localization but also substrate specificity (14, 82-86).

Our results show that the linker joining the D/D domain and the inhibitor site in RIIβ weaves through the hole that is created by the two RIIβ:J-C protomers. This placement of the D/D domain is also consistent with cross-linking studies and different from the RIIα holoenzyme(77, 87). It is also consistent with our linker swap experiments showing that the motif that is responsible for the compact structure of the RIIβ holoenzyme is embedded in this linker and D/D domain region(88). This model places the D/D domain and the myristylation sites attached to the N-termini of the C-subunits on the same surface, which allows them to form multivalent interactions with membranes (Fig. 6A). The myristyl groups in the RIIβ holoenzyme are solvent exposed and can anchor to membranes even in the absence of AKAPs(85, 89), whereas the myristyl groups in the RIα holoenzyme are embedded in the acyl pocket in the C-lobe of the C-subunit and do not contribute to membrane anchoring (89). In contrast to RIα holoenzymes, most of the RII subunits are localized close to membranes(5). Therefore, having the D/D domain in the RIIβ holoenzyme localized on the same face as the myristylation sites provides a dual mechanism for forming multivalent interactions with the membrane. It is also likely that anchoring the N-terminus to membranes could influence the conformation of the missing 14 residues. This segment with its basic residues followed by a phosphorylation site is in fact a classic myristylation motif, similar to Src kinase, where the basic residues also contribute to membrane anchoring(90). As we show here, ordering the first 14 residues in the membrane-bound holoenzyme could easily affect the dynamic behavior of the entire wt holoenzyme. The hydrophobic C-terminus of the RIIβ-subunit, as well

as its dynamic β4-β5 loop in the CNB-B domain, could also become ordered when the holoenzyme is anchored to membranes. The highly basic β4-β5 loop in RIIβ is, in particular, in close proximity to the acidic surface of the membrane (Figure 4-13A). In addition, AKAPs themselves typically have a membrane-targeting-motif (MTM), so many mechanisms could be used to stabilize interactions with membranes (Figure 4-13A). In the J-C fusion protein, the myristylation site is lost which could also affect RIIβ holoenzyme binding to membranes in the cells (Figure 4-13A).

4.6.3 Two helices drive the allosteric regulation of the PKA holoenzymes

There are two helices that drive the allosteric regulation of PKA, the αB/C/N-helix in the R-subunits and the αA-helix in the C-subunit (Figure 4-13B). Sequences difference in the αB/C/N-helix, as well as differences in helical propensity and dynamics, between RI and RII reveal distinct allosteric networks between the two PKA isoforms, and the hinge point position in the αB/C/N-helix can also clearly contribute in unique ways to this allosteric communication. Our results indicate not only that the location of the major hinge point in the cAMP-bound conformation is significant, but also suggests that the αB/C/N-helix dynamics and the activation processes are probably linked.

While the dynamic αB/C/N-helix of each R-subunit is a dominant feature for cAMP-mediated activation of each holoenzyme, the stable αA-helix is a dominant allosteric feature of the C-subunit. The αA-helix is embedded in the N-terminal tail (N-tail) (residues 1-39) that wraps around both lobes of the kinase core (Figure 4-13B). This N-tail that precedes the kinase core and is missing entirely in our cryo-EM structure, is a key allosteric regulatory element(13). Of particular importance is the hydrophobic motif ($Trp30^{C}$ and $Phe26^{C}$ or $Trp85^{J\text{-}C}$ and $Phe81^{J\text{-}C}$) at

the end of αA-helix, which in the wt C-subunit, is wedged between the αC-helix and the Activation Loop of the kinase core (Figure 4-13B)(13).

The importance of exon 1 and the αA-helix in the PKA C-subunit has been demonstrated both biochemically and computationally(91, 92). Biochemically, we show that the deletion of residues 1-14 (exon 1) in wt C-subunit can introduce instability and can also affect holoenzyme function(91). Our previous study also indicated that the J-C-subunit is less thermostable than WT C-subunit(63, 71). Several post-translational modification sites in the wt C-subunit are localized at the other end of the αA-helix in exon 1, and these are missing in the fusion protein. These include the myristylation site at $Gly1^{C}$, the phosphorylation at $Ser10^{C}$, and deamidation at $Asn2^{C}$ and all are thought to contribute to function(93-95). How these residues are ordered when the acyl group is anchored to a membrane and how this influences the structure and function of the holoenzyme remains to be elucidated. Computationally, the community map analysis based on MD simulations shows that the DFG motif, which is crucial for kinase activity, is in the same community with the αA-helix(92). This community also connects to other substrate binding motifs, indicating these motifs are allosterically coupled(92). It is clear that the αA-helix can regulate many other motifs in both the C- and R-subunits, so that destabilizing the αA-helix could have a major effect on holoenzyme function.

4.6.4 Visualizing allostery

By capturing full length PKA holoenzymes in a crystal lattice we are able to visualize the striking symmetry of PKA as well as the allosteric cross talk between the two protomers, which is an essential feature of PKA activation(20, 22, 63, 73). However, any differences in dynamics are masked in these holoenzyme crystal structures; they are simply averaged. We show here that the asymmetry, although hidden in the RIIβ crystal structure, can be seen with MD simulations and in

the cryo-EM structure. In the crystal structure there is simply a high temperature factor for the CNB-B domains and the αA-helix, but the asymmetry, which must be an integral part of the allosteric mechanism for activation, is hidden. MD simulations allowed us to delve more deeply into the intrinsic asymmetry that is embedded in the dynamic properties of each CNB domain. This loss of allosteric communication between the two protomers is also reflected in the reduced Hill coefficient for cAMP activation. With single-particle cryo-EM reconstruction, however, we can directly observe the asymmetry of the two protomers. The combination of crystallography, MD simulations, and cryo-EM is thus a powerful way to explore thee different states; one approach alone is not sufficient.

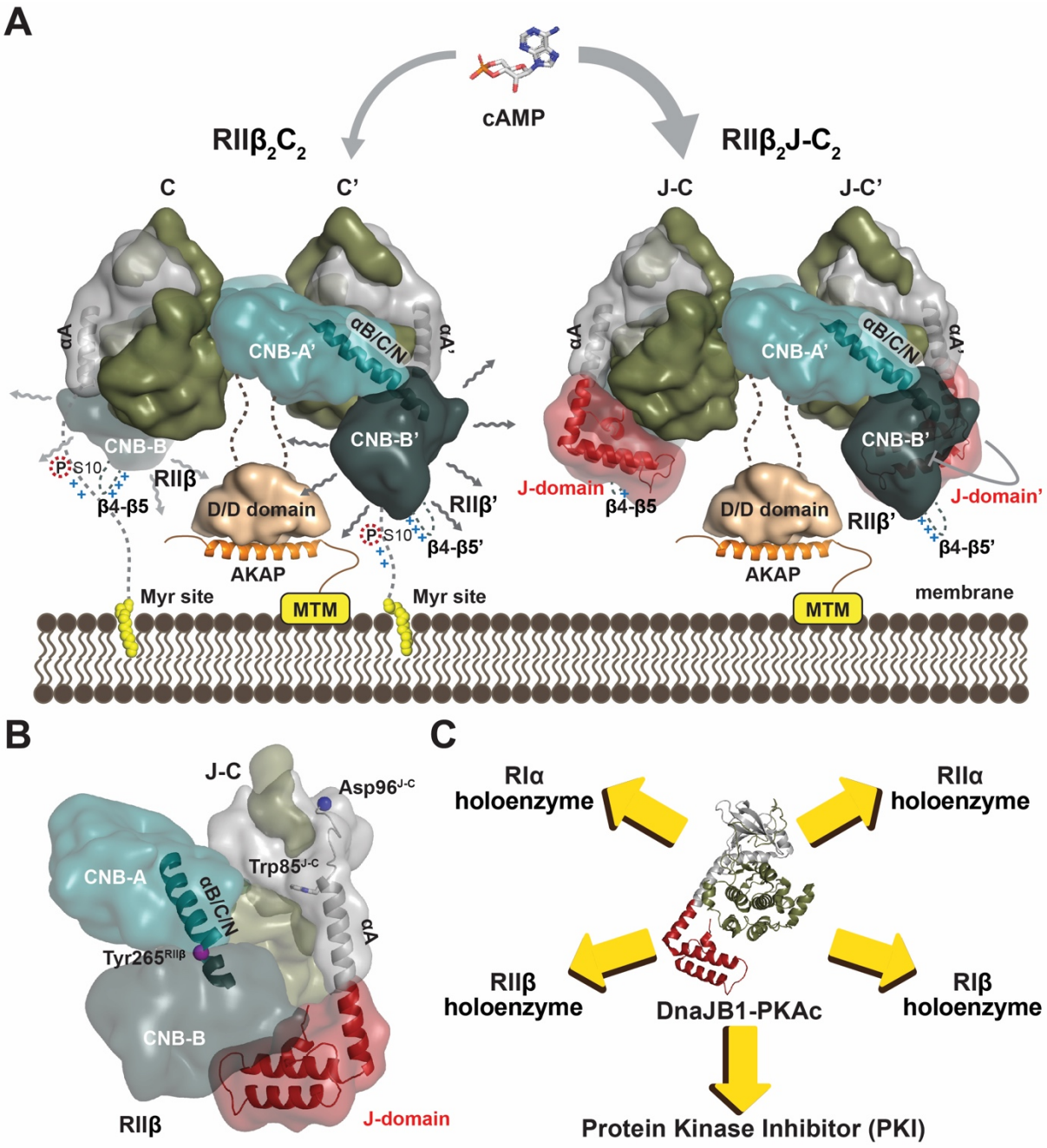

Figure 4-13. The structural, dynamic, and allosteric features of RIIβ$_2$J-C$_2$ holoenzymes. (A) The J-domain disrupts the multi-valent interaction and it can also stabilize the CNB-B domain dynamic in RIIβ holoenzyme. Meanwhile, RIIβ$_2$J-C$_2$ holoenzyme is easier to be activated by cAMP than RIIβ$_2$C$_2$ holoenzyme. (B) Two helices, αB/C/N-helix and αA-helix, regulate the RIIβ holoenzyme allostery. (C) DnaJB1-PKAc impairs PKA signaling network in an isoform-specific manner.

4.6.5 DnaJB1-PKAc disrupts PKA function in an isoform-specific manner

PKA-dependent signaling is finely regulated, which is demonstrated best in RIα where there are many mutations that are mostly clustered in the two CNB domains(66). Those in the CNB-A domain, for example, lead to Carney Complex Disease and create holoenzymes that are easier to activate with cAMP while those in the CNB-B domain lead to *Acrodysostosis* and are more difficult to activate(66). The differences are not off/on, but simply reflect a slightly different balance which is sufficient to cause distinct disease phenotypes.

Although the DnaJB1-PKAc fusion protein is the driver of FL-HCC, our structures of the RIα holoenzyme and the RIIβ holoenzyme with J-C-subunit do not reveal a clear mechanism for the pathogenesis of the mutation, instead we showed that the regulation of each holoenzyme is disrupted. The RIIβ holoenzyme formed with the fusion protein is easier to activate with cAMP than wt holoenzyme. This is in contrast to RIα where the PKAc and DnaJB1-PKAc RIα holoenzymes show similar cAMP activation(63); however, DnaJB1-PKAc can disrupt RIα localization and cAMP signaling compartmentation(96). Each of these PKA signaling networks is highly regulated and perturbation of that fine tuning can have profound consequences. In contrast to mutations in the R-subunits, the results of a mutation or fusion in the C-subunit will be complex and multi-valent and EVERY holoenzyme will be affected as well as interactions with PKI (FFigure 4-13C)(97). In the liver where regulation of metabolism is linked so closely to PKA-mediated gene transcription the effects of this mutation will be complex. Based on our work here coupled with previous studies of the PKI complex and the RIα holoenzyme it is clear that the fine tuning and allosteric regulation of each complex will be altered as well as the expression levels of each PKA regulatory subunit; the entire PKA signaling network will be disrupted.

4.7 Acknowledgment

Chapter 4 is currently submitted as a manuscript by Lu, T.-W.; Aoto, P. C; Weng, J.-H.; Nielsen, C.; Cash, J. N.; Hall, J.; Zhang, P.; Simon, M. S.; Cianfrocco, M. A.; Taylor, S. S. "Capturing allostery: asymmetry and dynamics of PKA RIIβ holoenzyme with DnaJB1-PKAc fusion in fibrolamellar hepatoceullar carcinoma" The dissertation author is the primary author of this manuscript.

Chapter 5 PKA isoform-specific localization and function in cells

In the previous chapters, I have shown that each of the PKA isoform has distinct quaternary holoenzyme structure as well as their allostery. In RIα holoenzyme, ATP serves as an orthosteric inhibitor, whereas in RIIβ holoenzyme, ATP is simply a substrate and can facilitate the PKA activation(73). Meanwhile, I have also shown that the cancer driving fusion mutant, DnaJB1-PKAc, can disrupts the PKA-dependent functions and dynamics in an isoform-specific way(63).

In this chapter, I would like to discuss the PKA localizations and functions in the cells. Utilizing the CRISPR-Cas9 techniques, I am able to generate the knock-out cell lines for each of the R-subunit. The R-subunit knock-out cell lines are great models to dissect the isoform-specific PKA-dependent signaling pathway in cells. I also study the localization of each isoform of PKA holoenzyme endogenously and in overexpression levels. I also showed here in this chapter that how the fusion protein, DnaJB1-PKAc, disrupts the PKA holoenzyme localization and potentially leads tumorigenesis. I also further generate RIα/RIβ and RIIα/RIIβ double knock-out cell lines. We showed that the ATP has distinct effect on RI and RII subunits; ATP stabilizes RI holoenzyme, therefore PKA activity is decreased when ATP concentration increased, whereas ATP destabilizes RII holoenzyme, increasing ATP concentration leads to PKA activity elevated. Our data is consistent with our *in vitro* studies that I have shown in Chapter 2. These results reveal that the distinct functions of PKA isoforms.

5.1 PKA R-subunits CRISPR-Cas9 knock-out cells

Recent advances of CRISPR-Cas9 techniques allows us to target and knock-out specific gene in the organisms and the cells. The protein Cas9 (CRISPR associated protein 9), derived from *Streptococcus pyogenes*, can unwind the double helix DNA and form Cas9-gRNA-DNA complex with 20 base pairs guide RNA (gRNA) and its complementary DNA sequences (98). The Cas9 cleaves the NGG site of the DNA and induces double strand breaks. These breaks can be utilized to introduce site-directed mutations by homologous recombination mechanism or simply knock-out through non-homologous end-joining(99). The high specificity and efficient properties make Cas9 a prominent tool for the gene editing studies(100, 101).

To generate four different PKA R-subunits knock-out cells, I first designed the 20 base pairs gRNA that specifically target to early exons of human PKA R-subunits. For each of the R-subunit, two gRNAs have been chosen to knock-out any of the potential splicing isoforms. After transfection and single-cell sorting, each of the clone was validated by genomic PCR and western blots (Figure 5-1).

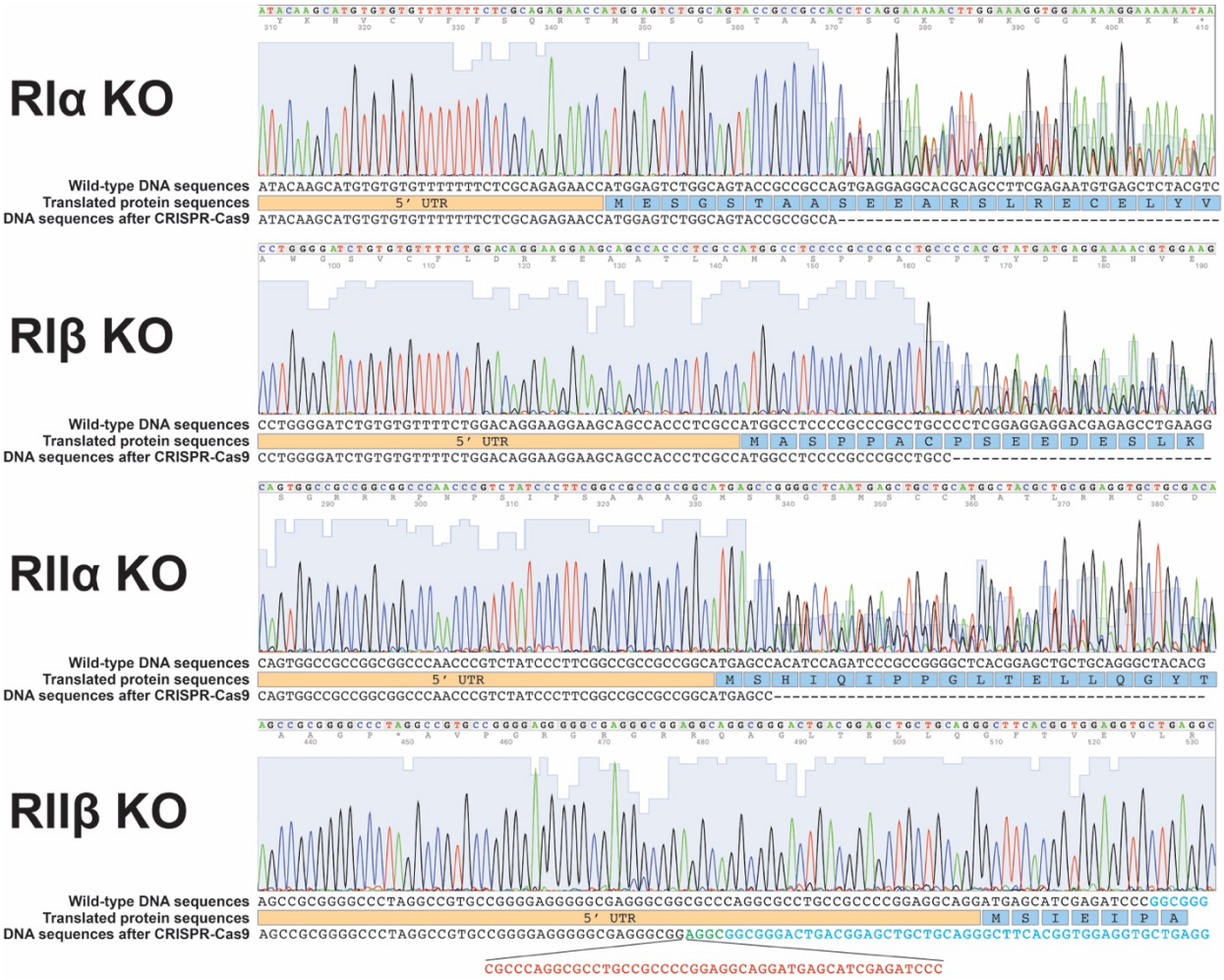

Figure 5-1. Genomic sequencing of R-subunit knock-out cells

5.2 Localization of PKA C- and J-C subunit

To study the localization of C-subunit, we expressed the C-terminus mCherry-fused C-subunit itself. By co-expressing with different markers, we identified wt C-subunit can either goes to mitochondria, Golgi apparatus, or centriole (Figure 5-2). Several studies have shown that PKA's role in different cellular compartment. For example, PKA can regulate the mitochondrial fission and fusion as well as Cytochrome *c* Oxidase (COX) complex in electron transport chain(102-104). Golgi complex's structure and biogenesis is also associated with PKA activity (105). Centrin, a main component of centrosome, can be phosphorylated by PKA. The stimulation of centrin phosphorylation by PKA results in centriole separation in interphase (106).

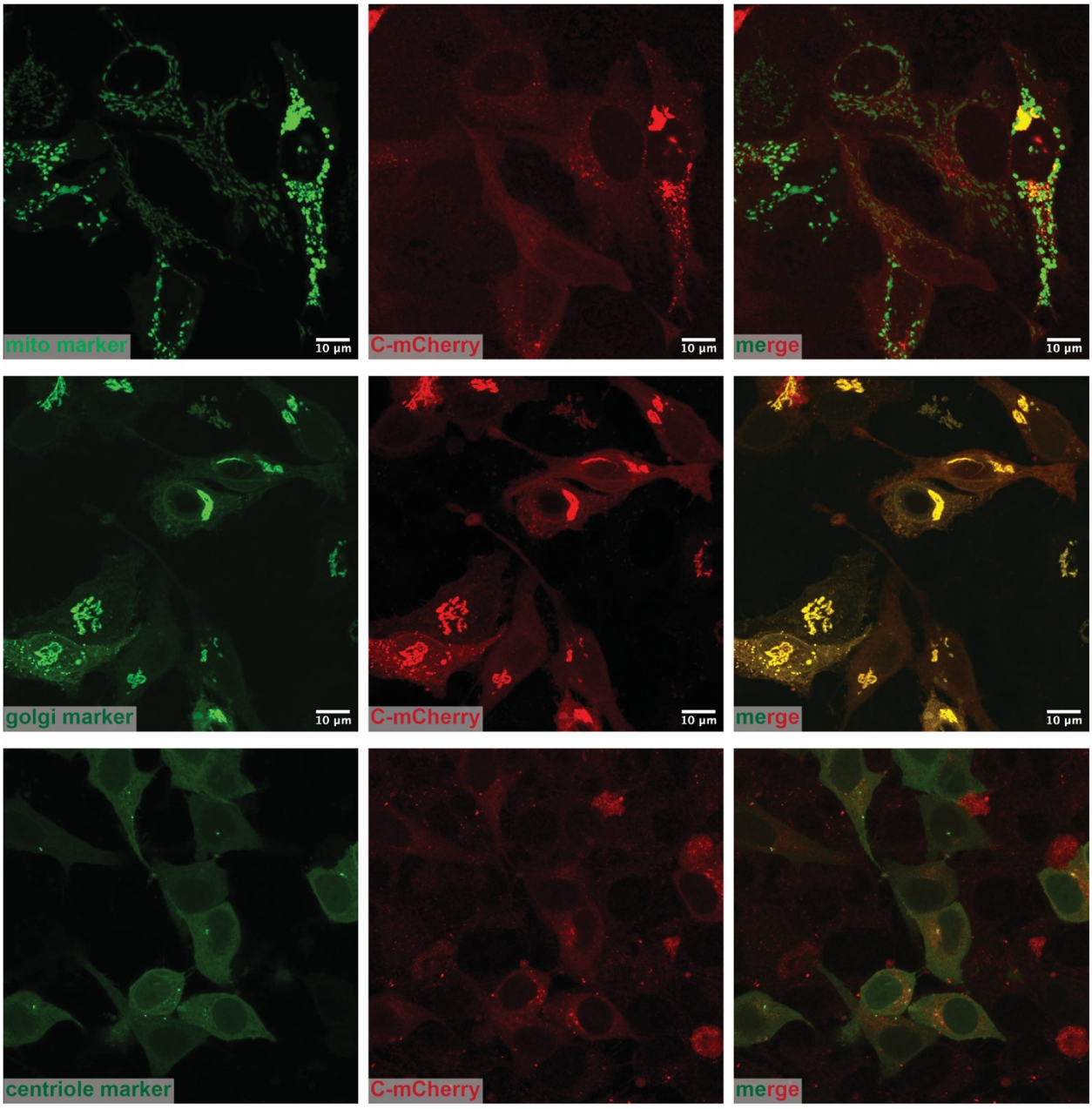

Figure 5-2. Wild-type C-subunit co-localizes with mitochondria, Golgi, and centriole markers.

Whereas, expressing C-terminus mCherry-fused J-C-subunit itself shows different result (Figure 5-3). Co-expressing with mitochondria, Golgi apparatus, or centriole markers have distinct localization pattern comparing with wt C-subunit. J-C-subunit can still go to centriole (Figure 5-4); however, it mainly diffuses in the cells and neither goes to Golgi apparatus or mitochondria.

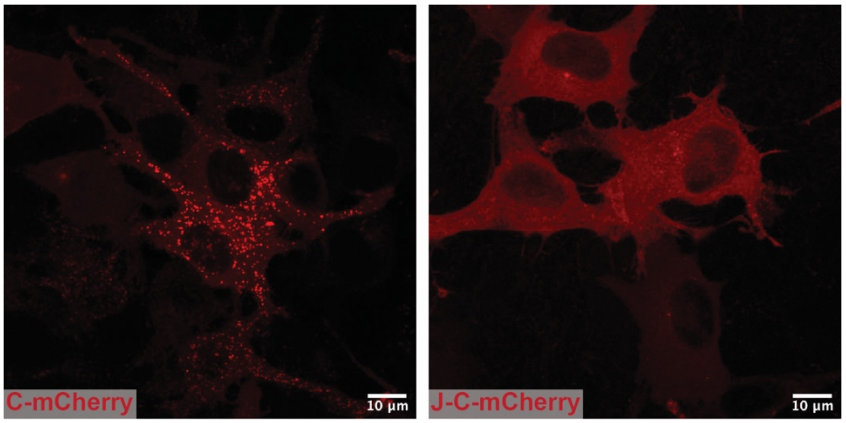

Figure 5-3. Wild-type C-subunit and J-C-subunit have distinct localization.

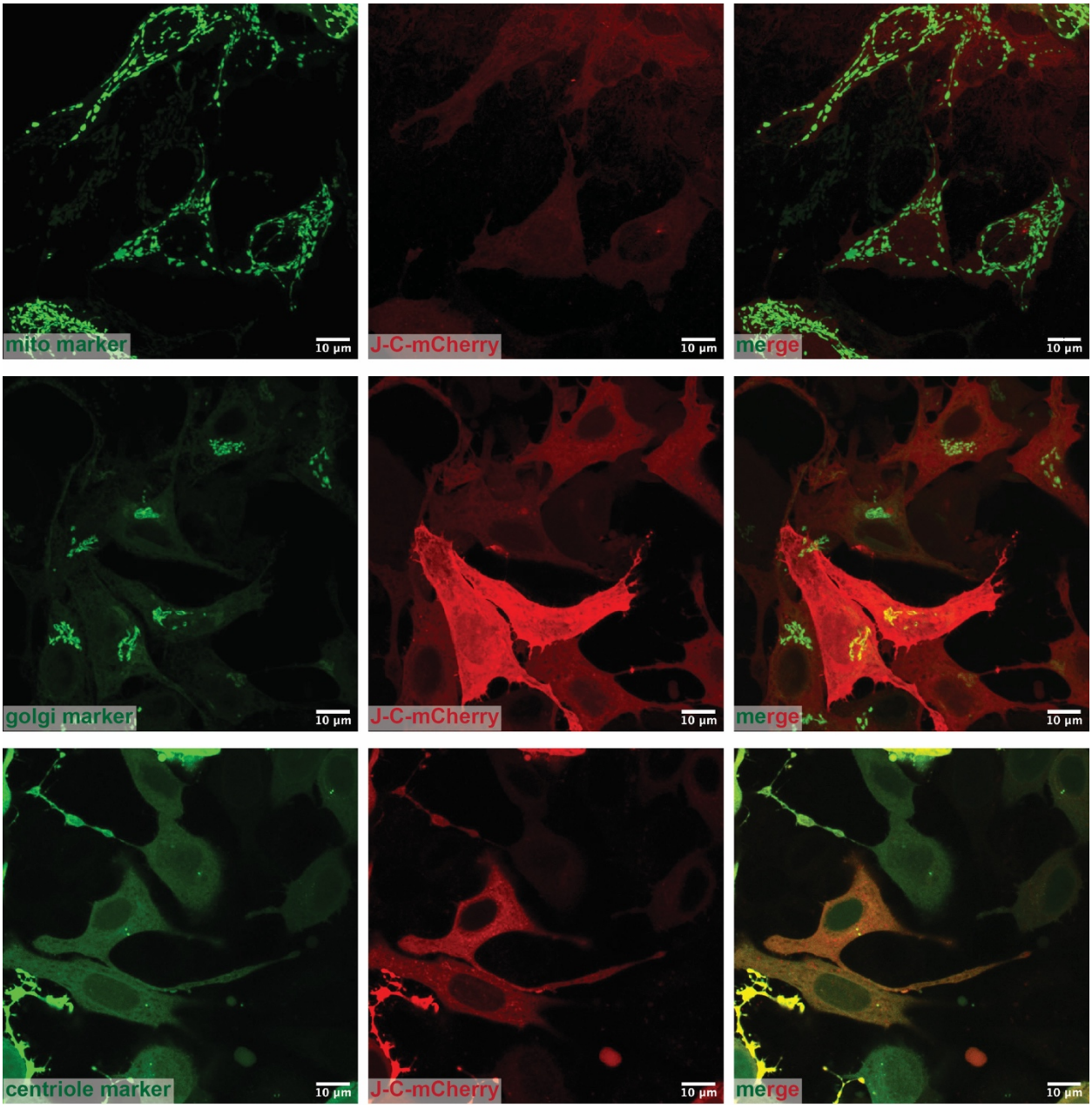

Figure 5-4. The J-C-subunit co-localizes with centriole marker, but not with mitochondria or Golgi markers.

5.3 Localization of RIα holoenzyme

Next, to study the localization of RIα holoenzyme, the C-terminus mCherry-fused C-subunit together with the C-terminus eGFP-fused RIα in the HEK293T cells. The $RI\alpha_2C_2$ and $RI\alpha_2J\text{-}C_2$ holoenzyme reveals different localization patterns (Figure 5-5).

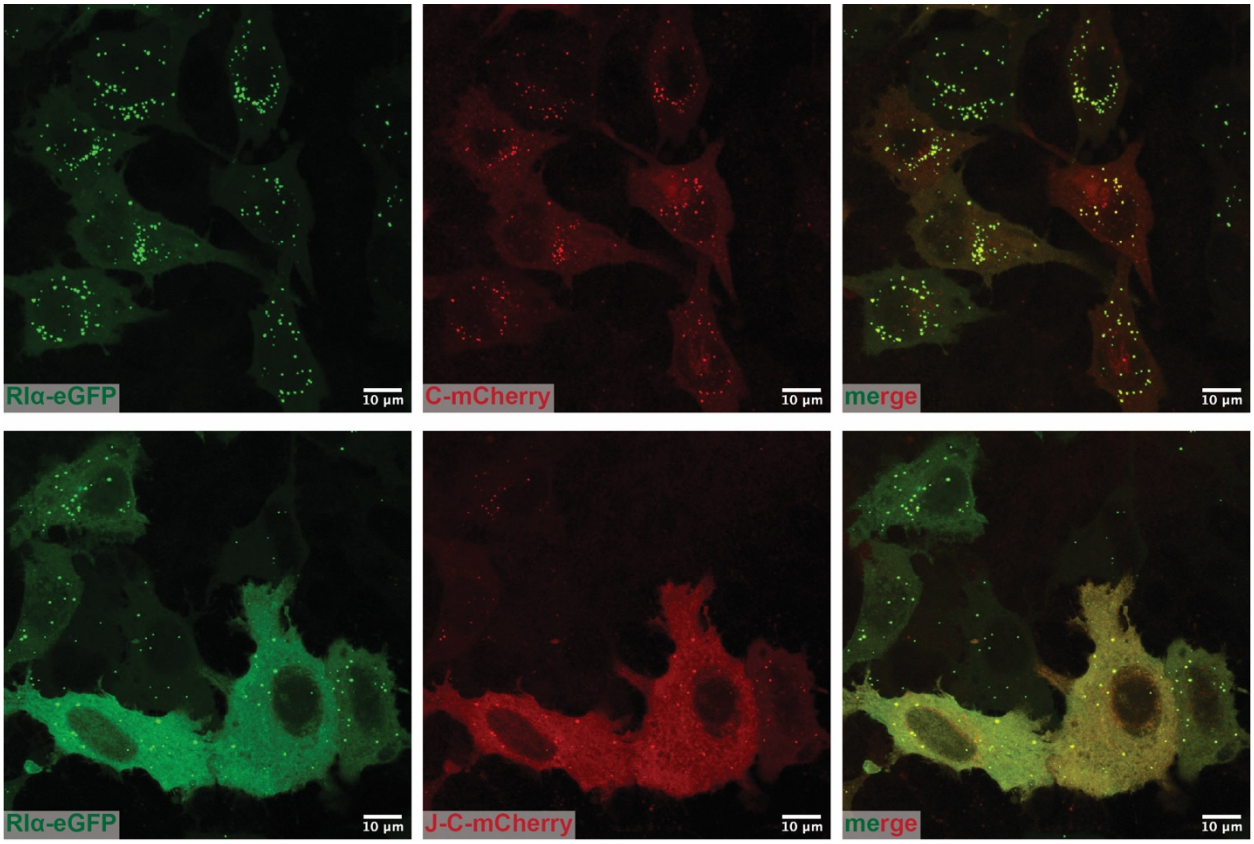

Figure 5-5. The $RI\alpha_2C_2$ (top) and $RI\alpha_2J\text{-}C_2$ (bottom) holoenzymes have different localization patterns.

For the wt RIα holoenzyme, the puncta-like structures have been identified as phase separation bodies, which was also shown to regulate the cAMP compartmentation in cells(96). However, the $RI\alpha_2J\text{-}C_2$ holoenzyme has distinct localization; it is diffused in the cells. Therefore, we would like to examine the molecular mechanism of the $RI\alpha_2J\text{-}C_2$ holoenzyme mis-localization. Several J-domain deletion mutants (J-C(Δ1-13), J-C(Δ1-39), and J-C(Δ1-55)) were expressed with the RIα-eGFP construct to examine their RIα holoenzymes localizations. Similar to the $RI\alpha_2J\text{-}C_2$ holoenzyme, all of them are diffused in cells (Figure 5-6). These results indicate that the mis-localization of the $RI\alpha_2J\text{-}C_2$ holoenzyme is not due to the steric effect of the J-domain.

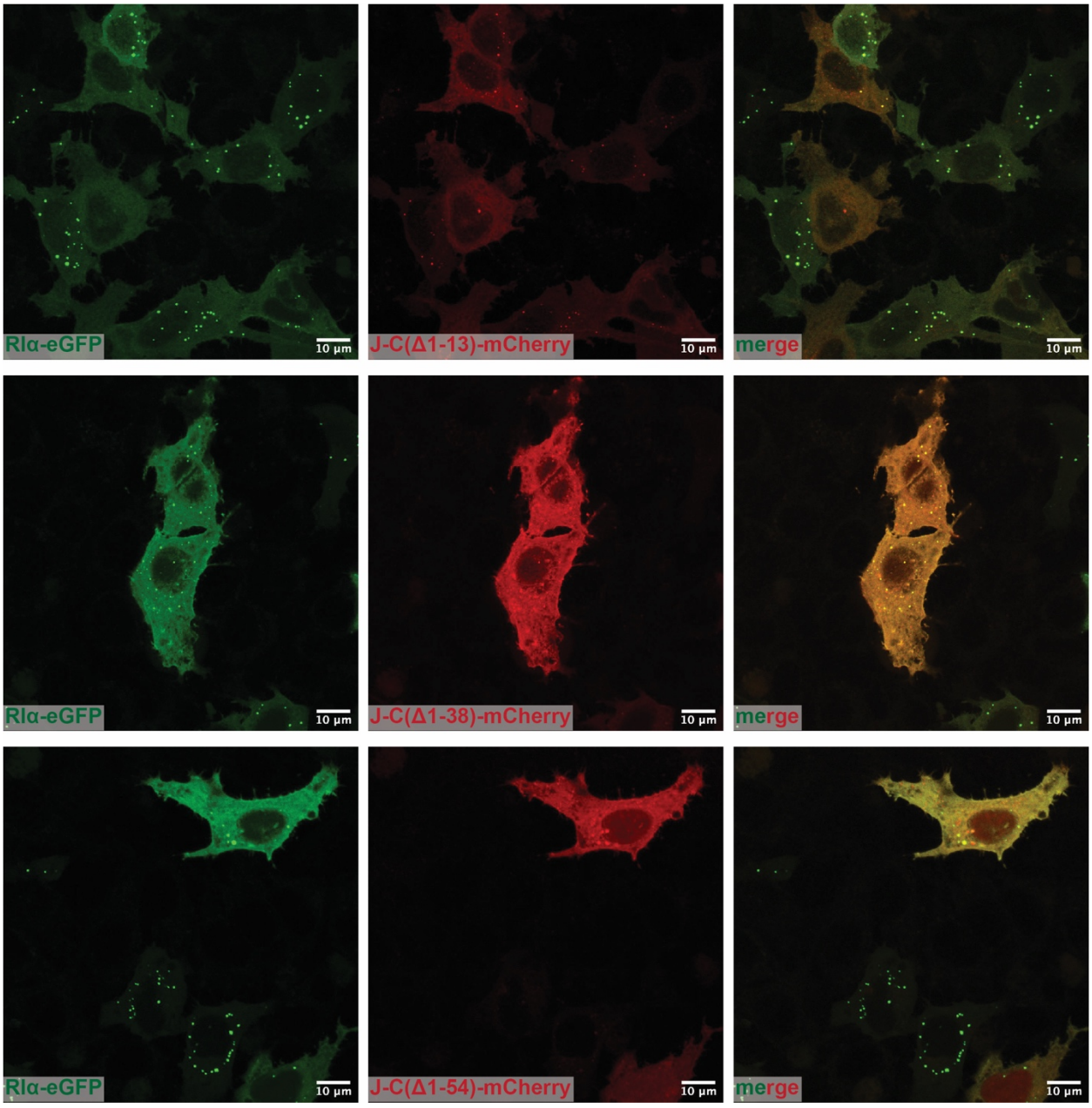

Figure 5-6. Co-expression of deletion mutants of J-C-subunits with RIα-subunit have similar localization as $RI\alpha_2J\text{-}C_2$ holoenzyme.

Next, we wanted to examine if the myristylation site can affect the RIα holoenzyme localization. We thus co-expressed the wt RIα-subunit with G1A mutation of C-subunit, which has been shown to abolish the PKA C-subunit myristylation (Figure 5-7). This mutant holoenzyme is diffused in the cells. Our results show that missing the myristylation sites apparently can affect the phase separation body formation.

We also found that the D/D domain mutations (RIα V20A/I25A), which retain the D/D domain integrity but can abolish AKAP binding (83), reveal similar localization as the $RI\alpha_2$J-C_2 holoenzyme (Figure 5-7). This may indicate that AKAP participates the phase separation body formation and the J-domain can impede AKAP binding in the cells.

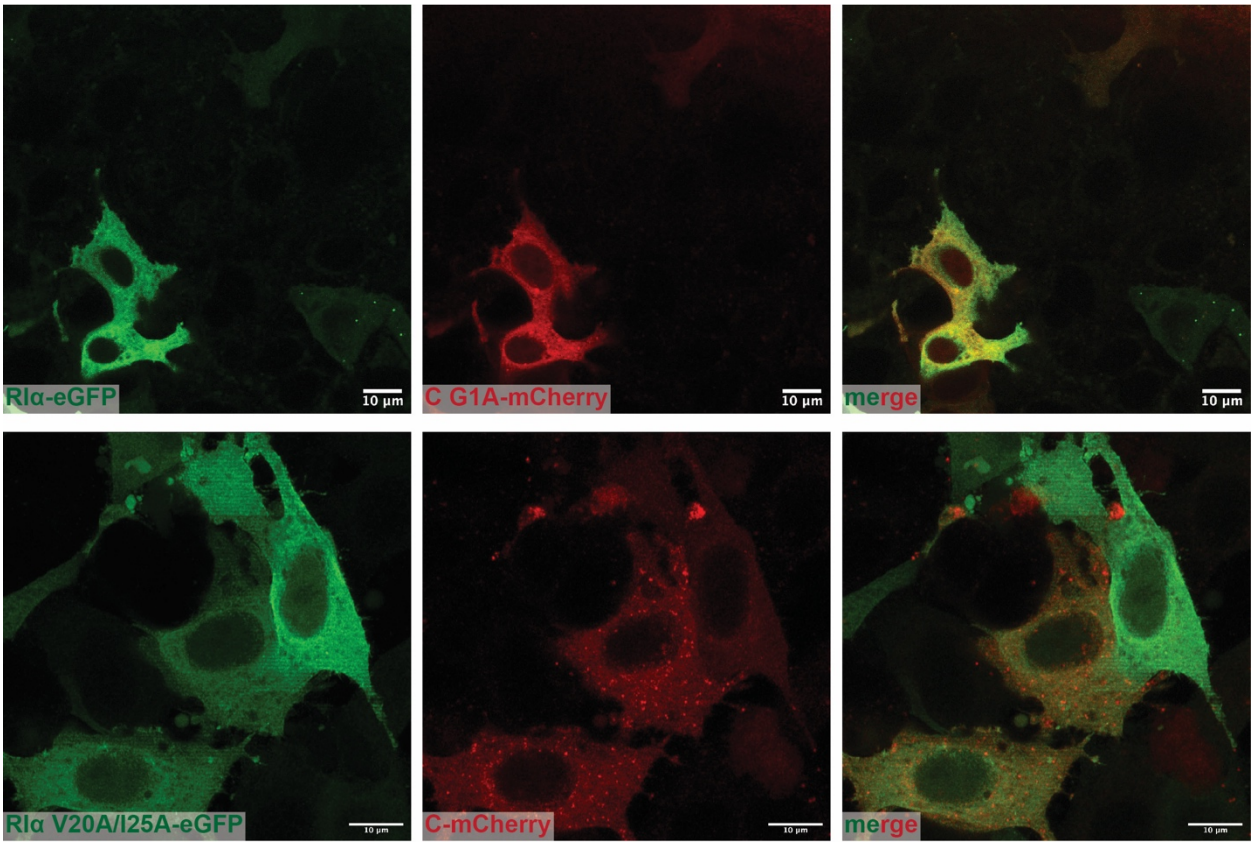

Figure 5-7. Myristylation site or D/D domain mutations can disrupt phase separation body formation.

We can conclude that both the myristylation site in the C-subunit and the D/D domain in the RIα-subunit are crucial for phase separation body formation. The extra J-domain and the missing myristylation site in the fusion protein impairs the PKA RIα pathway. The mis-localization of the $RI\alpha_2J\text{-}C_2$ holoenzyme also contributed to tumorigenesis.

5.4 Localization of RIIβ holoenzymes

To study the localization of $RII\beta_2C_2$ holoenzyme, we co-expressed the C-terminus eGFP-fused RIIβ and C-terminus mCherry-fused C-subunit in the HEK293T cells. Unlike $RI\alpha_2C_2$ holoenzyme, both RIIβ-eGFP and C-mCherry reveals patterns next to the nucleus region, indicating that $RII\beta_2C_2$ holoenzyme localizes at the Golgi apparatus (Figure 5-8).

The same constructs but replacing the wt C-subunit with the J-C-subunit was used to study the localization of $RII\beta_2J\text{-}C_2$. We co-expressed the C-terminus eGFP-fused RIIβ and C-terminus mCherry-fused J-C-subunit in the HEK293T cells. The $RII\beta_2J\text{-}C_2$ holoenzyme shows the same pattern as $RII\beta_2C_2$ holoenzyme, indicating the J-C-subunit does not change RIIβ holoenzyme localization. The $RII\beta_2J\text{-}C_2$ holoenzyme can still localizes to the Golgi apparatus (Figure 5-8).

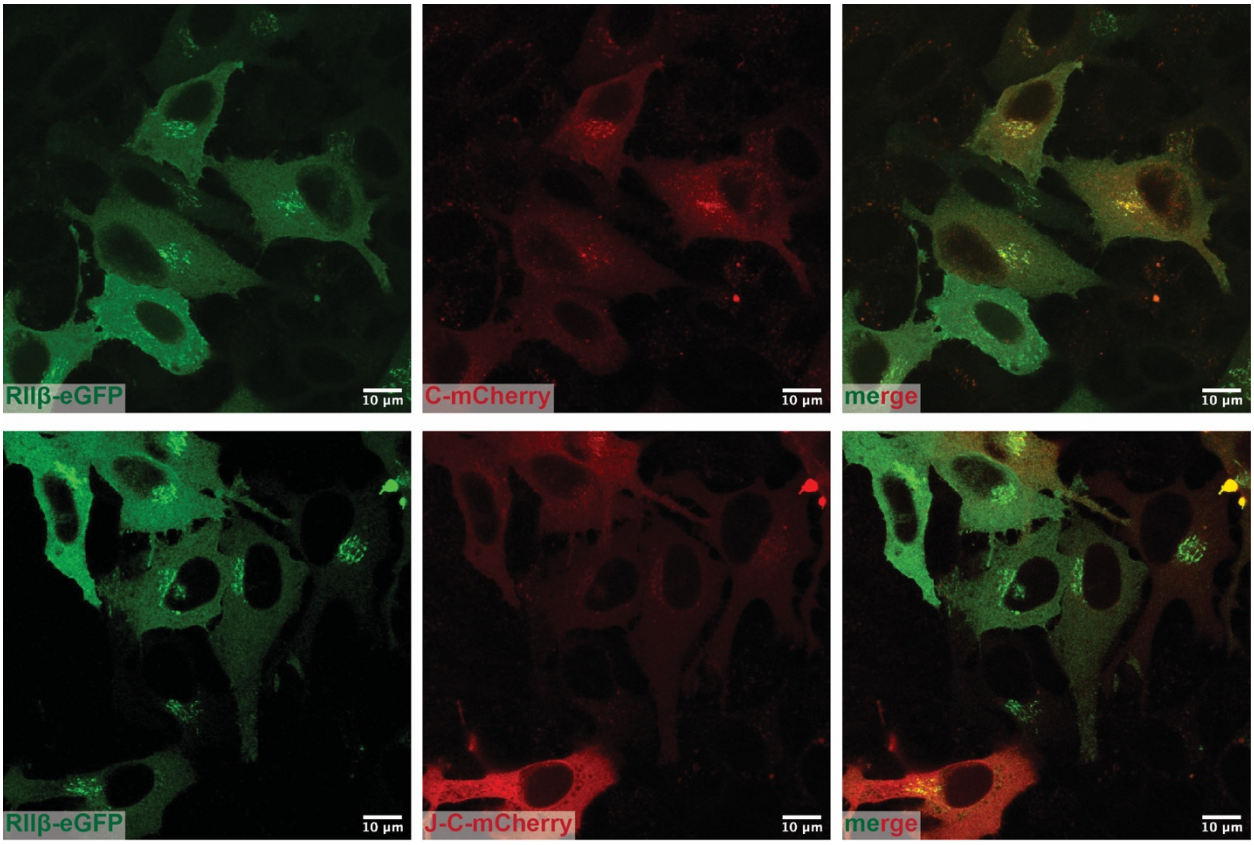

Figure 5-8. Both RIIβ$_2$C$_2$ and RIIβ$_2$J-C$_2$ holoenzymes localize in Golgi apparatus.

5.5 RIα/RIβ and RIIα/RIIβ double knock-out cells

In the previous chapters, we used RIα and RIIβ holoenzymes as examples to show their different responses toward ATP *in vitro*. The inhibitory sequence in RIα is a pseudo-substrate, therefore ATP serves as an orthosteric inhibitor, ATP stabilize RIα holoenzyme and make it more resistant to cAMP(73). In constrast, the inhibitory sequence in RIIβ is a substrate, it can be phosphorylated when ATP is present. The phosphorylated form of RIIβ is easier to active with cAMP(73). The pseudo-substrate or substrate in the inhibitory sequence of R-subunit is the signature feature that distinguishes RI and RII, respectively.

Therefore, we generated the RIα/RIβ and RIIα/RIIβ double knock-out cells in order to study the effect of ATP on PKA R-subunit isoforms (Figure 5-9). To make the RIα/RIβ and RIIα/RIIβ double knock-out cells, the RIα and RIIα knock-out HEK293T cells were transfected with gRNAs that target to RIβ or RIIβ, respectively. After transfection and single-cell sorting, each of the clone was validated by genomic PCR and western blots.

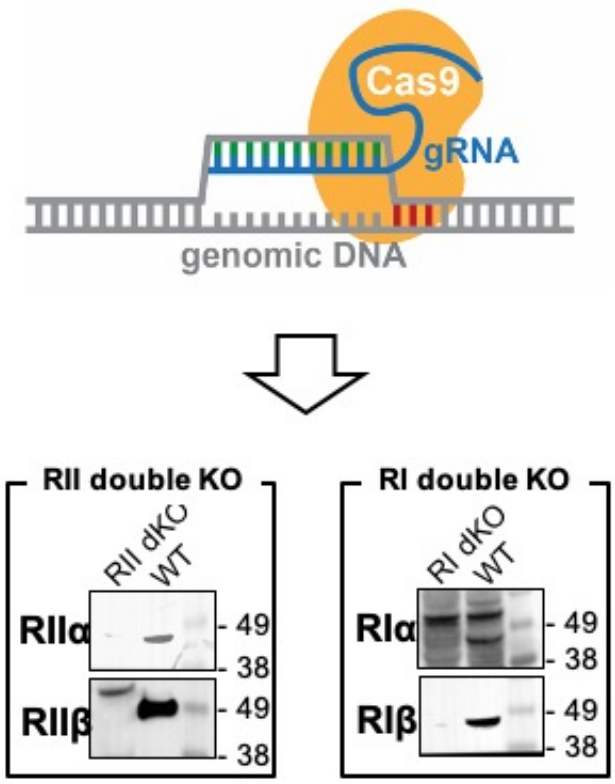

Figure 5-9. Generating RIα/RIβ and RIIα/RIIβ double knock-out cells.

We then utilized a PKA activity FRET reporter to investigate the activity differences under different of stimulations in the RIα/RIβ and RIIα/RIIβ double knock-out cells (Figure 5-10) (107, 108). The reporter contains a PKA substrate site and FHA1 domain in the middle of the construct. At each terminus, there is a FRET pair that can be tethered. The FRET signals can change based on the conformational changes of the reporter. In the basal unphosphorylated state, the fluorophore pair is far apart with low FRET signal. Once the substrate site is phosphorylated by the PKA, the FHA1 domain would binds to the phosphopeptide and induces an overall conformational change that brings the two FRET partners together which increases the FRET signal.

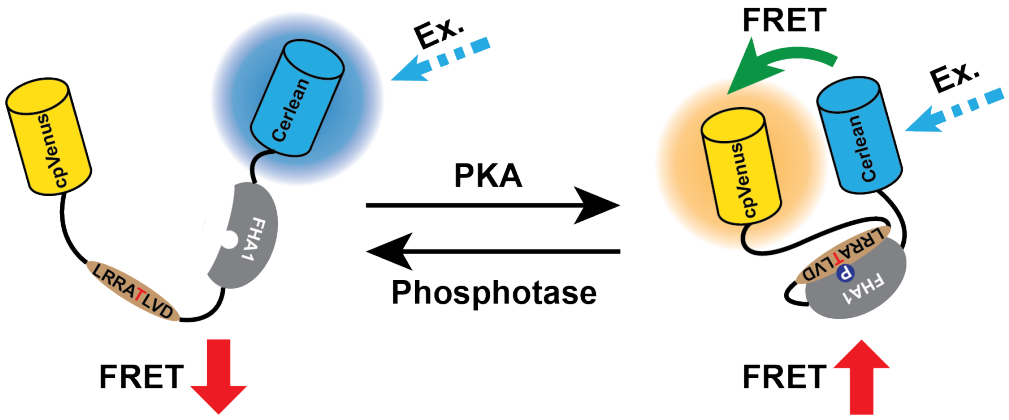

Figure 5-10. FRET-based PKA activity reporter.

Therefore, according to the FRET intensity, we are able to investigate the PKA activity in the cells. To stimulate the ATP synthesis in the cells, we first treated the starved cells with glucose, which can stimulate both anaerobic glycolysis and oxidative phosphorylation (OXPHOS) (Figure 5-11). The PKA activity is slightly elevated in the RIα/RIβ double knock-out cells, while the FRET signal (i.e. PKA activity) in the RIIα/RIIβ double knock-out cells is rapidly and significantly decreased after glucose treatment. These results are consistent with our *in vitro* data that ATP can stabilize RIα holoenzyme where it can destabilize and facilitate RIIβ holoenzyme activation with cAMP (Figure 2-6). However, both of the cells may still have endogenous levels of PKI, which, similar to RI-subunits, contains a pseudo-substrate sequence in its inhibitory site. This could explain why the FRET signal in the RIα/RIβ double knock-out cells has less amount of increase after glucose treatment (Figure 5-11).

Strikingly, the cells have quite different responses after the galactose treatment. The signals of the reporters in both double knock-out cells remain unchanged after galactose treatment. The double knock-out cells were made in HEK293T cells, which are derived from kidney cancer cells. Most of the cancer cells have dysfunctional mitochondria and the OXPHOS pathway, which is called as Warburg effect(109, 110). Our results can be explained by the Warburg effect.

Galactose, unlike glucose, consumes extra energy to get into the glycolyic pathway; there is no energetic yield from glycolysis. Galactose, therefore, only activates the OXPHOS pathway; no energy comes from glycolysis (111, 112). Unlike normal cells, the majority of energy for cancer cells come from glycolysis instead of OXPHOS, due to the dysfunction mitochondria. Thus, galactose treatment has no effect on PKA activity in both knock-out HEK293T cells.

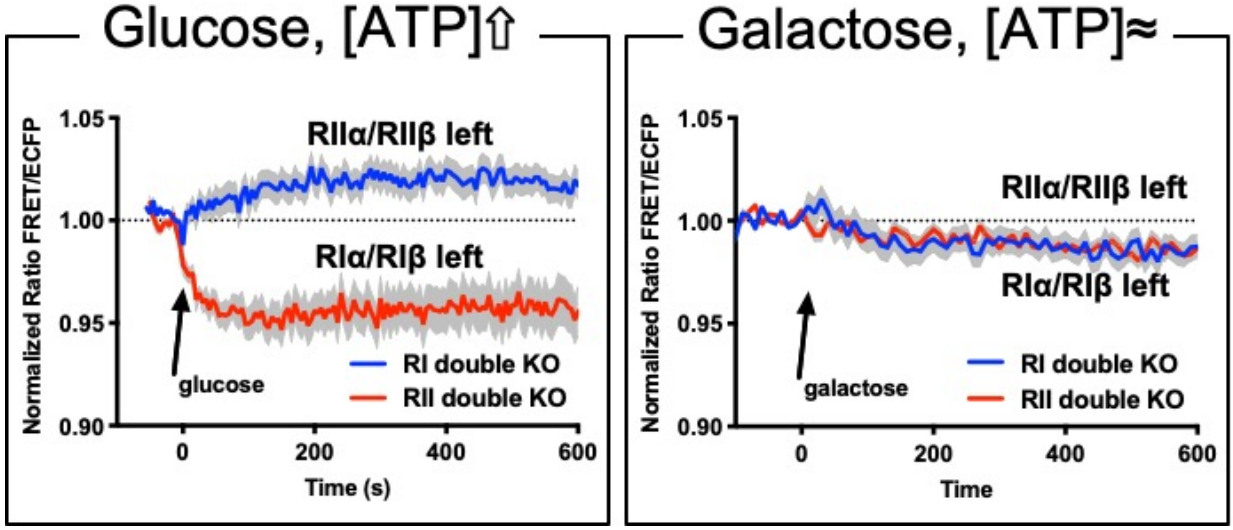

Figure 5-11. ATP has distinct effect on RI and RII double knock-out cells.

Both of our *in vivo* and *in vitro* studies reveal that RI and RII have distinct allostery. We also showed that the PKA-dependent pathway can be further dissected to, at least, RI and RII-dependent, and each of them has different responses under glucose stimulation. Meanwhile, we also showed Warburg effect on PKA-dependent signaling. This also sheds the light on the distinct PKA-dependent pathway in cancer and normal cells.

Chapter 6 Conclusions

In this chapter, I would like to summarize my findings about the PKA pathway focusing on structure, allostery, localization and cellular response. In addition, I list some of the unsolved questions that can be potentially be tackled with the future studies.

6.1 Isoform-specific PKA signaling

Even though all the PKA R-subunits retain the same domain organization, we have shown that RIα and RIIβ holoenzyme have distinct quaternary structures, allostery and localization. The RIα and RIIβ holoenzymes also respond differently to ATP. In the case of the RIα holoenzyme, ATP acts as orthosteric inhibitor, whereas in the RIIβ holoenzyme, ATP serves as substrate that facilitate activation with cAMP(73). I also utilized CRISPR-Cas9 gene editing to generate RIα/RIβ and RIIα/RIIβ double knock-out cells. These cell lines also respond differently to ATP stimulation. ATP also regulates the R- and C-subunits binding. In the presence of ATP, RIα showed strong binding with C-subunit (K_d < 0.1 nM), in contrast to holoenzyme formed in the absence of nucleotide (K_d = 15 nM)(51). However, RIIβ holoenzyme displayed weaker affinity in the presence ATP (K_d = 7 nM), compared to in the apo conditions (K_d = 0.39 nM)(24).

To summarize, these data all indicate that the RIα and RIIβ holoenzymes have different regulation mechanisms, and they are likely involved in distinct cellular pathways. In this chapter, I would like to discuss the molecular mechanisms that regulate the RIα and RIIβ holoenzymes.

6.1.1 RIα holoenzyme

In the previous chapters, we identified two conformations of the RIα holoenzyme. Based on our studies, the conformational changes between Molecule A (Conformation 1) and Molecule

B (Conformation 2) are mediated by ATP. In both of the conformations, similar to the $RI\alpha_2$ structure, the two RIα:C protomer have an antiparallel orientation with the N3A motifs serving as the holoenzyme interface. Because the CNB-B domains directly contact the CNB-A domains from the opposite protomer, the movements of CNB-B domains are limited in these two conformations. In comparison to the allosteric studies of the (Δ1-91)RIα:C complex(16), most of the previous biophysical studies showed that the CNB-B domains are flexible, and its dynamic feature is crucial for cAMP activation(19, 61).

Another RIα holoenzyme model has been proposed based on the RIα(73-244):C crystal structure packing (113). According to the crystal packing of the RIα(73-244):C structure, we were able to build the RIα holoenzyme model with the linker region serving as the holoenzyme interface leaving unconstrained CNB-B domains. This state (Quenched state) has solvent exposed CNB-B domains including solvent exposed N3A-motifs. The CNB-B domains are flexible in this model.

We thus propose there are at least three conformations of the RIα holoenzyme, and these three conformations can represent an ensemble of the RIα conformational states and each has distinct allosteric mechanisms for activation (Figure 6-1A). These states would be in equilibrium. The apo state in the absence of ATP is represented by Conformation 2. In the presence of ATP, the equilibrium shifts to Conformation 1, whereas in the absence of ATP equilibrium would favor Conformation 2. To avoid motif clashes, any of these conformational changes would need to go through a partially dissociated complex where the two RIα:C protomers are no longer in contact (Figure 6-1A). We thus hypothesize that this dissociation state is an obligatory intermediate for transitioning between the three conformational states. However, it is not clearly that under what conditions can drive the equilibrium to the Quenched state. The Quenched state may be the third option where there are two Mg^{2+} ions and ATP. This equilibrium can be influenced by several

factors that reflect the metabolic states of the cell. Many plausible mechanisms, such as metal ions, oxidation state, hydrolysis of ATP, or even other binding partners, can in principle influence this equilibrium. This question will be left for future studies.

To further investigate these different conformational states, we calculated the interface free energy of each state by using the online program, PRODIGY (Figure 6-1B)(114). Among these three states, Conformation 1 is the most stable one, where Conformation 2 and Quenched states are less stable with free energy 2.3 kcal/mol and 3.4 kcal/mol higher than Conformation 1, respectively. The partially dissociated state, hypothesized to be the intermediate, has highest free energy (8.1 kcal/mol higher than the Conformation 1).

Each of the conformational states may correlate with different functions. For example, Conformation 1 should be the conformation responsible for the PKA activation with C-subunit dissociation, since both Conformation 1 and RIα_2 structure share almost the same N3A-N3A' interface(17). However, we cannot exclude the possibility of the PKA activation without C-subunit dissociation, and if so, we have no evidence in what conformation is more likely to happen. This is another question that need to be tackled in the future.

Conformation 2 is believed to be the major conformation responsible for phase separation body formation. We get clues from two specific experiments: 1) RIα- and C-subunits mixture is easier to form phase separation body in the absence of ATP. 2) The N3A-motif mutant, Tyr120$^{RI\alpha}$, cannot form phase separation body. From these two conditions, we can conclude that if the equilibrium would shift to Conformation 2, it would promote phase separation body formation, whereas pushing the equilibrium to Quenched state or Conformation 1 can lead to diffuse state (Figure 6-1A). Hence, we can hypothesize that the Conformation 2 is the main conformation for forming phase separation body.

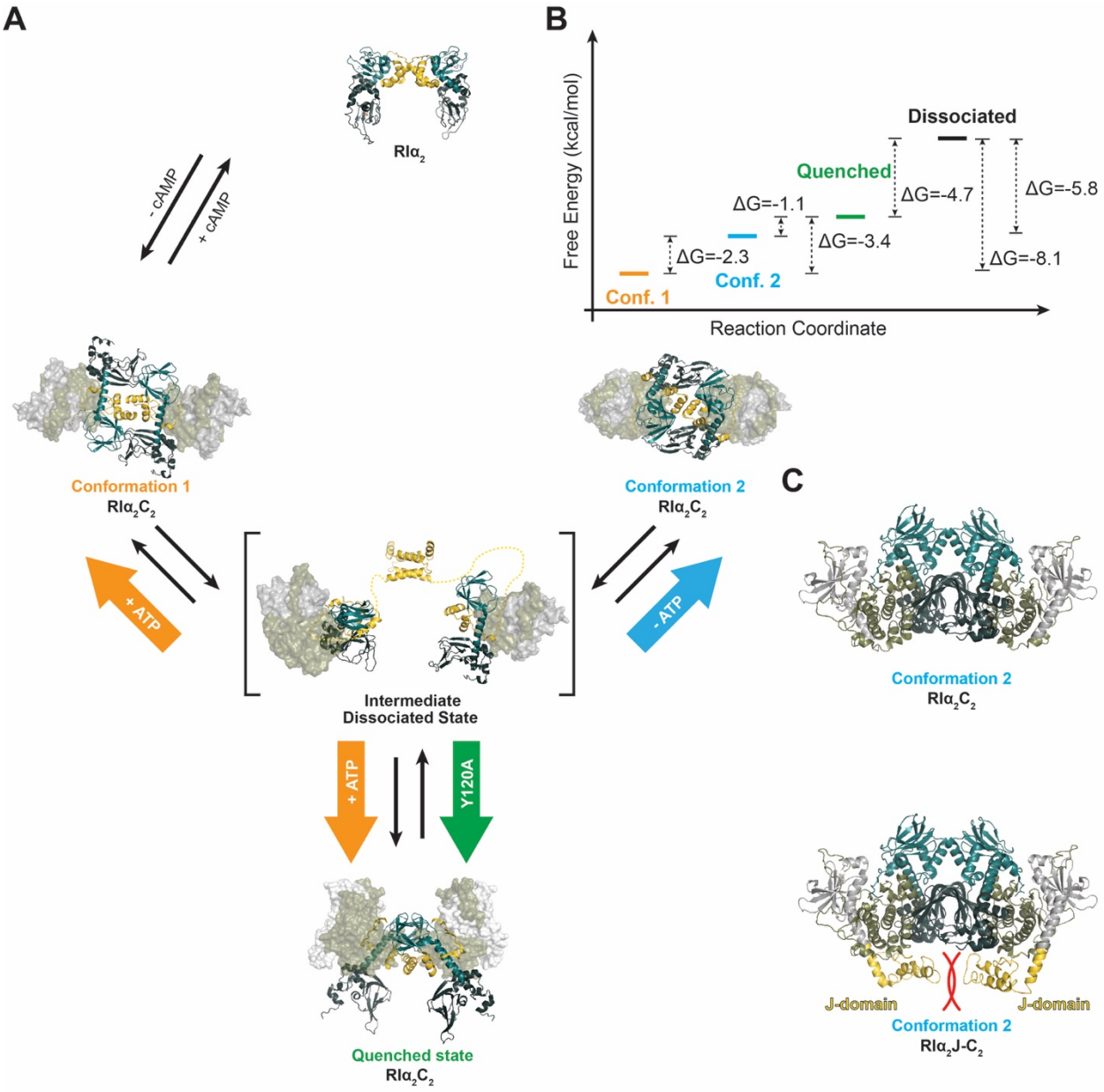

Figure 6-1. The equilibrium model of RIα holoenzymes. (A) The conformational changes of three RIα holoenzyme states. (B) Interface energy calculations of three states. (C) The two J-domains would clash each other in the Conformation 2.

This hypothesis can also explain why DnaJB1-PKAc can disrupt RIα phase separation body formation. If we replace the C-subunit with J-C-subunit in Conformation 2, the two J-domains would be in close proximity (Figure 6-1C). As we have shown earlier, the J-domain is extremely flexible, so the close proximity could disfavor this conformation. Therefore, the whole equilibrium would shift to either Conformation 1 or the Quenched state, which does not favor forming the phase separation body. These results can also explain why we did not see Conformation 2 in the DnaJB1-PKAc holoenzyme with RIα.

6.1.2 RIIβ holoenzyme

Unlike RIα, there are only two known states, the apo state and phosphorylated/ADP bound state, in the RIIβ holoenzyme. Both the apo and phosphorylated/ADP bound states essentially have the same conformation (22); however, they have different cAMP sensitivities for activation (Figure 6-2A)(24, 73). The apo form is more resistant to cAMP, whereas the phosphorylated/ADP bound form is easier to activate with cAMP. In cells, the phosphorylated/ADP bound state can represent the basal state(115), where the apo state would only exist when it is de-phosphorylated by the phosphatase, such as Calcineurin (Figure 6-2A)(115-118).

In comparison to the RIα holoenzyme, the RIIβ holoenzyme is different. Both of the holoenzyme states (apo and phosphorylated/ADP bound RIIβ) can *in vitro* be activated with cAMP, which will promote dissociation of the C-subunit. On the other hand, we cannot exclude the possibility that PKA activation occurs without C-subunit dissociation. The phosphorylated/ADP bound state, which in the absence of cAMP is the predominant state in the cell is most likely to be the conformation that can be activated without C-subunit fully dissociated (24, 115). Phosphorylation of the RIIβ-subunit decreases the ability of inhibitory sequence to bind to the C-subunit active site cleft, therefore other substrates, especially those tethered in close

proximity to the holoenzyme, can more easily compete with the phosphorylated inhibitory sequence of RIIβ-subunit and get into the C-subunit active site.

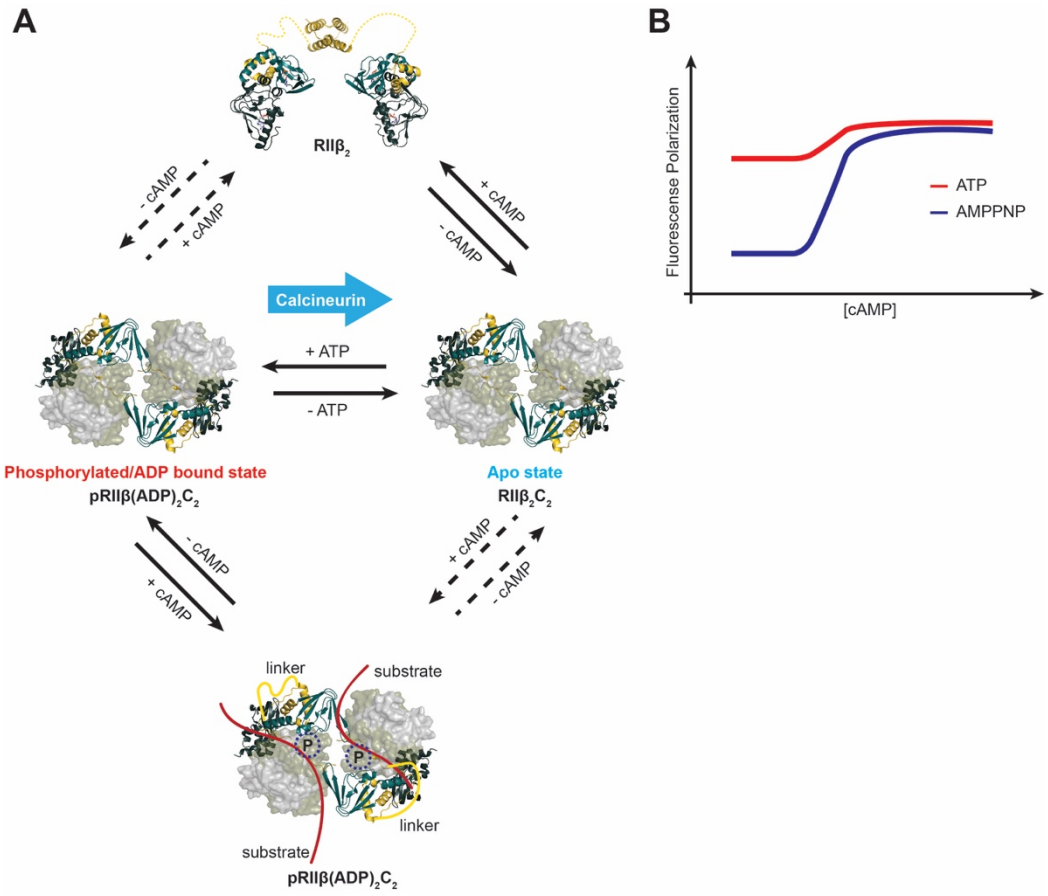

Figure 6-2. The equilibrium model of RIIβ holoenzyme. (A) The equilibrium of two RIIβ holoenzyme states. (B) The RIIβ holoenzyme has higher polarization background in the presence of ATP.

This phenomenon was also observed in our polarization assay where we used a fluorophore labeled PKI peptide as a probe to test the activation of the PKA holoenzyme with cAMP (Figure 6-2B). When the peptide binds to the C-subunit, the fluorescence polarization increases due to the increase in the size of the PKI peptide:C complex compared to the free peptide (119). We always get a high fluorescence polarization background when we incubate the RIIβ holoenzyme with ATP, even at low concentrations of cAMP; however, when we replace ATP with a non-hydrolyzable ATP analog, AMP-PNP, the polarization background is much lower (Figure 6-2B). This data indicates that when the RIIβ-subunit is phosphorylated, the peptide substrate can easily enter into the C-subunit active site even when the C-subunit is not fully dissociated from the RIIβ-subunit. With AMP-PNP, we trap a high affinity ATP bound state where the γ-phosphate cannot be transferred in contrast to ATP where the γ-phosphate is immediately transferred to the inhibitor site of the RIIβ subunit.

6.2 Questions for the future studies

There are many questions that remain unsolved in this field. One of the main directions is to understand the allostery of PKA RI and RII holoenzymes. Even though we have identified several conformations in the RIα and RIIβ holoenzymes, some of the detail mechanisms are still elusive. 1) What exact conditions can drive the RIα holoenzyme to Quenched state? 2) How does the conformation change form one state to the other? Can we trap a fully dissociated state of the cAMP-bound RIα holoenzyme? 3) Are there any more conformation-specific functions in each state? 4) Can we manipulate the holoenzyme equilibrium both *in vitro* and *in vivo*?

We have also shown that the fusion protein can affect each of the RIα holoenzyme localization and RIIβ holoenzyme molecular dynamics. These perturbations can be profound and

what is the consequence for the downstream signaling? Can the fusion protein impair the downstream signaling? The information can be insightful for developing therapeutical strategies.

Our R-subunit knock-out cell lines and localization studies are great platforms for us to further understand the PKA functions in the cells. By advances in mass spectrometry-based proteomics, we can dissect the PKA-signaling pathway in an isoform-specific way. Together with localization data and functional studies, we should also be able to tackle each of the R-subunit holoenzyme function at specific cellular localization.

The reporter assay in knock-out cell lines is also a great way to study isoform-specific cellular response and screen small compounds that target to different isoforms. Together with the downstream gene expression assay, we can elucidate the PKA isoform-specific pathway and potentially screen for the drugs that can specifically target to certain isoforms. Since each disease can disrupt different isoforms of PKA signaling, these strategies can be very useful for the future drug development.

The other interesting direction is to link the PKA isoforms regulation to their upstream target. We can study if different cAMP sources have different effects on each PKA isoform. Forskolin activates transmembrane adenylyl cyclases, whereas bicarbonate can stimulate soluble adenylyl cyclase. What are the consequence and response in each R-subunit knock-out cell under different ways of stimulations, eg. Forskolin vs. bicarbonate? Our reporters and knock-out cells will be good tools to tackle this question.

Our research lays the foundation to understand the molecular mechanism, localization, pathway, and allosteric regulation of PKA holoenzymes. There are many more unsolved questions that need to be explored, and we are looking forward to expanding our understandings of PKA-dependent signaling in the future.

Chapter 7 Material, methods and references

7.1.1 Protein purification

All wild-type C-subunit, J-C-subunit, and deletion mutants of J-C-subunit were purified with a similar purification protocol. The constructs were transformed into BL21(DE3), 0.5 mM IPTG was added to induce the cells at OD_{600}=0.6-0.8. After 16 hours of expression at 4°C. The bacterial pellets were re-suspended and lysed in the lysis buffer: 20 mM Tris-Cl, 300 mM NaCl, 5 mM β-mercaptoethanol (BME). After high speed centrifugation (13,000 rpm, 1hr), the supernatant was collected then passed through the Ni-resin. The resin was first washed with 3CV of wash buffer (20 mM Tris-Cl pH=8.0, 300 mM NaCl, 10 mM imidazole, 5 mM BME), and then C-subunit was eluted by 3CV of elution buffer (20 mM Tris-Cl pH=8.0, 300 mM NaCl, 500 mM imidazole, 5 mM BME). The eluent was collected and supplemented with Ulp1 (molar ratio SUMO-C : Ulp1 = 200 : 1). The mixture was dialyzed against the buffer (20 mM Tris-Cl pH=8.0, 300 mM NaCl, 5 mM BME) at 4°C overnight. After SUMO tag cleavage, the cleaved SUMO tag and uncleaved protein were removed by passing the solution back through the Ni-resin. The proteins were further purified by S-75 gel filtration column with buffer (20 mM MES pH=6.5, 300 mM NaCl, 5 mM BME).

The RIα- and RIIβ-subunit purifications are similar same as the literatures(17, 22).

7.1.2 Holoenzyme formation

Holoenzyme was prepared by mixing RIα- or RIIβ-subunit (1 equiv.) with excess of C-subunits (1.3 equiv.). The mixture was dialyzed against holoenzyme buffer: 50 mM MES pH=5.8, 50 mM NaCl, 1mM TCEP and add extra 5mM $MgCl_2$ and 0.5mM ATP if it is RIα. Unbound C subunits were removed by S-200 gel filtration column with the same holoenzyme buffer.

7.1.3 The RIα$_2$C$_2$ RIα$_2$J-C$_2$ holoenzyme structure determination and refinement

Single crystals of RIα$_2$C$_2$ and RIα$_2$J-C$_2$ holoenzyme were grown in hanging drops using the vapor diffusion method by mixing 1 µl of the protein solution (7.5 mg/ml) and 1 µl of the reservoir solution (100 mM imidazole/MES pH=7.0, 90 mM NPS, 16.8% v/v Ethylene glycol, 8.4 % w/v PEG 8000). The original condition was from Molecular Dimension Morpheus C6 condition) at 22.5 °C. The RIα$_2$J-C$_2$ crystals were grown in a buffer containing 100 mM NaCl, 16-18% pentaerythritol propoxylate and 10% dimethyl sulfoxide and to their final size in ~2 weeks. Crystals were flash frozen and the X-ray diffraction data sets were collected at the Advanced Light Source, Berkeley California beamline 8.2.2 and processed with HKL2000(3). The structure phasing was solved using the (1-91Δ)RIα:C heterodimer structure (PDB 2QCS) as a molecular replacement search model. The structure determination and refinement were carried out using CCP4 and Phenix, respectively. Model building was performed using Coot(120). The structures were refined using Phenix. The structure model has a good geometry as evaluated with PROCHECK(121).

7.1.4 Hydrodynamic radius

The Hydrodynamic Radius of the protein constructs were determined using Gel filtration Chromatography on an Analytical Sephadex S-200 column from Amersham Pharmacia. Buffer conditions used included 2mM $MgCl_2$, 10mM MOPS pH 7.0, 50mM NaCl and 1mM TCEP. For the size exclusion runs with ATP, 0.2mM was also included in the above mentioned buffer composition. All runs were carried out at constant flow rate of 1.0 mL/min. The experiment relied on the combination of Stokes-Einstein equation with retention theory to calculate the R_h (assuming it as a sphere)(7). A standard curve for the column was created using the Molecular Weight Kit from Sigma Aldrich (MWGF200). The Rh of the proteins were deconstructed from the said

standard curve and the Perrin Shape factor was calculated using the theoretically calculated R_g (= 0.66M1/3; where M is the Molecular Weight in Daltons)(8).

7.1.5 Grid preparation and data acquisition for RIIβ$_2$J-C$_2$ holoenzyme

For negative stain sample preparation, 4 µL of RIIβ$_2$J-C$_2$ at 40nM was incubated on continuous carbon grids (Electron Microscopy Sciences, Hatfield, PA; CF400-Cu) for 30 s. After incubation, the grid was transferred directly onto 5 × 75 µl droplets of 2% uranyl acetate and then blotted dry. Negative stain grids were imaged on an Tecnai Sphera (FEI Company, Hillsboro, OR) at 200 kV using a US4000 CCD detector (Gatan Inc., Pleaston, CA) with the Leginon(122) automated data collection software over a defocus range of 1–2.5 µm and a dose of 40 e-/Å2 at a nominal magnification of 62,000X (1.90 Å/pix).

For cryo-EM sample preparation, 4µl of RIIβ$_2$J-C$_2$ at 2µM was applied to a glow-discharged UltraAuFoil R (1.2/1.3) 300-mesh gold grid (Electron Microscopy Sciences). The grids were then blotted with filter paper and plunge-frozen into ethane cooled with liquid nitrogen using a Vitrobot Mark IV (Thermo Fisher Scientific) set to 4 °C, 100% humidity, 4 s blot, and a force of 20. Micrographs were collected using Leginon(122) on a Titan Krios transmission electron microscope (Thermo Fisher Scientific) operating at 300 keV using a Gatan K2 Summit direct electron detector (Gatan, Inc) in counting mode (1 Å/pixel) at a nominal magnification of 29,000X using 100 ms frame rate for 10 seconds with a total dose ~78e/Å2. All images were collected using a stage tilt of 40 degrees to increase orientation distribution (123, 124). Appion(125) was used for on-the-fly preprocessing to run MotionCor2(126) and CTFFIND4(127).

7.1.6 Image processing

Particles were picked and extracted using Appion preprocessing software. 693,293 particles were picked from 1,129 micrographs with the FindEM(128) software, using 2D class

averages from untilted cryo-EM data for RIIβ$_2$J-C$_2$ as templates. Particles were extracted using RELION(129) and local CTF values calculated by Gctf(130) to produce a particle stack at 1Å/pixel and a box size of 256 pixels. The particle stack was imported into cryoSPARC(131) (v0.65) for 2D classification. After throwing away bad classes, we used 153,426 particles for ab initio classification into 3 classes using cryoSPARC (v0.65). We selected a single good class containing 69,605 particles for homogenous refinement in cryoSPARC (v0.65), applying C2 symmetry to obtain a 6.2Å structure (-302Å^2 B-factor). Using the resulting particle stack, we performed 3D classification using RELION (v2.1) into 5 classes. After selecting the 21,330 particles associated with the map containing an extra density for CNB-B, we performed another round of 3D refinement using RELION to obtain a structure at 8.5Å using C1 symmetry. In order to obtain more information about the CNB-B domain, we created a mask and used this to perform classification without alignment to enrich for particles containing extra density. From one class, we used 11,182 particles to obtain a 7.5Å structure (C1 symmetry). For this, we then filtered according to local resolution using a B-factor of -500Å^2.

7.1.7 Model building and refinement

The crystal structure of wt RIIβ holoenzyme (PDB = 3TNP) and DnaJB1-PKAc (PDB = 4WB7) alone were chosen as initial models. To generate RIIβ$_2$J-C$_2$ model, the C-subunits in RIIβ holoenzyme were replaced with the J-C-subunits and submitted to HHpred (https://toolkit.tuebingen.mpg.de/#/tools/hhpred), using the top 10 scoring homologous models. This model was then initially refined using Rosetta(132) with the locally filtered cryo-EM map. We calculated 200 models and used top scoring model for a final refinement.

The real-space refinement of C1 symmetry structure was carried out by using Phenix. Further model refinement was performed by using Coot(120). The C2 symmetry structure was

derived from the refined C1 symmetry structure. Based on the C2 symmetry map, the N-terminus (residue 1 - 48) of J-C-subunit and CNB-B domain (residue 266 - 416) of RIIβ-subunit were removed from C1 symmetry structure. Both the two structure models have good geometry as evaluated with PROCHECK(121).

7.1.8 System preparation for MD

Holoenzyme complexes were prepared from either $RII\beta_2C_2$ or $RII\beta_2J\text{-}C_2$. The models were processed in Maestro (Schrodinger) where missing sidechains, counter ions, and ioniziable side chains were modeled in the Protein Preparation Wizard. Hydrogens were added and the models were solvated in a cubic box of TIP4P-EW water(133) and 150 mM KCl with a 10 Å buffer in AMBERtools(134). Parameters from the Bryce AMBER Parameter Database were used for phosphothreonine and phosphoserine(135).

7.1.9 MD simulations

AMBER16(134) was used for energy minimization, heating, and equilibration, using the CPU code for minimization and heating and GPU code for equilibration. 500 steps of hydrogen-only minimization was followed by 500 steps of solvent minimization, 500 steps of sidechain minimization, and 5000 steps of all-atom minimization. Systems were heated from 0K to 300 K over 500ps with 2fs timesteps and 10.0 kcal×mol×Å position restraints on protein and ligand. Temperature was maintained by the Langevin thermostat. Constant pressure equilibration with a 10 Å non-bonded cut-off with particle mesh Ewald was performed with 100ps of protein and ligand restraints followed by 100ps without restraints. Hydrogen mass repartition was implemented to achieve a 4fs time-step for production runs(136). Production simulations were performed on GPU enabled AMBER16(137, 138) as above in triplicate for a total aggregate simulation time of 1.5μs for each complex. Gaussian accelerated MD (GaMD) was also used to enhance conformational

sampling(139) of the holoenzyme complexes (C, J-C, and J-C(Δ1-69)). Systems were prepared, minimized, heated, and equilibrated identically to the conventional MD simulations. GaMD applies a Gaussian distributed boot to the potential energy surface which accelerated transitions between states while allowing accurate reweighting with cumulant expansions. Both dihedral and total potential acceleration were used simultaneously. Each GaMD simulation was equilibrated for 50ns during which boost potentials were updated every 2ns. For each construct 8 independent replicas of 100ns of GaMD simulation were run in the NVT ensemble.)

7.1.10 MD analysis

The first 50ns of each simulation was removed prior to analysis. Trajectories were aligned to the least dynamic regions of the protein by superposing only Cα atoms with an initial RMSF less than the mean. The displacement vector between CNBA and CNBB was put into the same reference frame for all constructs by aligning the CNBA domain of each R protomer over CA atoms for residues 169-246 to the same reference structure for both protomers prior to calculating the vector between Arg230 and Arg359. Solvent accessible surface area was calculated for residues 302, 321, 323, 339, 348, 350, 351, 352, 359, 360, 361 which form the cyclic-nucleotide binding pocket in the CNB-B domain of RIIβ. The Shrake-Rupley method, within MDtraj, with a probe radius of 0.3nm, similar to the radius of a cAMP molecule, was used for the SASA determination per frame. Plotting and analysis were performed in python.

7.1.11 SAXS analysis and model building

SAXS data were collected at beamline SIBYLS at Advanced Light Source equipped with Agilent 1260 series HPLC with a Shodex analytical column. Data were collected at 298K with sample to detector distance at 1.5 m and λ=1.03Å. Samples concentration was both ~5 mg/mL, with 60 μL in each loading. Buffer signals were subtracted based on the measurement of averaged

background scattering in each sample. The scattering files were transformed into real space pair distance distribution function *P*(r), and R_g and D_{max} were also calculated based on the *P*(r) function(140). Radius of gyration (R_g) was calculated from consecutive data throughout the FPLC and checked for consistency. All data were then scaled and merged as the final plot. Both samples have no sign of aggregation according to the Guinier analysis at low scattering angles(q). The Data were analyzed by ATSAS 2.8(141). Molecular weight estimation of each complex was calculated based on the formula: MW = Porod Volume / 1.7.

SAXS model was built by using the program CAROL(74). The flexible regions, such as residues 1-14 in C-subunit, residues 122-129, 44-103, 325-336, and 394-416 in RIIβ-subunit, were built as poly-Gly chains. The structural model of D/D domain was generated based on the homologous modeling by using the online program, I-TASSER(76).

7.1.12 Kinase activity assay

The enzymatic activity of wt or chimeric catalytic subunit was measured spectrophotometrically with a coupled enzyme assay. The ADP formation is coupled to the pyruvate kinase (PK) and lactate dehydrogenase (LDH) reactions. The reaction rate is determined by following the decrease in absorbance at 340 nm at 25 °C on a Photodiode Array Lambda 465 UV/Vis Spectrophotometer (PerkinElemer). The Michaelis-Menten parameters for ATP were determined by fixing Kemptide substrate (LRRASLG) at saturating concentrations while varying the concentrations of ATP. Reactions were pre-equilibrated at room temperature and initiated by adding ATP. The kinase reaction mixture contained 100 mM MOPS pH 7.1, 50 mM KCl, 6 mM phosphoenolpyruvate, 0.5 mM nicotinamide adenine dinucleotide (NADH), 100 μM of Kemptide, 15 units of LDH, 7 units of PK, and varying concentrations of ATP from 0 to 250 μM. MgCl2 was

present in a constant 1 mM excess over ATP. The data was analyzed and fitted to the Michaelis-Menten equation using SigmaPlot software.

7.1.13 Inhibitor Peptide PKI Binding Assay

Fluorescence anisotropy was used to measure PKI to C- or J-C-subunit. 0.9 nM FAM-labeled PKI (5-24) peptide was mixed with 0-2000 nM C- or J-C-subunit in buffer containing 20 mM MOPS pH 7.0, 150 mM NaCl, 10 mM $MgCl_2$, 1 mM ATP, and 0.01% Triton X-100. Fluorescence anisotropy was measured by using GENios Pro micro-plate reader (Tecan) in black flat-bottom costar assay plates with 485 nm excitation and 535 nm emission.

7.1.14 Stability assay

ThermoFluor assay was used to measure the stabilities of apo C- or J-C-subunit subunits and its ATP and/or peptide binding forms. The reaction was conducted with 5 μM of proteins in 45 μL of the buffer containing 20 mM MOPS pH 7.0, 150 mM NaCl. Ligands were used at the following concentrations 1 mM ATP, 10 mM $MgCl_2$, and 25 μM PKI peptide. For each ligand, triplicate reactions were measured in 96-well plate. After proteins and ligands were mixed and incubated for 5 min on ice, 5 μL of 200X SYPRO Orange dye was added to each reaction. The samples were heated from 20 to 85 °C with a 0.5°C/min heating rate by using CFX96 Real-Time PCR Detection System (Bio-Rad) in temperature scanning mode. The fluorescence signals were measured using the ROX channel.

7.1.15 ATP binding assay

ATP dissociation constants were determined using the ThermoFluor assay. Similar condition as thermostability assay was used for ATP binding, except a range of ATP concentrations from 0 to 1 mM were mixed with C- or J-C-subunit. After everything was mixed

and incubated for 5 min on ice, 5 μL of 200X SYPRO Orange dye was added to each reaction. The samples were heated from 20 to 85 ˚C with a 0.5 ˚C/min heating rate by using CFX96 Real-Time PCR Detection System (Bio-Rad) in temperature scanning mode. The final concentration 4.5 μM of catalytic subunits was used to fit the data. The fluorescence signals were measured using the ROX channel. Each melting temperature was recorded and plotted versus ATP concentration.

7.1.16 Fluorescence polarization assay

The cAMP activation assay of RIα and RIIβ holoenzymes was measured by a fluorescence polarization assay(142). The holoenzyme was formed by mixing C-subunit (or J-C-subunit or J-C deletion mutants) and RIα or RIIβ with molar ratio 1:1.2 in buffer: 2 mM HEPES pH=7.0, 75mM KCl, 0.005% Triton X-100, 1mM DTT, 10mM $MgCl_2$, and 1mM ATP(RIα) or AMP-PNP(RIIβ). A N-terminus fluorescein-labeled 20-residue PKI(5-24) peptide (FAM-IP20) was then added into the reaction. The working concentration of C-subunit was 12nM, FAM-IP20 was 2nM, and RIIβ was 14.4nM. A two-fold serial dilutions of cAMP from 2,000 to 0 nM(RIα) or 8,000 to 0nM(RIIβ) were added to each reaction. The polarization changes were from the FAM-IP20 binding to the C-subunit. Excitation and emission wavelength (485 nm and at 535 nm, respectively) to measure its polarization. The experiments were carried out with a GENios Pro micro-plate reader (Tecan) using black flat-bottom 96-well plates. Each data was repeated at least four times and the data sets were analyzed with Prism 7.

7.1.17 Fluorophore Labeling

To label with fluorophore, the Lys7 on Human C subunit was mutated to Cys. The mutagenesis was done using NEB Q5-site directed mutagenesis kit, and the primers were designed based on the online tool NEBBaseChanger. Purification of C-subunit Lys7Cys mutant was the

same as wild-type C-subunit. The purified protein was collected and incubated with 5 equiv. of Fluorescein-5-Maleimide in labeling buffer 20mM MES pH=6.5, 300 mM NaCl, 5 mM BME. After incubation at room temperature for one hour, the labeled-protein was injected to the S-200 column to remove the excess amount of un-reacted fluorophore.

7.1.18 Polarization Assay

The cAMP activation assay and R-C binding of RIα and RIIβ were investigated by a fluorescence polarization assay. For R-C binding, holoenzymes were formed in situ by mixing 10nM of Fluorescein labeled C-subunit and 2-fold serial dilution of R-subunits from 2000nM to 0nM in buffer 20 mM MOPS pH=6.5, 75 mM KCl, 0.005% Triton X-100, 1 mM DTT, 10 mM $MgCl_2$, and 1 mM ATP/ADP as indicated. For cAMP activation assay, holoenzymes were formed in situ by mixing 10nM of Fluorescein labeled C-subunit with 500nM of R-subunits in buffer 20 mM MOPS pH=6.5, 75 mM KCl, 0.005% Triton X-100, 1 mM DTT, 10 mM $MgCl_2$, and 1 mM ATP/ADP as indicated. A two-fold serial dilutions of cAMP from 1,0000 to 0 nM were added into each reaction to check the holoenzyme dissociation. All reactions were incubated for at least 20 min to reach equilibrium before being measured.

Excitation and emission wavelength (485 nm and at 535 nm respectively) were used to measure its polarization. The experiments were carried out with a GENios Pro micro-plate reader (Tecan) and black flat-bottom 96-well plates. Each data was repeated at least four times and the data sets were analyzed with Prism 7. Although Due to the detection limit of the assays, the measurement of half maximal effective concentration (EC_{50}) is not equal to the dissociation constant (K_d), however is sufficient to observe ATP and ADP difference.

7.1.19 Helical and capping propensity analyses

The online program, Agadir, was used to analyzed the helical and capping residues propensity of αB/C/N helix in RIα and RIIβ, αA-helix in wt C-subunit, and J-domain(143).

7.1.20 CRISPR knock-out cells

Two designed guide sequences (RIα: 5'-TGGCAGTACCGCCGCCAGTG-3' and 5'-AGAGACCCATGGCATTCCTC-3'; RIβ: 5'-CTCGTCCTCCTCCGAGGGGC-3' and 5'-TGCCCCAGGACACGTGCGAA-3'; RIIα: 5'-CCGTGAGCCCCGGCGGGATC-3' and 5'-ACTCCACTGCGAATTCGACG-3'; RIIβ: 5'-GATGAGCATCGAGATCCCGG-3' and 5'-ATTGAACGCCCCTGCGTCCG-3') that specifically target the human gene were each cloned into the sgRNA scaffold in pX458 (gift of Feng Zhang; Addgene plasmid #48138). Cells were co-transfected with these two plasmids when they reached 70% confluency. After 24 h of transfection, the cells were aspirated, washed with DPBS, and filtered through a 35-μm cell strainer. Cells with GFP signals were sorted into single cells in a 96-well plate using a BD FACSJazzTM cell sorter. After single cells had grown into colonies, the cells were transferred to 60-mm cell culture plates. The corresponding genomic DNA segments were sequenced and PCR amplified. Each colony was validated by using western blotting and DNA sequencing.

7.2 Reference

1. Manning G, Whyte DB, Martinez R, Hunter T, Sudarsanam S. The protein kinase complement of the human genome. Science. 2002;298(5600):1912-34. Epub 2002/12/10. doi: 10.1126/science.1075762. PubMed PMID: 12471243.

2. Krebs EG, Graves DJ, Fischer EH. Factors affecting the activity of muscle phosphorylase b kinase. J Biol Chem. 1959;234:2867-73. Epub 1959/11/01. PubMed PMID: 14411853.

3. Fischer EH, Krebs EG. Conversion of phosphorylase b to phosphorylase a in muscle extracts. J Biol Chem. 1955;216(1):121-32. Epub 1955/09/01. PubMed PMID: 13252012; PMCID: 13252012.

4. Krebs EG. Historical perspectives on protein phosphorylation and a classification system for protein kinases. Philos Trans R Soc Lond B Biol Sci. 1983;302(1108):3-11. Epub 1983/07/05. doi: 10.1098/rstb.1983.0033. PubMed PMID: 6137005.

5. Taylor SS, Ilouz R, Zhang P, Kornev AP. Assembly of allosteric macromolecular switches: lessons from PKA. Nat Rev Mol Cell Biol. 2012;13(10):646-58. Epub 2012/09/21. doi: 10.1038/nrm3432. PubMed PMID: 22992589; PMCID: PMC3985763.

6. Knighton DR, Zheng JH, Ten Eyck LF, Ashford VA, Xuong NH, Taylor SS, Sowadski JM. Crystal structure of the catalytic subunit of cyclic adenosine monophosphate-dependent protein kinase. Science. 1991;253(5018):407-14. Epub 1991/07/26. PubMed PMID: 1862342.

7. Keshwani MM, Klammt C, von Daake S, Ma Y, Kornev AP, Choe S, Insel PA, Taylor SS. Cotranslational cis-phosphorylation of the COOH-terminal tail is a key priming step in the maturation of cAMP-dependent protein kinase. Proc Natl Acad Sci U S A. 2012;109(20):E1221-9. Epub 2012/04/12. doi: 10.1073/pnas.1202741109. PubMed PMID: 22493239; PMCID: PMC3356610.

8. Johnson DA, Akamine P, Radzio-Andzelm E, Madhusudan M, Taylor SS. Dynamics of cAMP-dependent protein kinase. Chem Rev. 2001;101(8):2243-70. Epub 2001/12/26. PubMed PMID: 11749372.

9. Taylor SS, Zhang P, Steichen JM, Keshwani MM, Kornev AP. PKA: lessons learned after twenty years. Biochim Biophys Acta. 2013;1834(7):1271-8. Epub 2013/03/29. doi: 10.1016/j.bbapap.2013.03.007. PubMed PMID: 23535202; PMCID: PMC3763834.

10. Knighton DR, Zheng JH, Ten Eyck LF, Xuong NH, Taylor SS, Sowadski JM. Structure of a peptide inhibitor bound to the catalytic subunit of cyclic adenosine monophosphate-dependent protein kinase. Science. 1991;253(5018):414-20. Epub 1991/07/26. PubMed PMID: 1862343.

11. Kinderman FS, Kim C, von Daake S, Ma YL, Pham BQ, Spraggon G, Xuong NH, Jennings PA, Taylor SS. A dynamic mechanism for AKAP binding to RII isoforms of cAMP-dependent protein kinase. Molecular Cell. 2006;24(3):397-408. doi: 10.1016/j.molcel.2006.09.015. PubMed PMID: WOS:000241869500007.

12. Sarma GN, Kinderman FS, Kim C, von Daake S, Chen L, Wang BC, Taylor SS. Structure of D-AKAP2:PKA RI complex: insights into AKAP specificity and selectivity. Structure. 2010;18(2):155-66. Epub 2010/02/18. doi: 10.1016/j.str.2009.12.012. PubMed PMID: 20159461; PMCID: PMC3090270.

13. Herberg FW, Dostmann WRG, Zorn M, Davis SJ, Taylor SS. Crosstalk between Domains in the Regulatory Subunit of Camp-Dependent Protein-Kinase - Influence of Amino-Terminus on

Camp Binding and Holoenzyme Formation. Biochemistry. 1994;33(23):7485-94. doi: DOI 10.1021/bi00189a057. PubMed PMID: WOS:A1994NT32800057.

14. Day ME, Gaietta GM, Sastri M, Koller A, Mackey MR, Scott JD, Perkins GA, Ellisman MH, Taylor SS. Isoform-specific targeting of PKA to multivesicular bodies. J Cell Biol. 2011;193(2):347-63. Epub 2011/04/20. doi: 10.1083/jcb.201010034. PubMed PMID: 21502359; PMCID: PMC3080257.

15. Herberg FW, Taylor SS, Dostmann WR. Active site mutations define the pathway for the cooperative activation of cAMP-dependent protein kinase. Biochemistry. 1996;35(9):2934-42. Epub 1996/03/05. doi: 10.1021/bi951647c. PubMed PMID: 8608131.

16. Kim C, Cheng CY, Saldanha SA, Taylor SS. PKA-I holoenzyme structure reveals a mechanism for cAMP-dependent activation. Cell. 2007;130(6):1032-43. Epub 2007/09/25. doi: 10.1016/j.cell.2007.07.018. PubMed PMID: 17889648.

17. Bruystens JG, Wu J, Fortezzo A, Kornev AP, Blumenthal DK, Taylor SS. PKA RIalpha homodimer structure reveals an intermolecular interface with implications for cooperative cAMP binding and Carney complex disease. Structure. 2014;22(1):59-69. Epub 2013/12/10. doi: 10.1016/j.str.2013.10.012. PubMed PMID: 24316401; PMCID: PMC3963464.

18. Kornev AP, Taylor SS, Ten Eyck LF. A generalized allosteric mechanism for cis-regulated cyclic nucleotide binding domains. PLoS Comput Biol. 2008;4(4):e1000056. Epub 2008/04/12. doi: 10.1371/journal.pcbi.1000056. PubMed PMID: 18404204; PMCID: PMC2275311.

19. Boras BW, Kornev A, Taylor SS, McCulloch AD. Using Markov state models to develop a mechanistic understanding of protein kinase A regulatory subunit RIalpha activation in response to cAMP binding. J Biol Chem. 2014;289(43):30040-51. Epub 2014/09/10. doi: 10.1074/jbc.M114.568907. PubMed PMID: 25202018; PMCID: PMC4208011.

20. Ilouz R, Bubis J, Wu J, Yim YY, Deal MS, Kornev AP, Ma Y, Blumenthal DK, Taylor SS. Localization and quaternary structure of the PKA RIbeta holoenzyme. Proc Natl Acad Sci U S A. 2012;109(31):12443-8. Epub 2012/07/17. doi: 10.1073/pnas.1209538109. PubMed PMID: 22797896; PMCID: PMC3411989.

21. Wu J, Brown SH, von Daake S, Taylor SS. PKA type IIalpha holoenzyme reveals a combinatorial strategy for isoform diversity. Science. 2007;318(5848):274-9. Epub 2007/10/13. doi: 10.1126/science.1146447. PubMed PMID: 17932298; PMCID: PMC4036697.

22. Zhang P, Smith-Nguyen EV, Keshwani MM, Deal MS, Kornev AP, Taylor SS. Structure and allostery of the PKA RIIbeta tetrameric holoenzyme. Science. 2012;335(6069):712-6. Epub 2012/02/11. doi: 10.1126/science.1213979. PubMed PMID: 22323819; PMCID: PMC3985767.

23. Kirschner LS, Yin Z, Jones GN, Mahoney E. Mouse models of altered protein kinase A signaling. Endocr Relat Cancer. 2009;16(3):773-93. Epub 2009/05/28. doi: 10.1677/ERC-09-0068. PubMed PMID: 19470615.

24. Zhang P, Knape MJ, Ahuja LG, Keshwani MM, King CC, Sastri M, Herberg FW, Taylor SS. Single Turnover Autophosphorylation Cycle of the PKA RIIbeta Holoenzyme. PLoS Biol. 2015;13(7):e1002192. Epub 2015/07/15. doi: 10.1371/journal.pbio.1002192. PubMed PMID: 26158466; PMCID: PMC4497662.

25. Brandon EP, Zhuo M, Huang YY, Qi M, Gerhold KA, Burton KA, Kandel ER, McKnight GS, Idzerda RL. Hippocampal long-term depression and depotentiation are defective in mice carrying a targeted disruption of the gene encoding the RI beta subunit of cAMP-dependent protein kinase. Proc Natl Acad Sci U S A. 1995;92(19):8851-5. Epub 1995/09/12. PubMed PMID: 7568030; PMCID: PMC41065.

26. Brandon EP, Logue SF, Adams MR, Qi M, Sullivan SP, Matsumoto AM, Dorsa DM, Wehner JM, McKnight GS, Idzerda RL. Defective motor behavior and neural gene expression in RIIbeta-protein kinase A mutant mice. J Neurosci. 1998;18(10):3639-49. Epub 1998/06/06. PubMed PMID: 9570795.

27. Cummings DE, Brandon EP, Planas JV, Motamed K, Idzerda RL, McKnight GS. Genetically lean mice result from targeted disruption of the RII beta subunit of protein kinase A. Nature. 1996;382(6592):622-6. Epub 1996/08/15. doi: 10.1038/382622a0. PubMed PMID: 8757131.

28. Kirschner LS, Kusewitt DF, Matyakhina L, Towns WH, 2nd, Carney JA, Westphal H, Stratakis CA. A mouse model for the Carney complex tumor syndrome develops neoplasia in cyclic AMP-responsive tissues. Cancer Res. 2005;65(11):4506-14. Epub 2005/06/03. doi: 10.1158/0008-5472.CAN-05-0580. PubMed PMID: 15930266.

29. Amieux PS, Howe DG, Knickerbocker H, Lee DC, Su T, Laszlo GS, Idzerda RL, McKnight GS. Increased basal cAMP-dependent protein kinase activity inhibits the formation of mesoderm-derived structures in the developing mouse embryo. J Biol Chem. 2002;277(30):27294-304. Epub 2002/05/11. doi: 10.1074/jbc.M200302200. PubMed PMID: 12004056.

30. Davies H, Bignell GR, Cox C, Stephens P, Edkins S, Clegg S, Teague J, Woffendin H, Garnett MJ, Bottomley W, Davis N, Dicks E, Ewing R, Floyd Y, Gray K, Hall S, Hawes R, Hughes J, Kosmidou V, Menzies A, Mould C, Parker A, Stevens C, Watt S, Hooper S, Wilson R, Jayatilake H, Gusterson BA, Cooper C, Shipley J, Hargrave D, Pritchard-Jones K, Maitland N, Chenevix-Trench G, Riggins GJ, Bigner DD, Palmieri G, Cossu A, Flanagan A, Nicholson A, Ho JW, Leung SY, Yuen ST, Weber BL, Seigler HF, Darrow TL, Paterson H, Marais R, Marshall CJ, Wooster R, Stratton MR, Futreal PA. Mutations of the BRAF gene in human cancer. Nature. 2002;417(6892):949-54. Epub 2002/06/18. doi: 10.1038/nature00766. PubMed PMID: 12068308.

31. Roskoski R, Jr. The ErbB/HER family of protein-tyrosine kinases and cancer. Pharmacol Res. 2014;79:34-74. Epub 2013/11/26. doi: 10.1016/j.phrs.2013.11.002. PubMed PMID: 24269963.

32. Salesse S, Verfaillie CM. BCR/ABL: from molecular mechanisms of leukemia induction to treatment of chronic myelogenous leukemia. Oncogene. 2002;21(56):8547-59. Epub 2002/12/12. doi: 10.1038/sj.onc.1206082. PubMed PMID: 12476301.

33. Soda M, Choi YL, Enomoto M, Takada S, Yamashita Y, Ishikawa S, Fujiwara S, Watanabe H, Kurashina K, Hatanaka H, Bando M, Ohno S, Ishikawa Y, Aburatani H, Niki T, Sohara Y, Sugiyama Y, Mano H. Identification of the transforming EML4-ALK fusion gene in non-small-cell lung cancer. Nature. 2007;448(7153):561-6. Epub 2007/07/13. doi: 10.1038/nature05945. PubMed PMID: 17625570.

34. Honeyman JN, Simon EP, Robine N, Chiaroni-Clarke R, Darcy DG, Lim, II, Gleason CE, Murphy JM, Rosenberg BR, Teegan L, Takacs CN, Botero S, Belote R, Germer S, Emde AK, Vacic V, Bhanot U, LaQuaglia MP, Simon SM. Detection of a recurrent DNAJB1-PRKACA chimeric transcript in fibrolamellar hepatocellular carcinoma. Science. 2014;343(6174):1010-4. Epub 2014/03/01. doi: 10.1126/science.1249484. PubMed PMID: 24578576; PMCID: PMC4286414.

35. Kirschner LS, Carney JA, Pack SD, Taymans SE, Giatzakis C, Cho YS, Cho-Chung YS, Stratakis CA. Mutations of the gene encoding the protein kinase A type I-alpha regulatory subunit in patients with the Carney complex. Nat Genet. 2000;26(1):89-92. Epub 2000/09/06. doi: 10.1038/79238. PubMed PMID: 10973256.

36. Greene EL, Horvath AD, Nesterova M, Giatzakis C, Bossis I, Stratakis CA. In vitro functional studies of naturally occurring pathogenic PRKAR1A mutations that are not subject to nonsense mRNA decay. Hum Mutat. 2008;29(5):633-9. Epub 2008/02/05. doi: 10.1002/humu.20688. PubMed PMID: 18241045.

37. Linglart A, Menguy C, Couvineau A, Auzan C, Gunes Y, Cancel M, Motte E, Pinto G, Chanson P, Bougneres P, Clauser E, Silve C. Recurrent PRKAR1A mutation in acrodysostosis with hormone resistance. N Engl J Med. 2011;364(23):2218-26. Epub 2011/06/10. doi: 10.1056/NEJMoa1012717. PubMed PMID: 21651393.

38. Elli FM, Bordogna P, de Sanctis L, Giachero F, Verrua E, Segni M, Mazzanti L, Boldrin V, Toromanovic A, Spada A, Mantovani G. Screening of PRKAR1A and PDE4D in a Large Italian Series of Patients Clinically Diagnosed With Albright Hereditary Osteodystrophy and/or Pseudohypoparathyroidism. J Bone Miner Res. 2016;31(6):1215-24. Epub 2016/01/15. doi: 10.1002/jbmr.2785. PubMed PMID: 26763073.

39. Bongarzone I, Butti MG, Coronelli S, Borrello MG, Santoro M, Mondellini P, Pilotti S, Fusco A, Della Porta G, Pierotti MA. Frequent activation of ret protooncogene by fusion with a new activating gene in papillary thyroid carcinomas. Cancer Res. 1994;54(11):2979-85. Epub 1994/06/01. PubMed PMID: 8187085; PMCID: 8187085.

40. Wong TH, Chiu WZ, Breedveld GJ, Li KW, Verkerk AJ, Hondius D, Hukema RK, Seelaar H, Frick P, Severijnen LA, Lammers GJ, Lebbink JH, van Duinen SG, Kamphorst W, Rozemuller AJ, Netherlands Brain B, Bakker EB, International Parkinsonism Genetics N, Neumann M,

Willemsen R, Bonifati V, Smit AB, van Swieten J. PRKAR1B mutation associated with a new neurodegenerative disorder with unique pathology. Brain. 2014;137(Pt 5):1361-73. Epub 2014/04/12. doi: 10.1093/brain/awu067. PubMed PMID: 24722252.

41. Beuschlein F, Fassnacht M, Assie G, Calebiro D, Stratakis CA, Osswald A, Ronchi CL, Wieland T, Sbiera S, Faucz FR, Schaak K, Schmittfull A, Schwarzmayr T, Barreau O, Vezzosi D, Rizk-Rabin M, Zabel U, Szarek E, Salpea P, Forlino A, Vetro A, Zuffardi O, Kisker C, Diener S, Meitinger T, Lohse MJ, Reincke M, Bertherat J, Strom TM, Allolio B. Constitutive activation of PKA catalytic subunit in adrenal Cushing's syndrome. N Engl J Med. 2014;370(11):1019-28. Epub 2014/02/28. doi: 10.1056/NEJMoa1310359. PubMed PMID: 24571724; PMCID: PMC4727447.

42. Walker C, Wang Y, Olivieri C, Karamafrooz A, Casby J, Bathon K, Calebiro D, Gao J, Bernlohr DA, Taylor SS, Veglia G. Cushing's syndrome driver mutation disrupts protein kinase A allosteric network, altering both regulation and substrate specificity. Sci Adv. 2019;5(8):eaaw9298. Epub 2019/09/07. doi: 10.1126/sciadv.aaw9298. PubMed PMID: 31489371; PMCID: PMC6713507.

43. Kastenhuber ER, Lalazar G, Houlihan SL, Tschaharganeh DF, Baslan T, Chen CC, Requena D, Tian S, Bosbach B, Wilkinson JE, Simon SM, Lowe SW. DNAJB1-PRKACA fusion kinase interacts with beta-catenin and the liver regenerative response to drive fibrolamellar hepatocellular carcinoma. Proc Natl Acad Sci U S A. 2017;114(50):13076-84. Epub 2017/11/23. doi: 10.1073/pnas.1716483114. PubMed PMID: 29162699; PMCID: PMC5740683.

44. Engelholm LH, Riaz A, Serra D, Dagnæs-Hansen F, Johansen JV, Santoni-Rugiu E, Hansen SH, Niola F, M. Fd. CRISPR/Cas9 Engineering of Adult Mouse Liver Demonstrates That the Dnajb1-Prkaca Gene Fusion Is Sufficient to Induce Tumors Resembling Fibrolamellar Hepatocellular Carcinoma. Gastroenterology. 2017;153:1662-73.

45. Cheung J, Ginter C, Cassidy M, Franklin MC, Rudolph MJ, Robine N, Darnell RB, Hendrickson WA. Structural insights into mis-regulation of protein kinase A in human tumors. Proceedings of the National Academy of Sciences of the United States of America. 2015;112(5):1374-9. doi: 10.1073/pnas.1424206112. PubMed PMID: WOS:000349087700046.

46. Simon EP, Freije CA, Farber BA, Lalazar G, Darcy DG, Honeyman JN, Chiaroni-Clarke R, Dill BD, Molina H, Bhanot UK, La Quaglia MP, Rosenberg BR, Simon SM. Transcriptomic characterization of fibrolamellar hepatocellular carcinoma. Proc Natl Acad Sci U S A. 2015;112(44):E5916-25. Epub 2015/10/23. doi: 10.1073/pnas.1424894112. PubMed PMID: 26489647; PMCID: PMC4640752.

47. London E, Nesterova M, Sinaii N, Szarek E, Chanturiya T, Mastroyannis SA, Gavrilova O, Stratakis CA. Differentially Regulated Protein Kinase A (PKA) Activity in Adipose Tissue and Liver Is Associated With Resistance to Diet-Induced Obesity and Glucose Intolerance in Mice That Lack PKA Regulatory Subunit Type IIα. Endocrinology. 2014;155(9):3397-408.

48. Riggle KM, Riehle KJ, Kenerson HL, Turnham R, Homma MK, Kazami M, Samelson B, Bauer R, McKnight GS, Scott JD, Yeung RS. Enhanced cAMP-stimulated protein kinase A

activity in human fibrolamellar hepatocellular carcinoma. Pediatr Res. 2016;80(1):110-8. Epub 2016/03/31. doi: 10.1038/pr.2016.36. PubMed PMID: 27027723; PMCID: PMC5105330.

49. Hura GL, Menon AL, Hammel M, Rambo RP, Poole FL, 2nd, Tsutakawa SE, Jenney FE, Jr., Classen S, Frankel KA, Hopkins RC, Yang SJ, Scott JW, Dillard BD, Adams MW, Tainer JA. Robust, high-throughput solution structural analyses by small angle X-ray scattering (SAXS). Nat Methods. 2009;6(8):606-12. Epub 2009/07/22. doi: 10.1038/nmeth.1353. PubMed PMID: 19620974; PMCID: PMC3094553.

50. Herberg FW, Taylor SS. Physiological inhibitors of the catalytic subunit of cAMP-dependent protein kinase: effect of MgATP on protein-protein interactions. Biochemistry. 1993;32(50):14015-22. Epub 1993/12/21. PubMed PMID: 8268180.

51. Herberg FW, Doyle ML, Cox S, Taylor SS. Dissection of the nucleotide and metal-phosphate binding sites in cAMP-dependent protein kinase. Biochemistry. 1999;38(19):6352-60. Epub 1999/05/13. doi: 10.1021/bi982672w. PubMed PMID: 10320366.

52. Zawadzki KM, Taylor SS. cAMP-dependent protein kinase regulatory subunit type IIbeta: active site mutations define an isoform-specific network for allosteric signaling by cAMP. J Biol Chem. 2004;279(8):7029-36. Epub 2003/11/20. doi: 10.1074/jbc.M310804200. PubMed PMID: 14625280.

53. Narayana N, Cox S, Xuong NH, TenEyck LF, Taylor SS. A binary complex of the catalytic subunit of cAMP-dependent protein kinase and adenosine further defines conformational flexibility. Structure. 1997;5(7):921-35. doi: Doi 10.1016/S0969-2126(97)00246-3. PubMed PMID: WOS:A1997XN42200008.

54. Bastidas AC, Wu J, Taylor SS. Molecular features of product release for the PKA catalytic cycle. Biochemistry. 2015;54(1):2-10. Epub 2014/08/01. doi: 10.1021/bi500684c. PubMed PMID: 25077557; PMCID: PMC4295794.

55. Zheng J, Trafny EA, Knighton DR, Xuong NH, Taylor SS, Ten Eyck LF, Sowadski JM. 2.2 A refined crystal structure of the catalytic subunit of cAMP-dependent protein kinase complexed with MnATP and a peptide inhibitor. Acta Crystallogr D Biol Crystallogr. 1993;49(Pt 3):362-5. Epub 1993/05/01. doi: 10.1107/S0907444993000423. PubMed PMID: 15299527.

56. Akimoto M, McNicholl ET, Ramkissoon A, Moleschi K, Taylor SS, Melacini G. Mapping the Free Energy Landscape of PKA Inhibition and Activation: A Double-Conformational Selection Model for the Tandem cAMP-Binding Domains of PKA RIalpha. PLoS Biol. 2015;13(11):e1002305. Epub 2015/12/01. doi: 10.1371/journal.pbio.1002305. PubMed PMID: 26618408; PMCID: PMC4664472.

57. Malmstrom RD, Kornev AP, Taylor SS, Amaro RE. Allostery through the computational microscope: cAMP activation of a canonical signalling domain. Nat Commun. 2015;6:7588. Epub 2015/07/07. doi: 10.1038/ncomms8588. PubMed PMID: 26145448; PMCID: PMC4504738.

58. McNicholl ET, Das R, SilDas S, Taylor SS, Melacini G. Communication between tandem cAMP binding domains in the regulatory subunit of protein kinase A-Ialpha as revealed by domain-silencing mutations. J Biol Chem. 2010;285(20):15523-37. Epub 2010/03/06. doi: 10.1074/jbc.M110.105783. PubMed PMID: 20202931; PMCID: PMC2865341.

59. England JP, Hao Y, Bai L, Glick V, Hodges HC, Taylor SS, Maillard RA. Switching of the folding-energy landscape governs the allosteric activation of protein kinase A. Proc Natl Acad Sci U S A. 2018;115(32):E7478-E85. Epub 2018/07/25. doi: 10.1073/pnas.1802510115. PubMed PMID: 30038016; PMCID: PMC6094112.

60. Barros EP, Malmstrom RD, Nourbakhsh K, Del Rio JC, Kornev AP, Taylor SS, Amaro RE. Electrostatic Interactions as Mediators in the Allosteric Activation of Protein Kinase A RIalpha. Biochemistry. 2017;56(10):1536-45. Epub 2017/02/22. doi: 10.1021/acs.biochem.6b01152. PubMed PMID: 28221775; PMCID: PMC5495472.

61. Hirakis SP, Malmstrom RD, Amaro RE. Molecular Simulations Reveal an Unresolved Conformation of the Type IA Protein Kinase A Regulatory Subunit and Suggest Its Role in the cAMP Regulatory Mechanism. Biochemistry. 2017;56(30):3885-8. Epub 2017/07/01. doi: 10.1021/acs.biochem.7b00461. PubMed PMID: 28661131; PMCID: PMC5751417.

62. Su Y, Dostmann WR, Herberg FW, Durick K, Xuong NH, Ten Eyck L, Taylor SS, Varughese KI. Regulatory subunit of protein kinase A: structure of deletion mutant with cAMP binding domains. Science. 1995;269(5225):807-13. Epub 1995/08/11. PubMed PMID: 7638597.

63. Cao B, Lu TW, Martinez Fiesco JA, Tomasini M, Fan L, Simon SM, Taylor SS, Zhang P. Structures of the PKA RIalpha Holoenzyme with the FLHCC Driver J-PKAcalpha or Wild-Type PKAcalpha. Structure. 2019;27(5):816-28 e4. Epub 2019/03/25. doi: 10.1016/j.str.2019.03.001. PubMed PMID: 30905674; PMCID: PMC6506387.

64. Rinaldi J, Wu J, Yang J, Ralston CY, Sankaran B, Moreno S, Taylor SS. Structure of yeast regulatory subunit: a glimpse into the evolution of PKA signaling. Structure. 2010;18(11):1471-82. Epub 2010/11/13. doi: 10.1016/j.str.2010.08.013. PubMed PMID: 21070946; PMCID: PMC3435106.

65. Ringheim GE, Taylor SS. Effects of cAMP-binding site mutations on intradomain cross-communication in the regulatory subunit of cAMP-dependent protein kinase I. J Biol Chem. 1990;265(32):19472-8. Epub 1990/11/15. PubMed PMID: 2174038.

66. Bruystens JG, Wu J, Fortezzo A, Del Rio J, Nielsen C, Blumenthal DK, Rock R, Stefan E, Taylor SS. Structure of a PKA RIalpha Recurrent Acrodysostosis Mutant Explains Defective cAMP-Dependent Activation. J Mol Biol. 2016;428(24 Pt B):4890-904. Epub 2016/11/09. doi: 10.1016/j.jmb.2016.10.033. PubMed PMID: 27825928; PMCID: PMC5149412.

67. Berman HM, Ten Eyck LF, Goodsell DS, Haste NM, Kornev A, Taylor SS. The cAMP binding domain: an ancient signaling module. Proc Natl Acad Sci U S A. 2005;102(1):45-50. Epub 2004/12/25. doi: 10.1073/pnas.0408579102. PubMed PMID: 15618393; PMCID: PMC544069.

68. Ferretti AC, Tonucci FM, Hidalgo F, Almada E, Larocca MC, Favre C. AMPK and PKA interaction in the regulation of survival of liver cancer cells subjected to glucose starvation. Oncotarget. 2016;7(14):17815-28. Epub 2016/02/20. doi: 10.18632/oncotarget.7404. PubMed PMID: 26894973; PMCID: PMC4951252.

69. Knape MJ, Ballez M, Burghardt NC, Zimmermann B, Bertinetti D, Kornev AP, Herberg FW. Divalent metal ions control activity and inhibition of protein kinases. Metallomics. 2017;9(11):1576-84. Epub 2017/10/19. doi: 10.1039/c7mt00204a. PubMed PMID: 29043344.

70. Khavrutskii IV, Grant B, Taylor SS, McCammon JA. A transition path ensemble study reveals a linchpin role for Mg(2+) during rate-limiting ADP release from protein kinase A. Biochemistry. 2009;48(48):11532-45. Epub 2009/11/06. doi: 10.1021/bi901475g. PubMed PMID: 19886670; PMCID: PMC2789581.

71. Tomasini MD, Wang Y, Karamafrooz A, Li G, Beuming T, Gao J, Taylor SS, Veglia G, Simon SM. Conformational Landscape of the PRKACA-DNAJB1 Chimeric Kinase, the Driver for Fibrolamellar Hepatocellular Carcinoma. Sci Rep. 2018;8(1):720. Epub 2018/01/18. doi: 10.1038/s41598-017-18956-w. PubMed PMID: 29335433; PMCID: PMC5768683.

72. Graham RP, Lackner C, Terracciano L, Gonzalez-Cantu Y, Maleszewski JJ, Greipp PT, Simon SM, Torbenson MS. Fibrolamellar carcinoma in the Carney complex: PRKAR1A loss instead of the classic DNAJB1-PRKACA fusion. Hepatology. 2018;68(4):1441-7. Epub 2017/12/10. doi: 10.1002/hep.29719. PubMed PMID: 29222914; PMCID: PMC6151295.

73. Lu TW, Wu J, Aoto PC, Weng JH, Ahuja LG, Sun N, Cheng CY, Zhang P, S. TS. Two PKA RIα holoenzyme states define ATP as an isoform-specific orthosteric inhibitor that competes with the allosteric activator, cAMP. Proc Natl Acad Sci U S A. 2019;116(33):16347-56.

74. Petoukhov MV, Franke D, Shkumatov AV, Tria G, Kikhney AG, Gajda M, Gorba C, Mertens HD, Konarev PV, Svergun DI. New developments in the ATSAS program package for small-angle scattering data analysis. J Appl Crystallogr. 2012;45(Pt 2):342-50. Epub 2012/04/01. doi: 10.1107/S0021889812007662. PubMed PMID: 25484842; PMCID: PMC4233345.

75. Rambo RP, Tainer JA. Characterizing flexible and intrinsically unstructured biological macromolecules by SAS using the Porod-Debye law. Biopolymers. 2011;95(8):559-71. Epub 2011/04/22. doi: 10.1002/bip.21638. PubMed PMID: 21509745; PMCID: PMC3103662.

76. Yang J, Zhang Y. I-TASSER server: new development for protein structure and function predictions. Nucleic Acids Res. 2015;43(W1):W174-81. Epub 2015/04/18. doi: 10.1093/nar/gkv342. PubMed PMID: 25883148; PMCID: PMC4489253.

77. Walker-Gray R, Stengel F, Gold MG. Mechanisms for restraining cAMP-dependent protein kinase revealed by subunit quantitation and cross-linking approaches. Proc Natl Acad Sci U S A. 2017;114(39):10414-9. Epub 2017/09/13. doi: 10.1073/pnas.1701782114. PubMed PMID: 28893983; PMCID: PMC5625894.

78. Byun JA, Akimoto M, VanSchouwen B, Lazarou TS, Taylor SS, Melacini G. Allosteric Pluripotency as 1 Revealed by Protein Kinase A. Under Review.

79. Hao Y, England JP, Bellucci L, Paci E, Hodges HC, Taylor SS, Maillard RA. Activation of PKA via asymmetric allosteric coupling of structurally conserved cyclic nucleotide binding domains. Nat Commun. 2019;10(1):3984. Epub 2019/09/06. doi: 10.1038/s41467-019-11930-2. PubMed PMID: 31484930; PMCID: PMC6726620.

80. Diller TC, Madhusudan, Xuong NH, Taylor SS. Molecular basis for regulatory subunit diversity in cAMP-dependent protein kinase: crystal structure of the type II beta regulatory subunit. Structure. 2001;9(1):73-82. Epub 2001/05/09. doi: 10.1016/s0969-2126(00)00556-6. PubMed PMID: 11342137.

81. Gold MG, Lygren B, Dokurno P, Hoshi N, McConnachie G, Tasken K, Carlson CR, Scott JD, Barford D. Molecular basis of AKAP specificity for PKA regulatory subunits. Mol Cell. 2006;24(3):383-95. Epub 2006/11/04. doi: 10.1016/j.molcel.2006.09.006. PubMed PMID: 17081989.

82. Fraser ID, Scott JD. Modulation of ion channels: a "current" view of AKAPs. Neuron. 1999;23(3):423-6. Epub 1999/08/05. doi: 10.1016/s0896-6273(00)80795-3. PubMed PMID: 10433254.

83. Banky P, Huang LJ, Taylor SS. Dimerization/docking domain of the type Ialpha regulatory subunit of cAMP-dependent protein kinase. Requirements for dimerization and docking are distinct but overlapping. J Biol Chem. 1998;273(52):35048-55. Epub 1998/12/18. doi: 10.1074/jbc.273.52.35048. PubMed PMID: 9857038.

84. Wang Y, Ho TG, Bertinetti D, Neddermann M, Franz E, Mo GC, Schendowich LP, Sukhu A, Spelts RC, Zhang J, Herberg FW, Kennedy EJ. Isoform-selective disruption of AKAP-localized PKA using hydrocarbon stapled peptides. ACS Chem Biol. 2014;9(3):635-42. Epub 2014/01/16. doi: 10.1021/cb400900r. PubMed PMID: 24422448; PMCID: PMC3985448.

85. Tillo SE, Xiong WH, Takahashi M, Miao S, Andrade AL, Fortin DA, Yang G, Qin M, Smoody BF, Stork PJS, Zhong H. Liberated PKA Catalytic Subunits Associate with the Membrane via Myristoylation to Preferentially Phosphorylate Membrane Substrates. Cell Rep. 2017;19(3):617-29. Epub 2017/04/20. doi: 10.1016/j.celrep.2017.03.070. PubMed PMID: 28423323; PMCID: PMC5481286.

86. Patel HH, Hamuro LL, Chun BJ, Kawaraguchi Y, Quick A, Rebolledo B, Pennypacker J, Thurston J, Rodriguez-Pinto N, Self C, Olson G, Insel PA, Giles WR, Taylor SS, Roth DM. Disruption of protein kinase A localization using a trans-activator of transcription (TAT)-conjugated A-kinase-anchoring peptide reduces cardiac function. J Biol Chem. 2010;285(36):27632-40. Epub 2010/06/29. doi: 10.1074/jbc.M110.146589. PubMed PMID: 20581396; PMCID: PMC2934631.

87. Smith FD, Reichow SL, Esseltine JL, Shi D, Langeberg LK, Scott JD, Gonen T. Intrinsic disorder within an AKAP-protein kinase A complex guides local substrate phosphorylation. Elife. 2013;2. doi: ARTN e0131910.7554/eLife.01319. PubMed PMID: WOS:000328640600006.

88. Vigil D, Blumenthal DK, Taylor SS, Trewhella J. Solution scattering reveals large differences in the global structures of type II protein kinase A isoforms. J Mol Biol. 2006;357(3):880-9. Epub 2006/02/08. doi: 10.1016/j.jmb.2006.01.006. PubMed PMID: 16460759.

89. Zhang P, Ye F, Bastidas AC, Kornev AP, Wu J, Ginsberg MH, Taylor SS. An Isoform-Specific Myristylation Switch Targets Type II PKA Holoenzymes to Membranes. Structure. 2015;23(9):1563-72. Epub 2015/08/19. doi: 10.1016/j.str.2015.07.007. PubMed PMID: 26278174; PMCID: PMC4558360.

90. Sigal CT, Zhou W, Buser CA, McLaughlin S, Resh MD. Amino-terminal basic residues of Src mediate membrane binding through electrostatic interaction with acidic phospholipids. Proc Natl Acad Sci U S A. 1994;91(25):12253-7. Epub 1994/12/06. doi: 10.1073/pnas.91.25.12253. PubMed PMID: 7527558; PMCID: PMC45415.

91. Herberg FW, Zimmermann B, Mcglone M, Taylor SS. Importance of the A-helix of the catalytic subunit of cAMP-dependent protein kinase for stability and for orienting subdomains at the cleft interface. Protein Science. 1997;6(3):569-79.

92. McClendon CL, Kornev AP, Gilson MK, Taylor SS. Dynamic architecture of a protein kinase. Proc Natl Acad Sci U S A. 2014;111(43):E4623-31. Epub 2014/10/17. doi: 10.1073/pnas.1418402111. PubMed PMID: 25319261; PMCID: PMC4217441.

93. Gaffarogullari EC, Masterson LR, Metcalfe EE, Traaseth NJ, Balatri E, Musa MM, Mullen D, Distefano MD, Veglia G. A myristoyl/phosphoserine switch controls cAMP-dependent protein kinase association to membranes. J Mol Biol. 2011;411(4):823-36. Epub 2011/07/12. doi: 10.1016/j.jmb.2011.06.034. PubMed PMID: 21740913; PMCID: PMC3487414.

94. Jedrzejewski PT, Girod A, Tholey A, Konig N, Thullner S, Kinzel V, Bossemeyer D. A conserved deamidation site at Asn 2 in the catalytic subunit of mammalian cAMP-dependent protein kinase detected by capillary LC-MS and tandem mass spectrometry. Protein Sci. 1998;7(2):457-69. Epub 1998/04/01. doi: 10.1002/pro.5560070227. PubMed PMID: 9521123; PMCID: PMC2143929.

95. Pepperkok R, Hotz-Wagenblatt A, Konig N, Girod A, Bossemeyer D, Kinzel V. Intracellular distribution of mammalian protein kinase A catalytic subunit altered by conserved Asn2 deamidation. J Cell Biol. 2000;148(4):715-26. Epub 2000/02/23. doi: 10.1083/jcb.148.4.715. PubMed PMID: 10684253; PMCID: PMC2169370.

96. Zhang JZ, Lu T-W, Stolerman LM, Tenner B, Yang J, Zhang J-F, Rangamani P, Taylor SS, Mehta S, Zhang J. PKA RIα phase separation drives cAMP compartmentation and suppresses tumorigenic signaling Under Review.

97. Olivieri C, Walker C, Karamafrooz A, Yingjie W, V. S. M, Porcelli F, Blumenthal DK, Thomas DD, Bernlohr DA, Sandford SM, Taylor SS, Veglia G. J-domain fusion of chimeric kinase A disrupts binding cooperativity and imparts defective regulation by endogenous kinase inhibitor. Under Review.

98. Jinek M, Chylinski K, Fonfara I, Hauer M, Doudna JA, Charpentier E. A programmable dual-RNA-guided DNA endonuclease in adaptive bacterial immunity. Science. 2012;337(6096):816-21. Epub 2012/06/30. doi: 10.1126/science.1225829. PubMed PMID: 22745249; PMCID: PMC6286148.

99. Esvelt KM, Smidler AL, Catteruccia F, Church GM. Concerning RNA-guided gene drives for the alteration of wild populations. Elife. 2014;3. Epub 2014/07/19. doi: 10.7554/eLife.03401. PubMed PMID: 25035423; PMCID: PMC4117217.

100. Hsu PD, Scott DA, Weinstein JA, Ran FA, Konermann S, Agarwala V, Li Y, Fine EJ, Wu X, Shalem O, Cradick TJ, Marraffini LA, Bao G, Zhang F. DNA targeting specificity of RNA-guided Cas9 nucleases. Nat Biotechnol. 2013;31(9):827-32. Epub 2013/07/23. doi: 10.1038/nbt.2647. PubMed PMID: 23873081; PMCID: PMC3969858.

101. Cong L, Ran FA, Cox D, Lin S, Barretto R, Habib N, Hsu PD, Wu X, Jiang W, Marraffini LA, Zhang F. Multiplex genome engineering using CRISPR/Cas systems. Science. 2013;339(6121):819-23. Epub 2013/01/05. doi: 10.1126/science.1231143. PubMed PMID: 23287718; PMCID: PMC3795411.

102. Galluzzi L, Kepp O, Kroemer G. Mitochondrial dynamics: a strategy for avoiding autophagy. Curr Biol. 2011;21(12):R478-80. Epub 2011/06/21. doi: 10.1016/j.cub.2011.05.002. PubMed PMID: 21683905.

103. Willems PH, Rossignol R, Dieteren CE, Murphy MP, Koopman WJ. Redox Homeostasis and Mitochondrial Dynamics. Cell Metab. 2015;22(2):207-18. Epub 2015/07/15. doi: 10.1016/j.cmet.2015.06.006. PubMed PMID: 26166745.

104. Srinivasan S, Spear J, Chandran K, Joseph J, Kalyanaraman B, Avadhani NG. Oxidative stress induced mitochondrial protein kinase A mediates cytochrome c oxidase dysfunction. PLoS One. 2013;8(10):e77129. Epub 2013/10/17. doi: 10.1371/journal.pone.0077129. PubMed PMID: 24130844; PMCID: PMC3795003.

105. Bejarano E, Cabrera M, Vega L, Hidalgo J, Velasco A. Golgi structural stability and biogenesis depend on associated PKA activity. J Cell Sci. 2006;119(Pt 18):3764-75. Epub 2006/08/24. doi: 10.1242/jcs.03146. PubMed PMID: 16926194.

106. Lutz W, Lingle WL, McCormick D, Greenwood TM, Salisbury JL. Phosphorylation of centrin during the cell cycle and its role in centriole separation preceding centrosome duplication. J Biol Chem. 2001;276(23):20774-80. Epub 2001/03/30. doi: 10.1074/jbc.M101324200. PubMed PMID: 11279195.

107. Depry C, Allen MD, Zhang J. Visualization of PKA activity in plasma membrane microdomains. Mol Biosyst. 2011;7(1):52-8. Epub 2010/09/15. doi: 10.1039/c0mb00079e. PubMed PMID: 20838685.

108. Zhang J, Ma Y, Taylor SS, Tsien RY. Genetically encoded reporters of protein kinase A activity reveal impact of substrate tethering. Proc Natl Acad Sci U S A. 2001;98(26):14997-5002. Epub 2001/12/26. doi: 10.1073/pnas.211566798. PubMed PMID: 11752448; PMCID: PMC64972.

109. DeBerardinis RJ, Chandel NS. We need to talk about the Warburg effect. Nature Metabolism. 2020;2(2):127-9. doi: 10.1038/s42255-020-0172-2.

110. Liberti MV, Locasale JW. The Warburg Effect: How Does it Benefit Cancer Cells? Trends Biochem Sci. 2016;41(3):211-8. Epub 2016/01/19. doi: 10.1016/j.tibs.2015.12.001. PubMed PMID: 26778478; PMCID: PMC4783224.

111. Dashty M. A quick look at biochemistry: carbohydrate metabolism. Clin Biochem. 2013;46(15):1339-52. Epub 2013/05/18. doi: 10.1016/j.clinbiochem.2013.04.027. PubMed PMID: 23680095.

112. Aguer C, Gambarotta D, Mailloux RJ, Moffat C, Dent R, McPherson R, Harper ME. Galactose enhances oxidative metabolism and reveals mitochondrial dysfunction in human primary muscle cells. PLoS One. 2011;6(12):e28536. Epub 2011/12/24. doi: 10.1371/journal.pone.0028536. PubMed PMID: 22194845; PMCID: PMC3240634.

113. Boettcher AJ, Wu J, Kim C, Yang J, Bruystens J, Cheung N, Pennypacker JK, Blumenthal DA, Kornev AP, Taylor SS. Realizing the allosteric potential of the tetrameric protein kinase A RIalpha holoenzyme. Structure. 2011;19(2):265-76. Epub 2011/02/09. doi: 10.1016/j.str.2010.12.005. PubMed PMID: 21300294; PMCID: PMC3097484.

114. Vangone A, Bonvin AM. Contacts-based prediction of binding affinity in protein-protein complexes. Elife. 2015;4:e07454. Epub 2015/07/21. doi: 10.7554/eLife.07454. PubMed PMID: 26193119; PMCID: PMC4523921.

115. Isensee J, Kaufholz M, Knape MJ, Hasenauer J, Hammerich H, Gonczarowska-Jorge H, Zahedi RP, Schwede F, Herberg FW, Hucho T. PKA-RII subunit phosphorylation precedes activation by cAMP and regulates activity termination. J Cell Biol. 2018;217(6):2167-84. Epub 2018/04/05. doi: 10.1083/jcb.201708053. PubMed PMID: 29615473; PMCID: PMC5987717.

116. Rangel-Aldao R, Rosen OM. Dissociation and reassociation of the phosphorylated and nonphosphorylated forms of adenosine 3':5' -monophosphate-dependent protein kinase from bovine cardiac muscle. J Biol Chem. 1976;251(11):3375-80. Epub 1976/06/10. PubMed PMID: 179996.

117. Oliveria SF, Dell'Acqua ML, Sather WA. AKAP79/150 anchoring of calcineurin controls neuronal L-type Ca2+ channel activity and nuclear signaling. Neuron. 2007;55(2):261-75. Epub 2007/07/21. doi: 10.1016/j.neuron.2007.06.032. PubMed PMID: 17640527; PMCID: PMC2698451.

118. Langeberg LK, Scott JD. Signalling scaffolds and local organization of cellular behaviour. Nat Rev Mol Cell Biol. 2015;16(4):232-44. Epub 2015/03/19. doi: 10.1038/nrm3966. PubMed PMID: 25785716; PMCID: PMC4722875.

119. Brown SH, Cheng CY, Saldanha SA, Wu J, Cottam HB, Sankaran B, Taylor SS. Implementing fluorescence anisotropy screening and crystallographic analysis to define PKA isoform-selective activation by cAMP analogs. ACS Chem Biol. 2013;8(10):2164-72. Epub 2013/08/28. doi: 10.1021/cb400247t. PubMed PMID: 23978166; PMCID: PMC3827627.

120. Emsley P, Cowtan K. Coot: model-building tools for molecular graphics. Acta Crystallogr D Biol Crystallogr. 2004;60(Pt 12 Pt 1):2126-32. Epub 2004/12/02. doi: 10.1107/S0907444904019158. PubMed PMID: 15572765.

121. Laskowski RA, MacArthur MW, Moss DS, Thornton JM. PROCHECK: a program to check the stereochemical quality of protein structures. Journal of Applied Crystallography. 1993;26(2):283-91. doi: 10.1107/s0021889892009944.

122. Suloway C, Pulokas J, Fellmann D, Cheng A, Guerra F, Quispe J, Stagg S, Potter CS, Carragher B. Automated molecular microscopy: the new Leginon system. J Struct Biol. 2005;151(1):41-60. Epub 2005/05/14. doi: 10.1016/j.jsb.2005.03.010. PubMed PMID: 15890530.

123. Tan YZ, Baldwin PR, Davis JH, Williamson JR, Potter CS, Carragher B, Lyumkis D. Addressing preferred specimen orientation in single-particle cryo-EM through tilting. Nat Methods. 2017;14(8):793-6. Epub 2017/07/04. doi: 10.1038/nmeth.4347. PubMed PMID: 28671674; PMCID: PMC5533649.

124. Su M, Guo EZ, Ding X, Li Y, Tarrasch JT, Brooks CL, 3rd, Xu Z, Skiniotis G. Mechanism of Vps4 hexamer function revealed by cryo-EM. Sci Adv. 2017;3(4):e1700325. Epub 2017/04/26. doi: 10.1126/sciadv.1700325. PubMed PMID: 28439563; PMCID: PMC5392032.

125. Lander GC, Stagg SM, Voss NR, Cheng A, Fellmann D, Pulokas J, Yoshioka C, Irving C, Mulder A, Lau PW, Lyumkis D, Potter CS, Carragher B. Appion: an integrated, database-driven pipeline to facilitate EM image processing. J Struct Biol. 2009;166(1):95-102. Epub 2009/03/06. doi: 10.1016/j.jsb.2009.01.002. PubMed PMID: 19263523; PMCID: PMC2775544.

126. Zheng SQ, Palovcak E, Armache JP, Verba KA, Cheng Y, Agard DA. MotionCor2: anisotropic correction of beam-induced motion for improved cryo-electron microscopy. Nat Methods. 2017;14(4):331-2. Epub 2017/03/03. doi: 10.1038/nmeth.4193. PubMed PMID: 28250466; PMCID: PMC5494038.

127. Rohou A, Grigorieff N. CTFFIND4: Fast and accurate defocus estimation from electron micrographs. J Struct Biol. 2015;192(2):216-21. Epub 2015/08/19. doi: 10.1016/j.jsb.2015.08.008. PubMed PMID: 26278980; PMCID: PMC6760662.

128. Roseman AM. FindEM--a fast, efficient program for automatic selection of particles from electron micrographs. J Struct Biol. 2004;145(1-2):91-9. Epub 2004/04/07. doi: 10.1016/j.jsb.2003.11.007. PubMed PMID: 15065677.

129. Scheres SH. RELION: implementation of a Bayesian approach to cryo-EM structure determination. J Struct Biol. 2012;180(3):519-30. Epub 2012/09/25. doi: 10.1016/j.jsb.2012.09.006. PubMed PMID: 23000701; PMCID: PMC3690530.

130. Zhang K. Gctf: Real-time CTF determination and correction. J Struct Biol. 2016;193(1):1-12. Epub 2015/11/26. doi: 10.1016/j.jsb.2015.11.003. PubMed PMID: 26592709; PMCID: PMC4711343.

131. Punjani A, Rubinstein JL, Fleet DJ, Brubaker MA. cryoSPARC: algorithms for rapid unsupervised cryo-EM structure determination. Nat Methods. 2017;14(3):290-6. Epub 2017/02/07. doi: 10.1038/nmeth.4169. PubMed PMID: 28165473.

132. Wang RY, Song Y, Barad BA, Cheng Y, Fraser JS, DiMaio F. Automated structure refinement of macromolecular assemblies from cryo-EM maps using Rosetta. Elife. 2016;5. Epub 2016/09/27. doi: 10.7554/eLife.17219. PubMed PMID: 27669148; PMCID: PMC5115868.

133. Horn HW, Swope WC, Pitera JW, Madura JD, Dick TJ, Hura GL, Head-Gordon T. Development of an improved four-site water model for biomolecular simulations: TIP4P-Ew. J Chem Phys. 2004;120(20):9665-78. Epub 2004/07/23. doi: 10.1063/1.1683075. PubMed PMID: 15267980.

134. Salomon-Ferrer R, Case DA, Walker RC. An overview of the Amber biomolecular simulation package. Wiley Interdisciplinary Reviews: Computational Molecular Science. 2013;3(2):198-210. doi: 10.1002/wcms.1121.

135. Homeyer N, Horn AH, Lanig H, Sticht H. AMBER force-field parameters for phosphorylated amino acids in different protonation states: phosphoserine, phosphothreonine, phosphotyrosine, and phosphohistidine. J Mol Model. 2006;12(3):281-9. Epub 2005/10/22. doi: 10.1007/s00894-005-0028-4. PubMed PMID: 16240095.

136. Hopkins CW, Le Grand S, Walker RC, Roitberg AE. Long-Time-Step Molecular Dynamics through Hydrogen Mass Repartitioning. J Chem Theory Comput. 2015;11(4):1864-74. Epub 2015/11/18. doi: 10.1021/ct5010406. PubMed PMID: 26574392.

137. Le Grand S, Götz AW, Walker RC. SPFP: Speed without compromise—A mixed precision model for GPU accelerated molecular dynamics simulations. Computer Physics Communications. 2013;184(2):374-80. doi: 10.1016/j.cpc.2012.09.022.

138. Salomon-Ferrer R, Gotz AW, Poole D, Le Grand S, Walker RC. Routine Microsecond Molecular Dynamics Simulations with AMBER on GPUs. 2. Explicit Solvent Particle Mesh Ewald. J Chem Theory Comput. 2013;9(9):3878-88. Epub 2013/09/10. doi: 10.1021/ct400314y. PubMed PMID: 26592383.

139. Miao Y, Feher VA, McCammon JA. Gaussian Accelerated Molecular Dynamics: Unconstrained Enhanced Sampling and Free Energy Calculation. J Chem Theory Comput. 2015;11(8):3584-95. Epub 2015/08/25. doi: 10.1021/acs.jctc.5b00436. PubMed PMID: 26300708; PMCID: PMC4535365.

140. Kikhney AG, Svergun DI. A practical guide to small angle X-ray scattering (SAXS) of flexible and intrinsically disordered proteins. FEBS Lett. 2015;589(19 Pt A):2570-7. Epub 2015/09/01. doi: 10.1016/j.febslet.2015.08.027. PubMed PMID: 26320411.

141. Franke D, Petoukhov MV, Konarev PV, Panjkovich A, Tuukkanen A, Mertens HDT, Kikhney AG, Hajizadeh NR, Franklin JM, Jeffries CM, Svergun DI. ATSAS 2.8: a comprehensive data analysis suite for small-angle scattering from macromolecular solutions. J Appl Crystallogr. 2017;50(Pt 4):1212-25. Epub 2017/08/16. doi: 10.1107/S1600576717007786. PubMed PMID: 28808438; PMCID: PMC5541357.

142. Saldanha SA, Kaler G, Cottam HB, Abagyan R, Taylor SS. Assay principle for modulators of protein-protein interactions and its application to non-ATP-competitive ligands targeting protein kinase A. Anal Chem. 2006;78(24):8265-72. Epub 2006/12/15. doi: 10.1021/ac061104g. PubMed PMID: 17165815; PMCID: PMC3435108.

143. Lacroix E, Viguera AR, Serrano L. Elucidating the folding problem of alpha-helices: local motifs, long-range electrostatics, ionic-strength dependence and prediction of NMR parameters. J Mol Biol. 1998;284(1):173-91. Epub 1998/11/13. doi: 10.1006/jmbi.1998.2145. PubMed PMID: 9811549.